# UNIVERSITY OF PADUA


Department of Industrial Engineering
Master's Degree in Aerospace Engineering

## A NUMERICAL STUDY ON THE UNSTEADY AERODYNAMIC BEHAVIOUR IN CLOSE GROUND PROXIMITY OF A FORMULA 1 STYLE UNDERBODY

Luca Pellizzari
Matr. n. 1242418

Advisor: Prof. Francesco PICANO
Co-advisor: Prof. Matteo MASSARO

— ACADEMIC YEAR 2022/2023 —

**Abstract**

The study investigates the downforce generation capabilities of a Formula One 2022-style underbody placed close to a moving ground and subjected to a pure heave oscillatory motion. The investigation has been conducted using both IDDES and URANS solvers coupled with the SST Menter K-omega turbulence model. To achieve a close ground proximity oscillation a sliding grid approach coupled with an AMR (Adaptive Mesh Refinement) solver has been used. For values of the reduced frequency k between 0.754 and 1.508 the oscillation induced a significant amplification in the aerodynamic forces compared to the quasi-static assumption. In order to understand the origin of this amplification and to build a predictive model, multiple geometries of increasing complexity were tested. A fundamental finding is the almost linear relationship between the downforce circulatory component oscillation amplitude and the effective ground load GE. A new added mass component was derived and shown to be non negligible at high frequencies for geometries with low ride height endplates. Due to this component presence, endplate longitudinal extension has shown to be the most influential feature on forces oscillation amplitude at high frequencies. The addition of other near ground features like footplates or a central hull has shown mostly no effect beside differences in GE magnitude.

# Contents

# Chapter 1

# Introduction

## 1.1 Introduction to the topic

Before the first wing was introduced in motor sport racing in 1966, aerodynamic developments of racing cars had been limited to streamlining the overall profile of the car while maintaining adequate engine cooling [1]. The introduction of wings in 1966 heralded a new era in racing car aerodynamics. Through the use of negative lift (downforce), the grip between the tires and the road surface had been significantly increased, thus achieving higher cornering speeds and lateral accelerations. One category of motorsport where aerodynamic development has had a significant impact is Formula One. Since the first technical regulations limitations on wing size and placement were introduced in Formula One, the drive for optimum wing performance have progressively escalated over time. The true potential of ground effect aerodynamics was realised in 1977 with the introduction of the Lotus type 78 [1]. Through the use of flexible side skirts, wings close to the ground and a shaped underbody the Lotus type 78 represented a milestone in ground effect aerodynamics in Formula One.

The exploitation of ground effect allowed downforce levels to reach unprecedented heights, resulting in higher cornering speeds than ever before. Although under optimal conditions, the combination of side skirts and a profiled underbody provided significant vertical load, which was constantly on the verge of disappearing. Ride height and body trim sensitivity were inherent characteristics of these cars, but tracks were rarely smooth, often filled with bumps and curbs. Drivers in a race frequently took risks, engaged in battles, and made mistakes, making encounters with track irregularities unavoidable. These encounters often caused sideskirt damage or malfunctions , leading to a sudden loss of downforce and, in many

cases, catastrophic accidents. Due to the rising number of accidents in the 1980s, the FIA (Federation Internationale de l'Automobile) prohibited sliding side skirts and mandated the adoption of a flat underbody. From that point onwards, racing car aerodynamics in Formula One have focused on the front wing, rear wing, and rear diffuser. This trend has persisted since the 2022 technical regulation changes, where the flat underbody was replaced by significantly more complex venturi channels.

The 2022 technical regulations opened the door to multiple fundamentally different development paths, and choosing any path with these limitations is akin to take a leap of faith. The combination of the significant shift in the primary method of generating downforce, the absence of testing, the simplification of mechanical components previously dedicated to the aerodynamic platform control and, finally, the limited understanding of unsteady aerodynamic phenomena in ground proximity, has led to the emergence of the phenomenon known as "porpoising" in 2022. "Porpoising" is a term used in aerodynamics and racing car mechanics to describe an unwanted dynamic phenomenon. This movement resembles the up-and-down motion of a dolphin (hence the term "porpoising," derived from the English word "porpoise," referring to the marine mammal) as it swims in water.

## 1.2 Applicability of research

The primary application of this research is within the realm of motorsport, specifically in categories that rely on ground effect as the primary method to generate downforce. There exists a lack of quantitative data concerning oscillating low aspect ratio wings in close ground proximity.

Most of the studies on oscillating wings have focused on insect flight and micro air vehicles (MAVs). Insects fly at low Reynolds numbers, so the flow physics differ from racing car wings. Furthermore, both applications are generally focused on thrust generation and wake structure. The work published on unsteady ground effect has been exclusively conducted through 2D numerical simulations and so far it has only offered a qualitative analysis of the various effects at play.

None of these studies have provided predictive capabilities that could have assisted teams in avoiding porpoising during the 2022 Formula One season. Therefore, even if someone had been able to anticipate the susceptibility of the new cars to the phenomenon, without expensive fully coupled unsteady simulations, there would have been no way to quantify its magnitude

to develop countermeasures nor to evaluate its impact on overall performance.

## 1.3 Aims of the present thesis

The aims of this research were the following.

- To investigate and quantify the flow field generated by a Formula One 2022 style underbody.
- To investigate the effects of oscillatory heaving motion on the performance of a Formula One 2022 style underbody.
- To explore how geometric features influence the heave frequency response of a Formula One 2022 style underbody.
- To deepen the understanding of the unsteady force generation mechanisms of an inverted low aspect ratio wing in close proximity to the ground.
- To propose a predictive model for these unsteady aerodynamic force generation mechanisms

This thesis is divided into four main sections. Firstly the simulation setups used during this research will be discussed within chapters 2 to 4 with validation considerations in chapter 5. Then numerical results of this research will be covered from chapter 6 to chapter 7. In chapter 8 an empirical model with predictive capabilities regarding the unsteady forces generated in ground effect will be presented. Finally in chapter 9 the results will be summarised and some recommendations for future investigations will be offered.

# Chapter 2

# CFD Model

In this chapter, an explanation of the CFD approach will be provided along with a brief overview of the formulations used. Specifically, both incompressible URANS (Unsteady Reynolds-Averaged Navier-Stokes) and IDDES (Improved Delayed Detached Eddy Simulation) have been implemented using a second-order implicit temporal scheme. The simulation process involves finite volume discretization using unstructured grids. Relative heaving motion has been implemented through the use of two overlapping grids, a method known as the Overset-mesh method. Additionally, considerations regarding the use of Adaptive Mesh Refinement (AMR) strategies will also be discussed.

## 2.1 Computational strategy

To gain a deeper understanding of the observed porpoising phenomenon during the 2022 Formula One season, computational investigations were conducted. These investigations were carried out with two main objectives:

1. To enhance the qualitative knowledge of the unsteady aerodynamic flow field.

2. To collect data across a wide range of geometries and oscillation conditions.

The initial cases involved a complex geometry inspired by actual Formula One 2022 underbody configurations. The most prominent features of the underbodies were replicated from Formula Ones that experienced the phenomenon most prominently, such as the Ferrari SF-75 and the Mercedes-Benz Petronas W-13. Due to limitations in computational resources, the geometry in these cases will not include wings, tires, suspension arms, and features above

the underbody, such as sidepods, bonnets, and cooling vents. It has been assumed that the porpoising phenomenon is primarily related to the interaction between the lower surface of the underbody and the ground. A hybrid RANS-LES known as IDDES (Improved Delayed Detached Eddy Simulation) formulation had been employed to capture grid-resolvable eddies both for steady state and heaving cases. This choice was made to investigate any hypotheses concerning the connection between unsteady turbulent flow and the porpoising phenomenon.

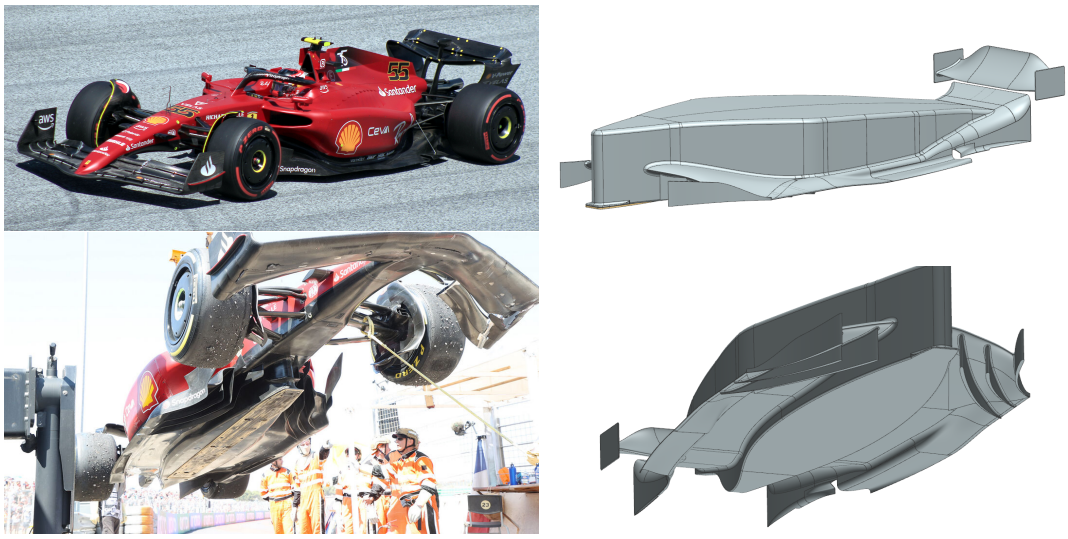

**Figure 2.1:** *Comparison between a the F1-75 2022 Formula One car and the "complex" case considered in this thesis*

Both quasi-steady and periodic imposed heaving motion will be investigated to study the aerodynamic forces through a series of simulation cases. The real porpoising phenomenon involves a combined motion of heaving and pitching. However, it's challenging to accurately quantify the magnitude and phase of the pitching motion due to a lack of data. Therefore, another hypothesis made during this work is that pitching effects are negligible. Porpoising motion has thus been modeled as a pure one-degree-of-freedom (1DOF) heaving motion. In the 2022 Formula One season, both oscillation frequency and amplitude varied significantly across teams, tracks, and setups. Frequency data have been publicly released by the FIA, showing a range varying from 4.5Hz to 6Hz. In this thesis a range between 3 and 6Hz has been considered. The heaving amplitude has been assumed to be a maximum of 30mm based on quick image measurements.

The porpoising phenomenon has been observed to occur at speeds as low as 40 m/s, impacting the behavior of the car not only at its top speed during straight-line braking but also in medium-high-speed corners, where a consistent aerodynamic load is essential for performance.

At high speeds and during an oscillating heaving motion, a combination of aerodynamic and inertial forces often leads to a condition known as "bottoming". Bottoming occurs when the wooden plank, positioned on the bottom of the central hull of the car, comes into contact with and scrapes the ground. This wooden plank is placed 10 mm below the *reference plane* as specified by the Formula One 2022 regulations.

According to these regulations, every surface of the car's underbody must remain above this plane. This means that when bottoming occurs, disregarding any possible deformations, the only part of the car touching the ground is the wooden plank, and everything else remains 10 mm above the ground. Replicating the condition where a large surface like the plank touches the ground while maintaining a real-time accurate monitoring of body forces on the geometry is not feasible. Therefore, in this thesis, the presence of the plank will be disregarded. This means that no part of the geometry will ever touch the ground, while still maintaining a minimum height of 10 mm, thus accurately simulating the real minimum height condition.

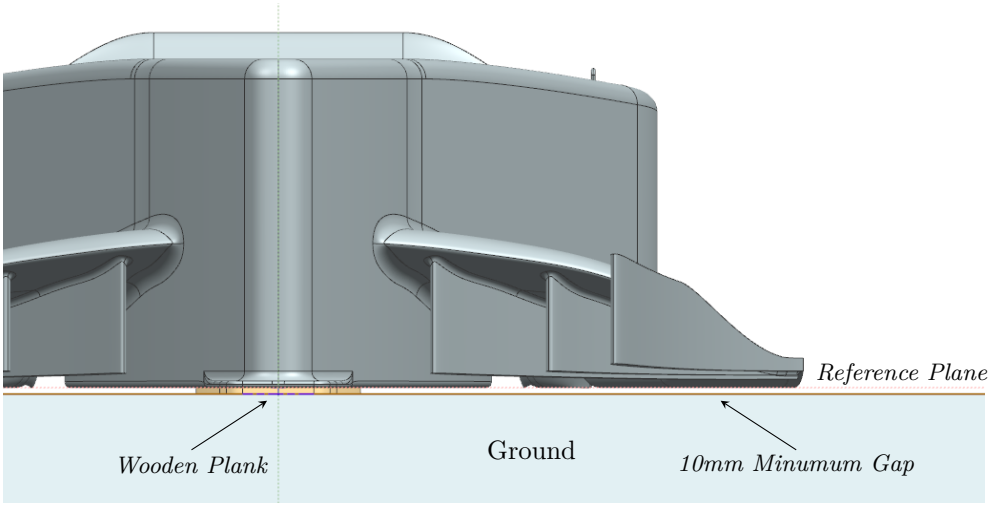


**Figure 2.2:** *CAD model at the minimum height condition considered*

Many hypotheses have been proposed by influential figures in the motorsport world to explain the cause of porpoising. However, since there is no publicly available material regarding any work done to attempt validation of these hypotheses, to fulfill the first objective, it was essential to limit the number of initial assumptions regarding the true causes of this phenomenon.

Following the results from the initial complex cases, a dependence of the phenomenon on turbulent oscillations was ruled out, as the amplitude of turbulent-induced force oscillations is several orders of magnitude lower compared to the amplitude of the forces induced by

heaving motion. Therefore, the second set of cases has been limited to a URANS (Unsteady Reynolds-Averaged Navier-Stokes) formulation for the heaving geometry simulations and RANS formulation for the stationary ones. In this second set of cases, the objective is to collect information on the relationship between geometric features and unsteady forces. The full geometry has been idealised as an inverted wing with various combinations and dimensions of Formula One 2022 underbody features, such as endplates, footplates, and a hull.

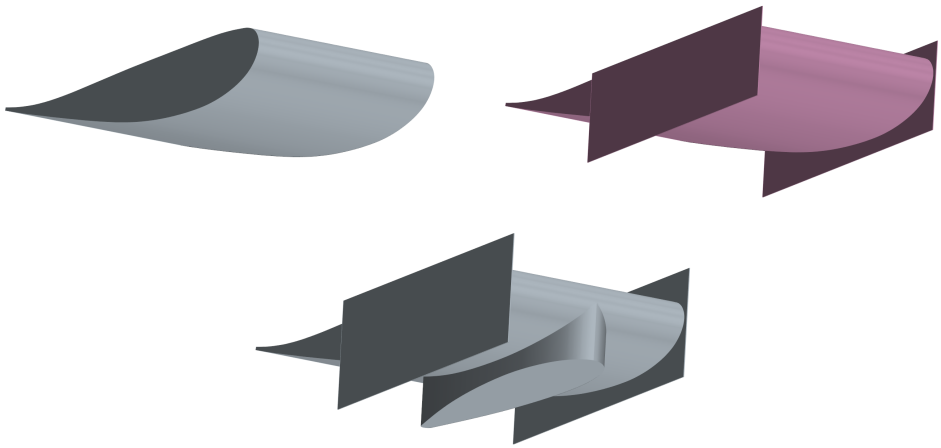

**Figure 2.3:** *Showcase of some of the simple geometries and some of the Formula One-like geometrical features tested*

## 2.2 Governing equations

Starting with the incompressible Navier-Stokes equations in three dimensions, Reynolds averaging is applied by decomposing each variable into a mean component ($U$, $P$) and a fluctuating component ($u'$, $p'$), where $U$ represents the mean velocity, $P$ is the mean pressure, $u'$ represents the velocity fluctuation, and $p'$ is the pressure fluctuation. This decomposition is expressed as $u_i = U_i + u_i'$ for velocity field and similarly $p = P + p'$ for the pressure field. The Reynolds averaging operation will be indicated as:

$$\langle u_i \rangle = U_i \tag{2.1}$$

$$\langle p \rangle = P \tag{2.2}$$

Substituting these relations into the incompressible Navier-Stokes equations and applying Reynolds averaging results in the Incompressible URANS (Unsteady Reynolds-Averaged Navier-

Stokes) equations:

$$\frac{\partial U_i}{\partial x_i} = 0, \;\; \frac{\partial u_i'}{\partial x_i} = 0 \tag{2.3}$$

$$\rho\left(\frac{\partial U_i}{\partial t} + U_j\frac{\partial U_i}{\partial x_j}\right) = \frac{\partial}{\partial x_j}\left(\mu\left(\frac{\partial U_i}{\partial x_j} + \frac{\partial U_j}{\partial x_i}\right) - P\delta_{ij} - \rho\langle u_i'u_j'\rangle\right) \tag{2.4}$$

$$R_{ij} = -\rho\langle u_i'u_j'\rangle = -\rho\begin{pmatrix} \langle u'u'\rangle & \langle u'v'\rangle & \langle u'w'\rangle \\ \langle u'v'\rangle & \langle v'v'\rangle & \langle v'w'\rangle \\ \langle u'w'\rangle & \langle v'w'\rangle & \langle w'w'\rangle \end{pmatrix} \tag{2.5}$$

Where eq. (2.3) represent the continuity equations, where both the mean velocity and fluctuating velocity fields are divergence-free (solenoidal). eq. (2.4) is the momentum equation and depends solely on terms from the mean velocity field, except for the term $R_{ij}$. The Reynolds stress tensor $R_{ij}$, which is a 3x3 matrix, consists of 6 independent components associated with the velocity fluctuation field. Identifying these components is referred to as the RANS closure problem. Resolving this problem is where turbulence modeling plays a critical role. Turbulence models provide relationships for the components of the Reynolds stress tensor and other turbulent properties, allowing for a closure of the governing equations.

The idea behind the classical formulation of Detached Eddy Simulation (DES), proposed by Spalart in 1997 [14], was to combine RANS and LES in a single simulation. In this approach, thin shear flow attached regions are resolved using RANS and a turbulence model, while detached turbulent unsteady regions, where eddies are not much smaller than the scale of the geometry, are solved using LES. Since its introduction, there have been many improvements in this type of formulation. The one used in this thesis is the IDDES formulation, which was initially proposed by Shur in 2008 [13] and later refined and adapted to the K-Omega SST eddy viscosity turbulence model [3]. The capabilities of this latest formulation have recently been compared to more conventional LES and RANS approaches [4]. It was found that a RANS approach tends to be inaccurate in correctly predicting the qualitative features of wakes behind notchback road vehicles. On the other hand, the IDDES method has shown excellent consistency with LES results, even on coarser grids.

In all the simulations, the following finite volume method schemes have been employed:

**Convection** :

**RANS/URANS** second-order upwind

**IDDES** second-order upwind *(inizialization only)*

**IDDES** hybrid second-order upwind/central scheme

**Diffusion** : second-order upwind

The second-order upwind scheme allows for second-order accuracy while introducing artificial dissipation, which aids in solution stability in RANS formulations. For this reason the second-order upwind scheme was also utilized to quickly dampen initial transient oscillations in IDDES. The second-order upwind scheme is the most accurate for steady-state calculations, while the central-differencing scheme, with its kinetic energy-preserving properties, is suitable for LES. Therefore, the hybrid second-order upwind/central scheme is a good choice for a hybrid RANS/LES formulation like IDDES.

## 2.3 Turbulence model

Solving the RANS closure problem introduced in the previous chapter means finding a relationship between the Reynolds stress tensor and the mean flow field. This is where turbulence models come into play. Most of the commonly used turbulence models today are based on the Boussinesq hypothesis:

$$R_{ij} = \rho\nu_t \left( \frac{\partial U_i}{\partial x_j} + \frac{\partial U_j}{\partial x_i} \right) - \frac{2}{3}\rho k\delta_{ij} = 2\rho\nu_t E_{ij} - \frac{2}{3}\rho k\delta_{ij} \tag{2.6}$$

Where $\nu_t$ is the kinematic eddy viscosity and $E_{ij}$ is the mean rate of strain tensor. Substituting $R_{ij}$ into eq. (2.4) give:

$$\rho \left( \frac{\partial U_i}{\partial t} + U_j \frac{\partial U_i}{\partial x_j} \right) = \frac{\partial}{\partial x_j} \left( \rho \left( \nu + \nu_t \right) \left( \frac{\partial U_i}{\partial x_j} + \frac{\partial U_j}{\partial x_i} \right) - P\delta_{ij} - \frac{2}{3}\rho k\delta_{ij} \right) \tag{2.7}$$

From Equation eq. (2.7), it is clear where the name *"Eddy viscosity models"* comes from. The Boussinesq hypothesis assumes that the presence of the Reynolds stress tensor can be interpreted as an increase in the total viscosity acting on the mean flow. ddy viscosity turbulence models, such as the K-Omega SST two-equation model, provide a relationship between mean flow field variables and $\nu_t$.

The K-Omega SST model as described in [8] allows, through the use of the blending function $F_1$, to progressively switch from the standard K-Omega model near the wall to the standard K-Epsilon model far away from the wall. The K-Omega SST model is derived from the K-Omega BSL model where the main difference between the two is the different definition of the eddy viscosity $\nu_t$, which has been modified to account for the transport of the turbulent shear stress $R_{ij}$ that, in the Boussinesq hypothesis, is proportional to the mean rate of strain $E_{ij}$. As

shown in [7] is the best performing model in shear flows with strong pressure gradients. This makes it the most suitable model both for pure RANS simulations and for the hybrid IDDES approach, as IDDES maintains a RANS formulation near walls.

Once the turbulence model has been chosen, the wall treatment has also been selected. In particular, the K-Omega SST model described in [8] allows for a low $y^+$ approach. This approach consists in maintaining the first cell adimensional distance from the wall $y^+ < 5$ to solve the viscous sub-layer region in the boundary layer. The adimensional distance $y^+$ is defined as a function of a reference velocity usually called shear velocity $u_\tau$

$$y^+ = \frac{y u_\tau}{\nu} \tag{2.8}$$

$$u_\tau = \sqrt{\frac{\tau_w}{\rho}} \tag{2.9}$$

where $\tau_w$ is the wall shear stress and is proportional to $\frac{\partial U}{\partial y}\Big|_{y=0}$. With the assumption of turbulent flow and low $y^+$ the following wall functions have been used for all non-slip walls. For velocity:

$$u^+ = y^+ \tag{2.10}$$

For turbulence:

$$\omega^+ = \frac{6}{\beta_1 (y^+)^2} \tag{2.11}$$

where $\beta 1$ is a K-Omega coefficient.

$$P_k^+ = \mu_t^+ \frac{\partial u^+}{\partial y^+} \tag{2.12}$$

where $P_k^+ = \frac{\mu P_k}{\rho^2 u_t^4}$ is the adimesional production of tubulent kinetic energy, $\omega^+ = \frac{\omega \mu}{\rho u_t^2}$ is the adimensional specific dissipation rate and $\mu_t^+ = \frac{\mu_t}{\mu}$ is the adimensional turbulent eddy viscosity.

## 2.4 Boundary conditions

The domain has been identical for all simulations: a rectangular $10 \times 10 \times 65m$ domain with a constant velocity inlet, pressure outlet and a moving ground. The assumption of symmetry has been implemented by using a symmetry plane to reduce the required number of cells by half. This assumption is considered safe because it is unlikely that the geometry under consideration would exhibits asymmetric wakes with respect to the XZ plane. Far field boundaries have also been treated as symmetry planes.

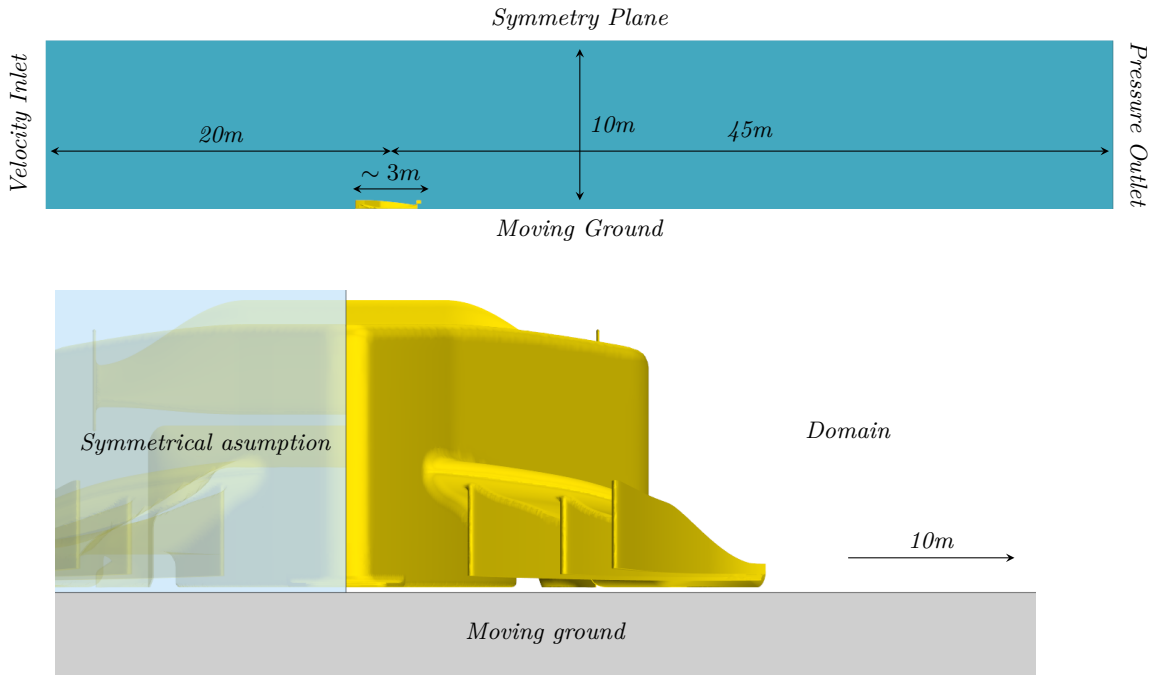


**Figure 2.4:** *Side view and front view of the computational domain and the geometry at its minumum heigth of 10mm*

## 2.5 Motion: Overset-Grids

To achieve relative motion between walls in the domain, two methods were evaluated: mesh morphing and overset grids. Mesh morphing is the easier and less computationally expensive method for small movements. However, when dealing with larger movements, mesh quality may become problematic. In contrast to the overset mesh method, using mesh deformation doesn't introduce conservation or interpolation errors, as the grid remains single. Addressing the challenge of high mesh deformation involves performing remeshing operations whenever a predefined quality threshold is exceeded, offsetting any speed advantages. Overset meshes are employed to discretize a computational domain using multiple different meshes that overlap in

an arbitrary manner.


**Figure 2.5:** *Overset domain containing the geometry inside the background domain*

They are particularly useful for problems involving large motions. After conducting a quick test of both methods, the overset method was selected to avoid the need for frequent remeshing operations.In this thesis, two separate grids were adopted: the background grid, which contains the moving ground and far-field boundary conditions, and the overset grid, which contains the geometry. Heaving motion is achieved by vertically sliding the overset grid on top of the background grid. Information exchange between the background region and the overset region is accomplished using a linear interpolation approach, as described in [1].

## 2.6 Convergence Criteria

Convergence criteria for steady RANS solutions were determined based on both residuals and body forces reports. To consider a RANS simulation as converged, all residuals needed to decrease by at least three orders of magnitude before reaching a plateau. Additionally, there should be no or negligible oscillation in the body forces.

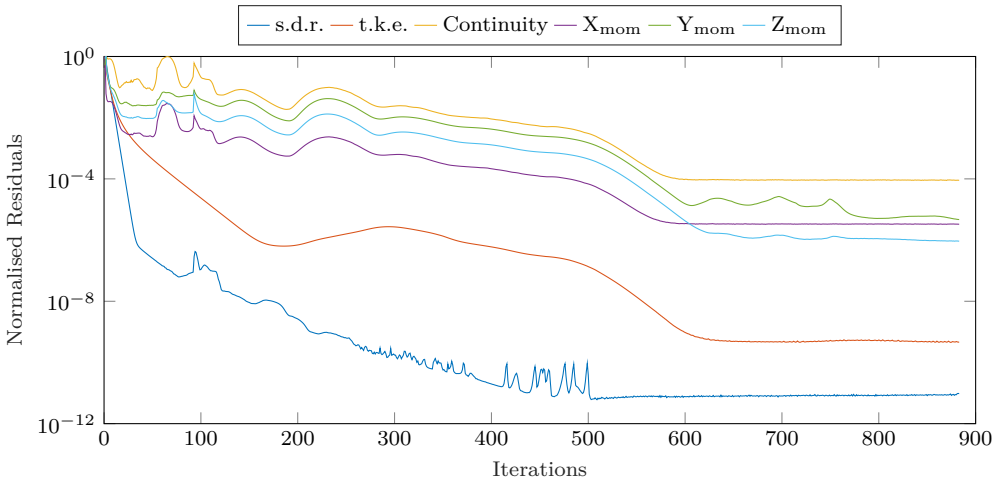


**Figure 2.6:** *Example of well converged steady RANS solution*

When examining residuals in unsteady IDDES or URANS simulations, they have limited utility in determining if each inner iteration reaches a converged solution. The formulation of convergence criteria for stopping inner iterations has proven to be unreliable, varying from one simulation to another. Therefore, a consistent approach of using a fixed number of inner iterations has been employed. Nevertheless, it has been ensured that residuals exhibited a converging trend during each inner iteration. To determine the exhaustion of the initial transient for unsteady solutions with a steady-state geometry, the moving average value of key quantities of interest, such as the magnitude of body forces and the position of the center of pressure, has been considered.

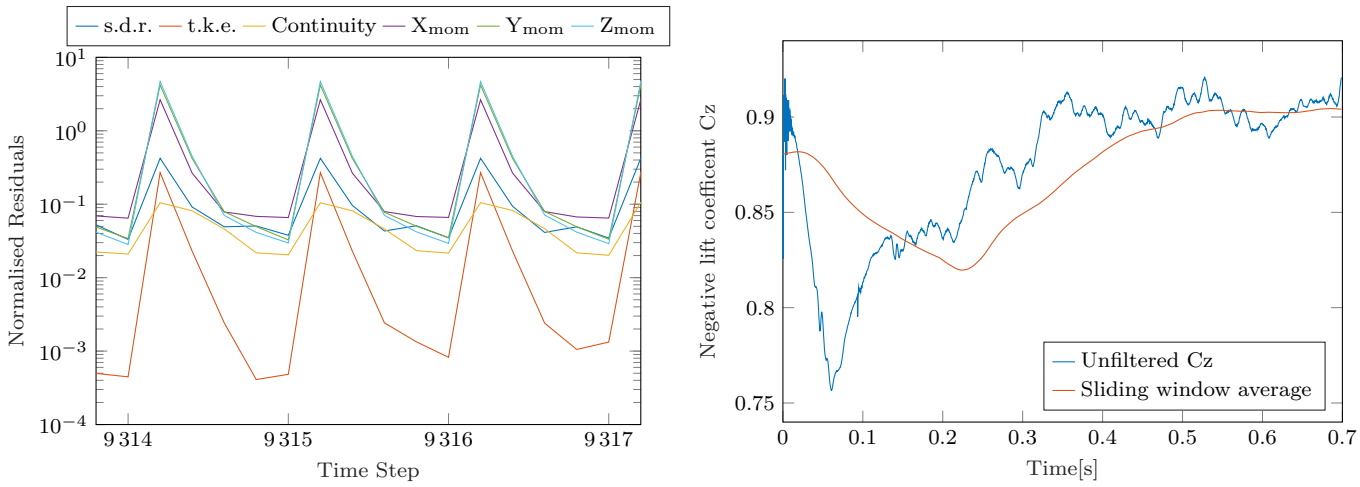


**Figure 2.7:** *Example of inner iteration converging residuals on the left and a convergent body-forces plot of unsteady IDDES solution on the right*

## 2.7 Initialization Strategy

Initialization strategy fro URANS transient has been simply done by starting from well converged steady RANS solution with same mesh and turbulence model. IDDES initialization was a bit more elaborate:

1. Starting with a well converged RANS K-omega SST solution
2. First 150 transient IDDES K-Omega timesteps using the second-order upwind convective scheme (for increased numerical dissipation)
3. Switching to hybrid second-order upwind/central scheme (for increased accuracy in LES treated domain)
4. After a steady state solution has been reached geometry motion could be activated

Transition from RANS to IDDES has been done maintaining the same mesh to avoid solution interpolation error between different grids.

# Chapter 3

# Computational Grid

## 3.1 Global strategy

The fluid domain had been discretized using a trimmed mesh for the majority of the core and an inflation layer (or prism layer) of anisotropic prismatic cells next to wall surfaces.

The trimmed mesh utilizes a template mesh constructed from hexahedral cells at the target size, from which it cuts or trims the core mesh using the initial input surface. This method allows for a high-quality hexahedral mesh with minimal skewness. It also enables a rapid, automated meshing process, resulting in reduced iteration time and memory allocation compared to the polyhedral mesh. This type of mesh is the recommended choice for highly directional flows, as diffusion errors can be minimised by alining the hexahedral grid with the flow direction. The trimmed mesh also allows for localised generation of high aspect ratio cells, which tunred out to be very useful in mitigating the high cell demand required to define the close gap between the studied geometry and the ground.

The adoption of a RANS formulation and a turbulence model allows for the use of a highly anisotropic inflation layer (or prism layer) near walls to adequately capture the mean flow features of the boundary layer. Prism layers do not only provide near wall mesh density, they also allow high-aspect-ratio cells to be used, thus providing better cross-stream resolution without incurring an excessive stream-wise resolution. Prism layers also reduce numerical diffusion near the wall. Numerical diffusion is a discretization error that smears discontinuities and steep gradients in a finite volume advection scheme. Numerical diffusion is minimized when the flow is aligned with the mesh. The use of prism layers greatly enhances accuracy as a result.

## 3.2 Volume refinement

Since the size of the trimmed cell template mesh is based on the default target surface size, the trimmed cell mesh only grows in multiples of 2 starting from the target surface size. Therefore, the actuall Cell Size $CS[m]$ in the domain core can be represented by the following formulation:

$$CS = BS \cdot \frac{16 \cdot 2^{-L}}{100}$$

Where $BS[m]$ represents the Base Size, which is a global parameter used to scale the overall grid density, and tha adimensional value $L$ is the refinement level. A value of $L = 0$ represents the "default" cell dimension used to define the body surface. Positive values of $L$ indicate grid refinement, while negative values of $L$ indicate grid coarsening. To ensure efficient resource utilization, careful consideration was taken in identifying areas where a positive refinement level $L$ was necessary and areas where a negative one could be applied.

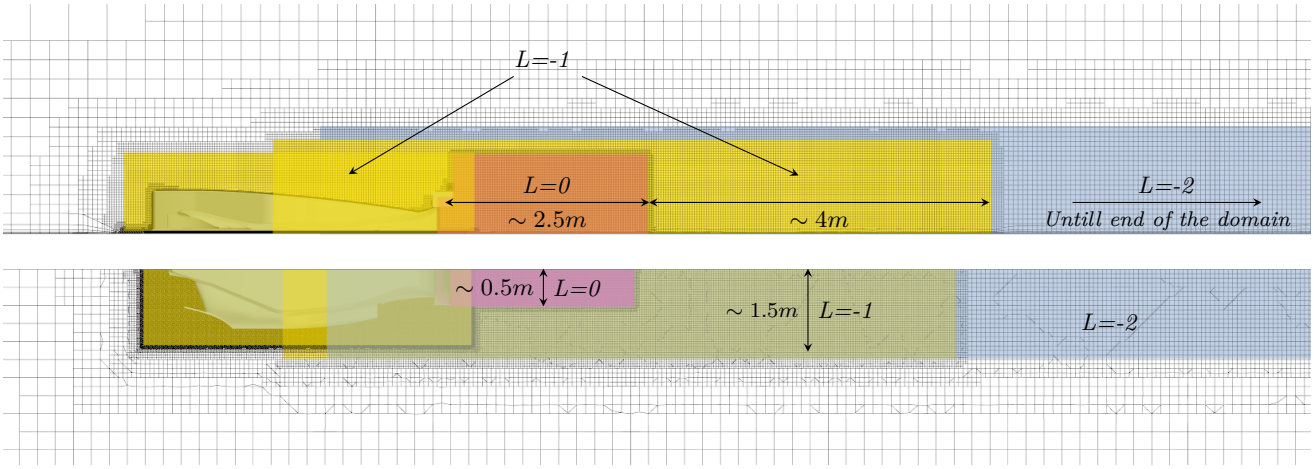


**Figure 3.1:** *Volume mesh refinement zones showned from the side and from above*

In fig. 3.1, the control volumes used to define the volume refinement zones are shown in different colors. The pink region represents the $L = 0$ refinement zone, which corresponds to the wake zone immediately behind the geometry. The vicinity of the geometry and an extended backward portion of the domain are defined with $L = -1$ cells, shown in yellow. Finally, a $L = -2$ coarser region, extending from the backend of the geometry to the end of the domain, is used to avoid abrupt dissipation of the wake structures inside the domain.

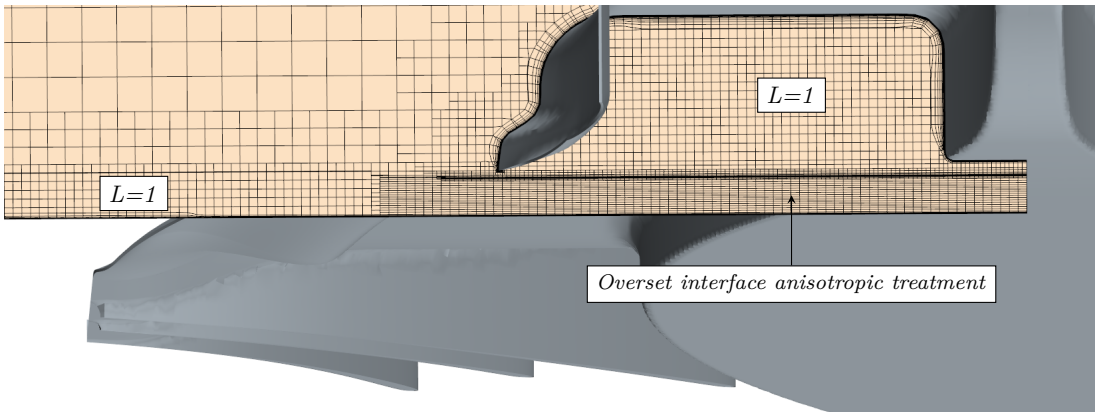


**Figure 3.2:** *Underbody treatment*

In fig. 3.2 aim to show that all the volume below the geometry is refined using a $L = 1$ refinement level.

For IDDES simulations, an Adaptive Mesh Refinement (AMR) strategy to capture fluctuating turbulent wakes was considered, tested, and subsequently discarded. The AMR solver was configured to identify and refine zones where turbulent quantities exceeded a certain threshold. This method was implemented for its ability to provide higher-resolution results and faster solution speeds compared to a static mesh.

AMR simulations demonstrated improved resolution of turbulent wakes with minimal impact on memory resource requirements. However, it was observed that AMR interventions were highly sensitive to threshold parameters and had limited influence on the body's pressure distribution. To effectively track the convective motion of the turbulence structures, frequent activations of AMR were necessary, which negated any potential time savings in the solution process. Consequently, this approach was abandoned for wake refinement applications in this thesis.

## 3.3 Wall treatment

Correctly defining the inflation layer is crucial to accurately predict forces acting on a wall and to predict flow features such as separation and vortex shedding. To ensure an accurate representation of the boundary layer, a low wall y+ approach has been adopted. The choice of such approach has imposed a constraint on the maximum height of wall adjacent cells. The inflation layer is composed of a specified number of progressively growing layers. The total thickness of this layer is defined as the distance between the surface of the wall and the surface

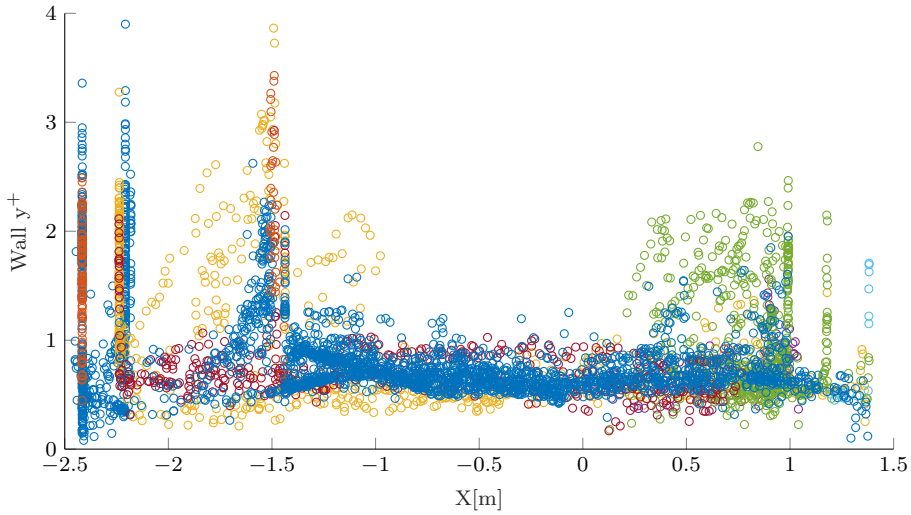


**Figure 3.3:** *$y^+$ value distribution on the surface geometry of an IDDES conveged simulation. Different colours representing different patches of the suface*

of the last layer. The thickness of these layers follows a geometric progression law, such as:

$$h_{tot} = h_0 + h_1 + ...h_{n-1} = \sum_{i=0}^{n-1} h_0 \cdot \alpha^i = h_0 \cdot \frac{1-\alpha^n}{1-\alpha}$$

Where $n$ the number of layers, $\alpha$ is the growth rate and $h_0$ is the height of the first layer. This equation is regulated by four variables, three of which are independet, also $h_0$ is constrained by the limitation imposed by $y^+ \geq 5$. The choice of the remaining two independent variables was made to ensure high mesh quality based on general criteria. These critiria being the following:

1. *Slow growthrate* $\alpha \in [1.2 - 2]$
2. *Smooth transition between prism layer and core mesh*

To quantify the *smoothness* of the core to prism layer transition, the parameter Transition Ratio (TR) has been defined as follows:

$$TR = \frac{CS}{LPLT}$$

Where $CS[m]$ is the local core cell size and $LPLT[m]$ is the last prism layer thickness (fig. 3.4). $TR$ is a "*quality*" parameter, in all the simulations done during this thesis for all transitioning cells its value has being kept between [1-5] . Growthrate $\alpha$ is both a "*resolution*" and a "*quality*" parameter since values above a certain threshold can lead to instability or divergence in the solution. Growthrate values closer to 1 coupled with a fixed target TR will cause a quick increase in prism layer number, thus an increase in total cells count. To guarantee an efficient

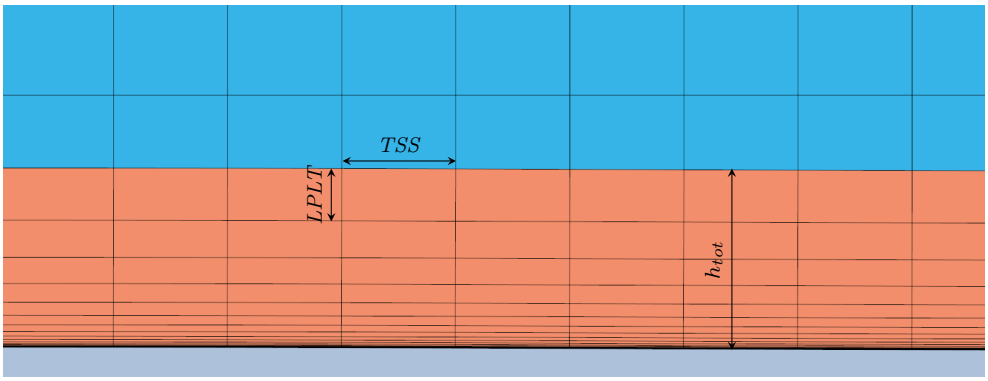


**Figure 3.4:** *Mesh section near a wall to showcase inflation layer structure*

utilization of the available resources, the geometry surface has been divided into two main groups based on prism layer "*resolution*" and "*quality*" criteria used.

| | Target max y+ | Growtrate $\alpha$ | Transition Ratio (TR) |
|---|---|---|---|
| Critical surfaces | 3 | 1.3 | [1-4] |
| Non Critical Surfaces | 5 | 1.6 | [1-5] |

Critical surfaces are those that contribute significantly to force generation. These surfaces experience strong pressure gradients and may be prone to separation. Therefore, they have been treated with a highly resolved and high-quality prism layer.

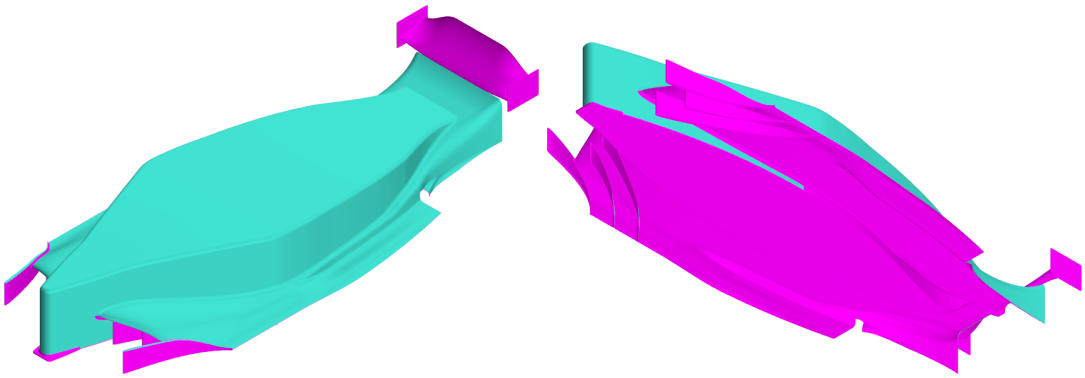

**Figure 3.5:** *In cyan, the non-critical surfaces are highlighted, while in magenta, the critical surfaces are highlighted.*

## 3.4 Ground treatment

As stated in section 3.4, the ground surface is modeled as a moving wall, whose velocity coincides with the freestream velocity. Since there is no relative velocity between ground surface and freestream flow this mean that the boundary layer will form only where flow behaviour deviates from freestream condition. This is true especially in geometry vicinity,

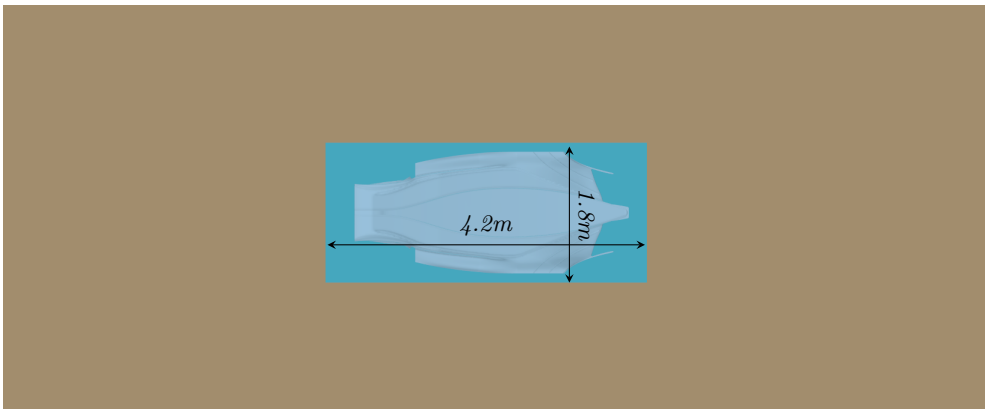


**Figure 3.6:** *In light blue, the ground patch beneath the geometry has been treated for strong interaction with the body, while in brown is the remaining ground surface treated for weak interaction.*

where the flow can be strongly accelerated by the presence of stagnation points, suction peaks and near ground vortex structures formation (fonte 4 sezione 5.3 interazione col ground, fonte 7 4.4 ). Just like stationary walls an inflation layer has been applied to the sliding ground surface too. To optimize resource allocation, the ground surface has been devided into two zones based on ground-body interaction. One group comprises areas with strong ground-body interaction, while the other includes areas with weak interaction (fig. 3.6).

| Interaction strengt | Target max y+ | Growtrate $\alpha$ | Transition Ratio (TR) |
|---|---|---|---|
| Strong | 5 | 1.6 | [1-5] |
| Weak | 5 | 2 | [1-5] |

The table above provides details on the properties of the prism layers in these two zones.

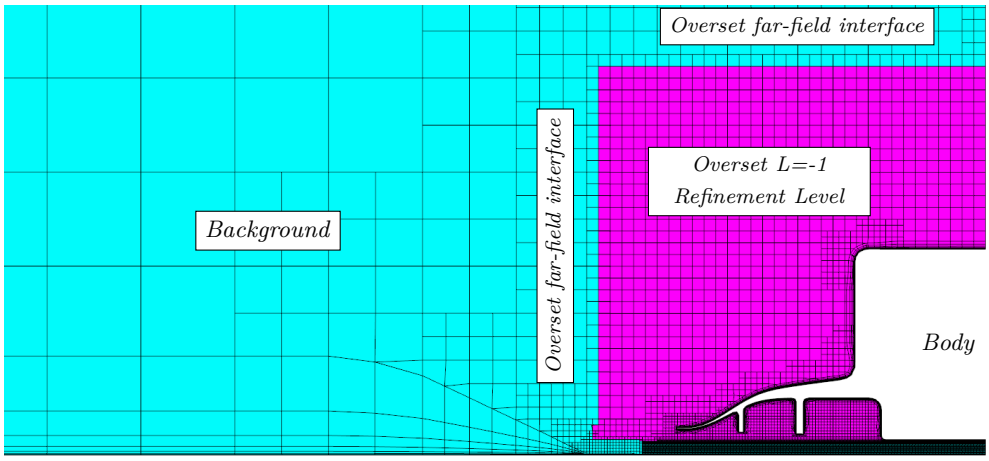


**Figure 3.7:** *Mesh section along the Y-Z axis illustrating grid coupling between overset domain and Background domain*

## 3.5 Overset interface treatment

Particular attention has been devoted to interface quality between the overset region and the background region, especially in the close ground proximity side. On the far-field sides of the interface, the sole criterion enforced was that the cell sizes between the overset region and the background region had to be identical (fig. 3.7). Complying with this criterion was relatively straightforward, thanks to the grid's uniformity in the distant regions away from the geometry. Regarding the ground-side interface, relying solely on the grid uniformity criterion was found to be inadequate. It was observed that during heaving motions, the conversion of acceptor cells into active cells and vice versa introduced considerable noise into the pressure field underneath the body, resulting in significant fluctuations in pressure-related reports (fig. 3.8).

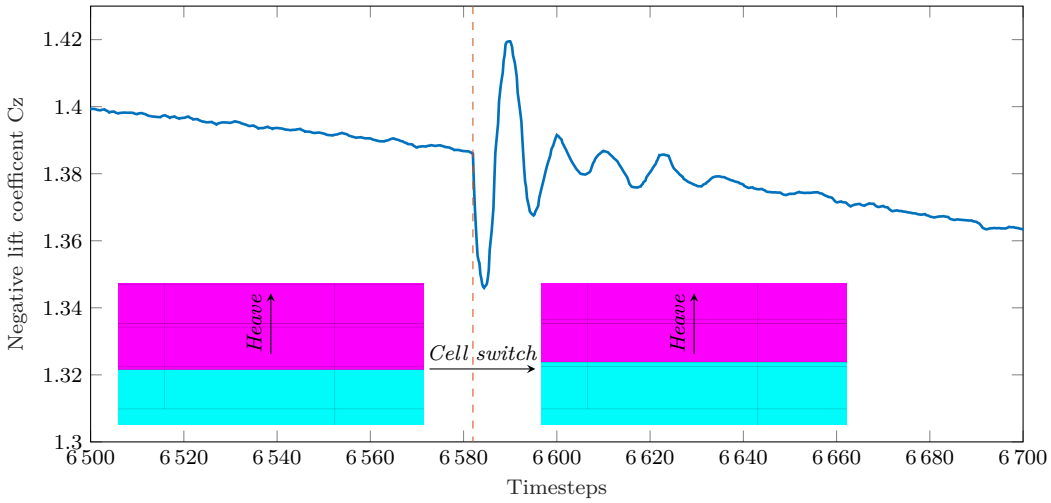


**Figure 3.8:** *Showcase of active/inactive cell switcing induced noise on Lift reports.*

Similar fluctuations, although smaller in magnitude, have been observed in published results from [1]. The high magnitude observed in the application during this thesis is likely caused by the extreme proximity of the overset interface to the geometry. The number of time steps required to dissipate these fluctuations depended on their magnitude, which was related to the vertical cell dimensions of cells along the ground-side interface where strong pressure gradients were occurring. As this phenomenon not only affects readings but also impacts the entire flow field, a series of strategies were implemented to mitigate this issue:

1. Avoid having prism layer cells as acceptor cells since prism layer cells are difficult to control.
2. Increase gap-wise cell resolution through the use of anisotropic cells. Especially in areas where steep vertical pressure gradients exist, which include:
    - Volumes below minimum height part surfaces, such as endplates, hull and fence edges.
    - Volumes where strong vortex structures exist.
3. Adoption of adaptive mesh refinement strategies to maintain adequate interface quality during overset movement.

Ground-side interface cells consist of both isotropic and anisotropic cells. All the anisotropic cells used in the core mesh, except for transition cells, had the following dimensions:

$$XSide = YSide = BS \cdot \frac{16 \cdot 2^{(-L_z+2)}}{100}$$

$$ZSide = BS \cdot \frac{16 \cdot 2^{-L_z}}{100}$$

Where $L_z$ is analogous to the refinement level $L$ used for isotropic cells in section 4.2, the difference being that parameter $L_z$ is defined only for anisotropic cells and refers to the refinement level along the z-direction.

$$AspectRatio = \frac{Xside}{ZSide} = \frac{Yside}{ZSide} = \frac{2^{(L_z+2)}}{2^{L_z}} = 4$$

The fixed aspect ratio of 4 has been chosen as a limit value to achieve a good z-resolution in critical areas of the interface without introducing concerns about mesh quality related to excessively high aspect ratios. This choice was made due to the limitations of the trimmed mesh, which does not allow for aspect ratios between 4 and 8. Using a value of 8 would have required special care to ensure mesh quality. Gap refinement for the ground-side overset interface can be represented by the 2 cases showed in fig. 3.9 and fig. 3.10 in which 4 different types of treatments can be distinguished. In particular:

**Typer 1:** Far from the body there is no necessity of any consideration about interface refinement.

**Type 2a:** Presence of gradients non negligible but not strong enough to justify anisotropic treatment so cells remains isotropic at refinement level $L = 1$.

**Type 2b:** Strong gradients due to body suction peaks the or presence of near ground vortices therefore requiring $L_z = 3$

**Type 3:** Strongest gradients and minimum body-ground clearance therefore $L_z = 4$ *(This refinement has been done only in proximity of the interface using an adaptive mesh aproach)*

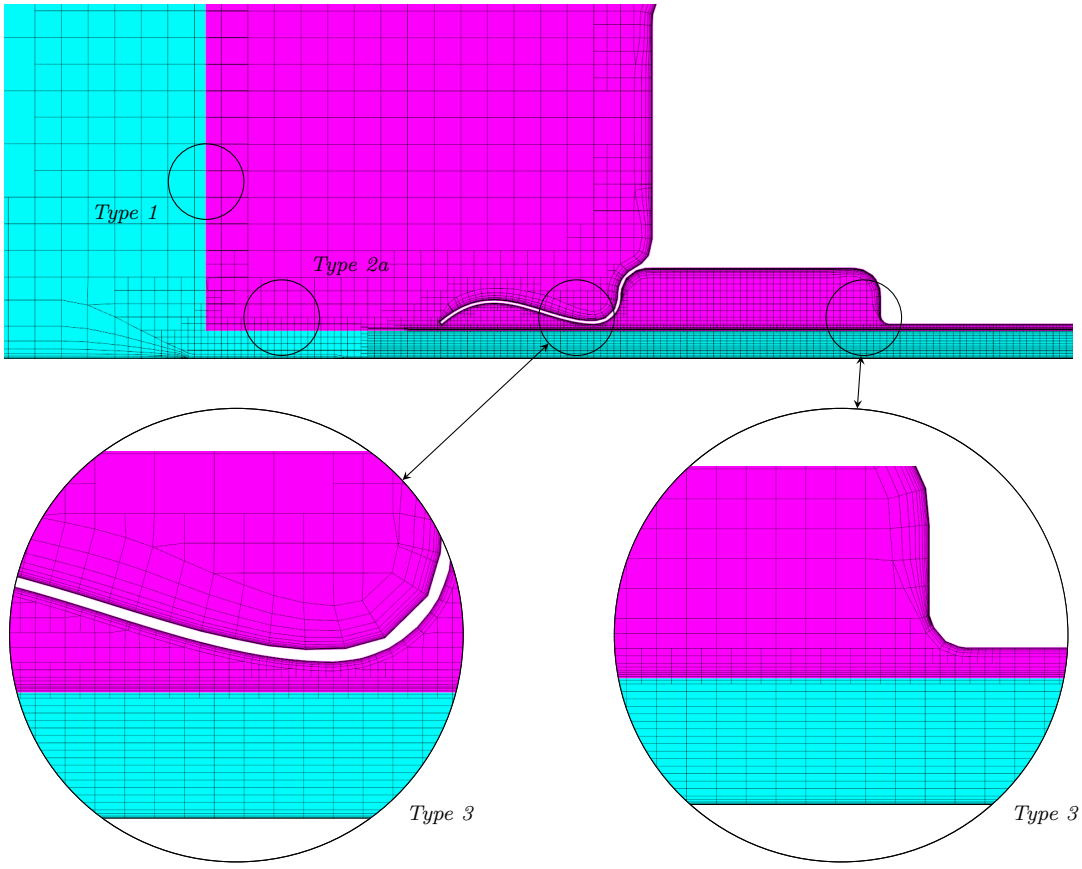


**Figure 3.9:** *Showcase of the different treatment for different parts of the overset interface for a Y-Z section of the complex IDDES case.*

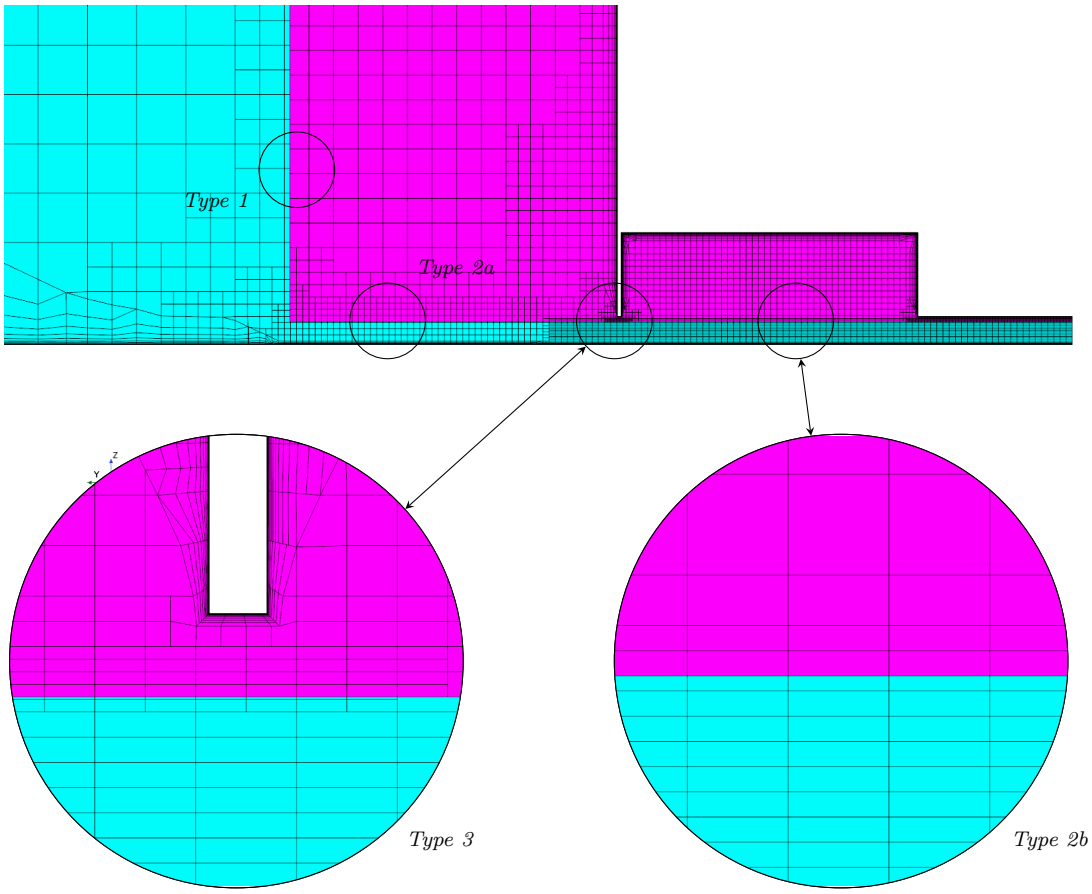


**Figure 3.10:** *Showcase of the different treatment for different parts of the overset interface for a Y-Z section of the simple RANS case.*

In fig. 3.9 , can be see that the entire surface beneath the body of the complex geometry has been subjected to type 3 adaptive anisotropic refinement. This decision is based on the presence of substantial vortex structures inside the channels, and the utilization of adaptive refinement aims to accurately capture and analyze the intricate flow patterns and vortex dynamics in this area. In contrast, in fig. 3.10, the portion of the interface in the middle of the channel was sufficiently treated with a type 2b refinement. the portion of the interface in the middle of the channel was sufficen to be treated with a type 2b. In order to guarantee that interpolation occours always between core cells and never with prism layer cells the following scheme has been adopted for surfaces at minimum body-ground clearance:

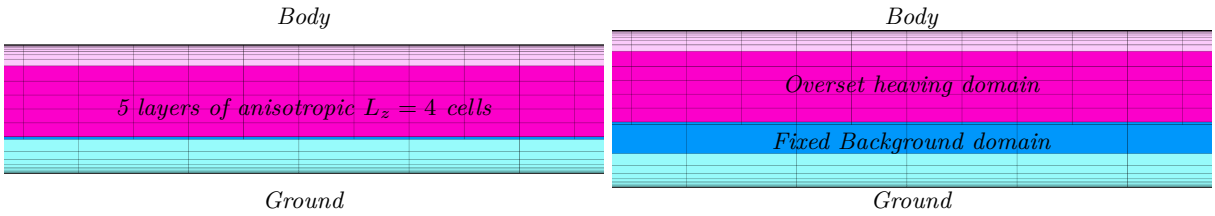


**Figure 3.11:** *Y-Z mesh section at minumum ride height of 10mm on the left and 12.5mm ride heigth on the rigth*

As shown in fig. 3.11 this scheme consists in having at least 5 non prism layer cells from the border of the interface and the start of the inflation layer. Given the fixed minum ride height of 10mm. This imposes a constraint on the values of the total prism layer height for surfaces at minimum body-ground clearance, both on the body side and on the ground side. The use of $L_z = 4$ allows for a reduced prism layer total height without compromizing TR, whose importance has been discussed in the previous section.

For geometries with large surfaces at minimum height, the increase in the number of cells caused by the use of anisotropic cells with $L_z = 4$ is very high. To ensure that this type of cell is used only near the interface and not across the entire oscillation range, an adaptive mesh approach has been used. The AMR has been set to intervene only when the movement of the overset domain causes a change in active cells count, this means the solver gets triggered only when there is the need to refine a a row of $L_z = 3$ into $L_z = 4$ (fig. 3.12).

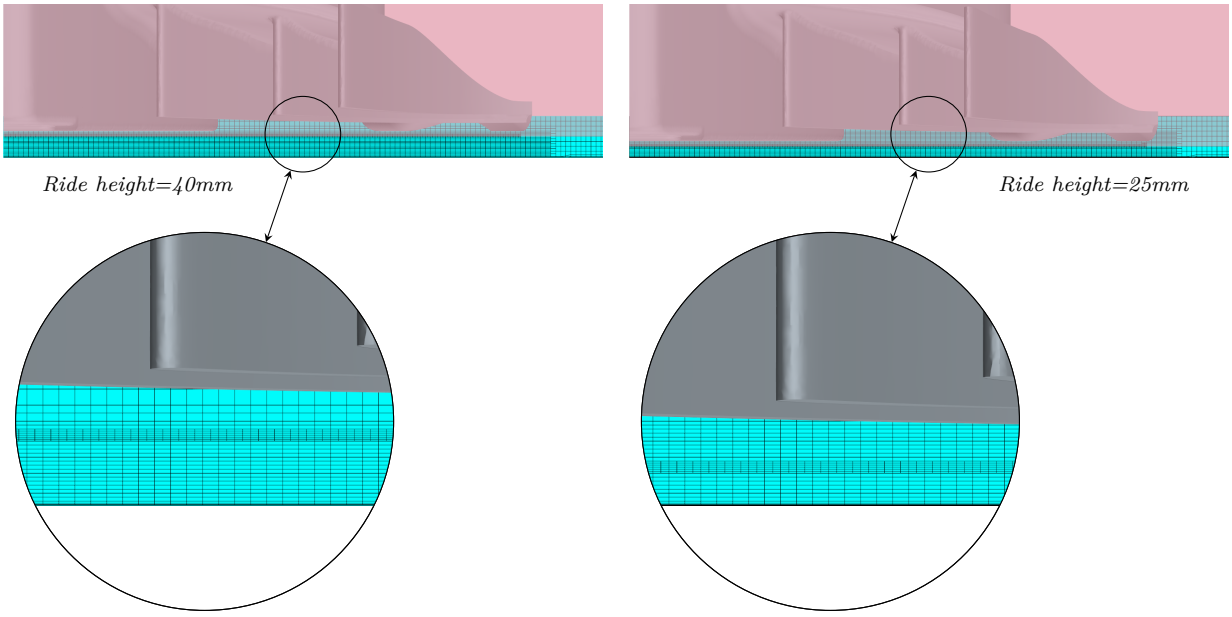


**Figure 3.12:** *Y-Z section of the background mesh at 2 different ride height to show the adapted $L_z = 4$ anisotropic cells following the lower overset interface*

# Chapter 4

# Solution time optimization

In this chapter the work done in order to optimize total solution time will be higlighted.

## 4.1 Grid independence analysis

A grid independence analysis study was conducted on the complex geometry by performing multiple RANS simulations with varying grid densities. The grid structure remained consistent with the description provided in chapter 3, with the only adjustable parameter being the base size, denoted as $BS$ in section 3.2. The base size directly determines both surface and volume resolution, and it indirectly influences the number of prism layers required for each surface to maintain the transition ratio ($TR$) within the threshold specified in section 3.3 . This approach is employed for both the URANS-based simulations and the IDDES-based simulations.

## 4.2 Time-step Independence analysis

Implicit schemes are unconditionally stable, meaning that there is no need to satisfy any particular time-step criteria to achieve a converging solution. However, it is essential to note that while implicit schemes are unconditionally stable, they are not unconditionally accurate. As a good practice, even for implicit schemes, it is often recommended to ensure that the Courant CFL (Courant-Friedrichs-Lewy) number is less than or equal to 1 at every point in the domain, where:

$$CFL = \frac{Velocity \cdot TimeStep}{GridSpacing}$$

This condition helps ensuring numerical stability and accuracy in simulations. Unfortunately, satisfying this criterion was almost impossible in this case, so a time-step independence analysis was conducted to choose the optimal compromise between accuracy and solution time.

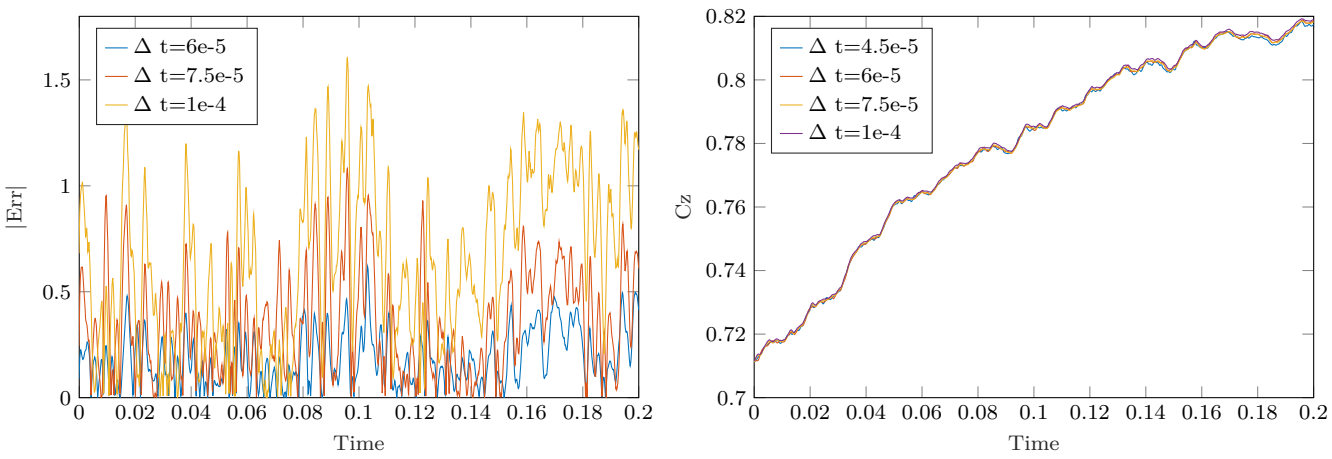


**Figure 4.1:** *Relative percentage error difference between the reference simulation with* $\Delta t = 4.5e-5s$ *for an early complex geometry*

This analysis was conducted on the IDDES simulations with a steady-state geometry and a constant number of inner iterations set to 10. To prevent solver instability, safe values of Under Relaxation Factors (URF) were used, with both velocity and K-Omega set to 0.7. As the SIMPLEC pressure-velocity coupling algorithm was employed, pressure relaxation is not specified since it is embedded in the algorithm. These measures were adopted to isolate error caused by temporal resolution. To determine an appropriate timestep, a series of simulations were conducted. These simulations were initialized using the finest timestep considered, and the difference in overall force generation relative to the finest timestep was calculated after a simulated time of 0.2 seconds

As shown in fig. 4.1 a timestep of 7.5e-5 seconds exhibits less than a 1% deviation in the Cz reading within respect to the reference simulation done with a timestep of 4.5e-5 seconds in the considered time interval. The error remains within an acceptable range even for a timestep of 1e-4 seconds. Therefore, a timestep of 7.5e-5 seconds has been chosen as a suitable compromise for IDDES simulations. This choice is also influenced by the fact that further reducing the time resolution would not significantly improve solution speed due to the need to increase the number of inner iterations to achieve convergence at each timestep.

Another point of concern when choosing the timestep for simulations involving moving geometries through sliding grids is to ensure that during motion, no overset interface cell takes less than 2 timesteps to move from one background cell to another. In this case, CFL-related limitations have been found to be much more demanding in terms of time resolution.

## 4.3 Inner iteration tightening

A good practice for choosing the number of inner iterations is to ensure that each inner iteration reaches an adequate level of convergence. The convergence speed for the implicit temporal scheme,

coupled with a segregated SIMPLEC solver, can depend on factors such as:

1. Mesh quality
2. Timestep value and Courant number distribution in the domain
3. Turbulence model
4. Solvers relaxation

This step was taken as an additional refinement in solver settings to improve solution speed. Starting with the reference solution that used a timestep of 7.5e-5 seconds presented in section 4.2, Under-Relaxation Factors (URF) were incrementally increased until instability was observed. After identifying a stable set of URF, a similar approach to the one used in section 4.2 was employed to determine the combination of URF and inner iteration numbers that strike a balance between accuracy and speed. This combination was found to require 5 inner iterations with both under relaxation factors for velocity and K-Omega set to 0.9.

# Chapter 5

# CFD model validation

CFD model Validation was performed using publicly available results. However, it is important to note that most of the heaving bodies in ground effect results are limited to 2D computational experiments, as seen in articles [10] and [11]. The behavior of the geometry considered in this thesis differs significantly from the one of a 2D geometry.

In particular, the stall height for a 2D geometry is much higher. For example, the results cited in [10] and [11] stop at $h_{\min} = h_0 - a = (0.16 - 0.08)c = 0.08c$, where $h_{\min}$ is the minimum gap between the ground and the section during heaving oscillation, $h_0$ is the mean gap, and $a$ is the oscillation amplitude, all expressed as a measure of the chord length $c$. This means that when scaling these results to a 3m chord length, the minimum height considered in [10] and [11] is $h_{\min} = 0.08 \cdot 3000mm = 240mm$, a value 24 times higher than the 10mm minimum height considered in this thesis.

Due to the absence of data from simulations or physical experiments regarding 3D low aspect ratio heaving bodies in close proximity to the ground, quantitative validation of the heaving results has proven to be infeasible. Therefore, validation will be limited to a qualitative assessment by comparing the observed 3D behavior in this thesis with the known 2D behaviour. Data related to 3D steady geometries in close ground proximity is available. In studies such as [2] and subsequently in [5], the effects of vortices trapped between a flat plate and a moving ground were investigated through wind tunnel experiments. In these experiments, forces were measured along the vertical and longitudinal

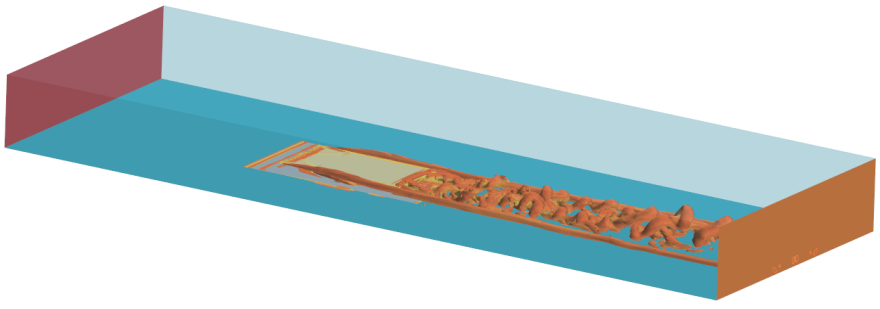

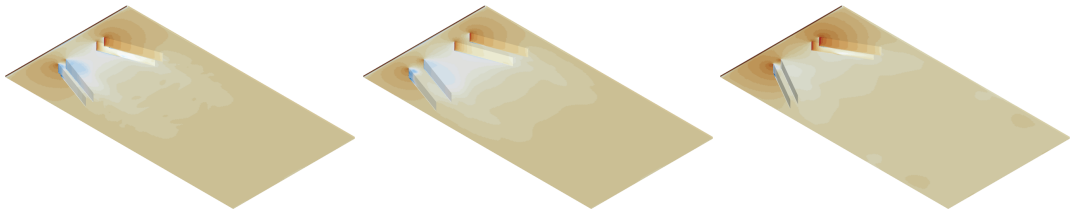

**Figure 5.1:** *On the top the purpously built domain to replicate [2] wind tunnel dimensions and features. On the bottom the 3 different set of fences tested*

directions at a speed of $120mph \simeq 53.65m/s$ for various ground clearances, with a minimum clearance of $h = 0.0042c$, where $c = 762mm$ is the length of the plate tested. Scaling the problem to a more representative cord $c = 3m$ it gives a scaled ground clearence of $h = 12.6mm$. Results obtained in [2] and [5] thus provide valuable data for the validation of the CFD model described in the previous chapters.

Validation has been performed by recreating the wind tunnel experiment published in [2] within the simulation environment. A comparison has been made for a range of clearances ranging from $h_{min} = 0.0042c = 3.24mm$ to $h_{max} = 0.084c = 64mm$ for three different configurations of vortex generators. Two of the sets considered had $\beta = 20°$ but different spacings between vortex generators $d$, while the last set had a different $\beta = 30°$. Experimental data has been compared with the IDDES solver using exacttlu the same overset mesh approach described in previous chapters. Due to the difference in geometry dimensions between this case and the original cases for which $BS$ was decided in section 4.1, the grid size had to be scaled. Scaling was accomplished by maintaining the same number of $L_z = 4$ anisotropic cells (whose importance is described in section 3.5) between the geometry and the ground surface at the minimum gap considered. Since cell dimensions changed, time step was adjusted to achieve a similar CFL distribution in the domain compared to what was found to be optimal in section 4.2.

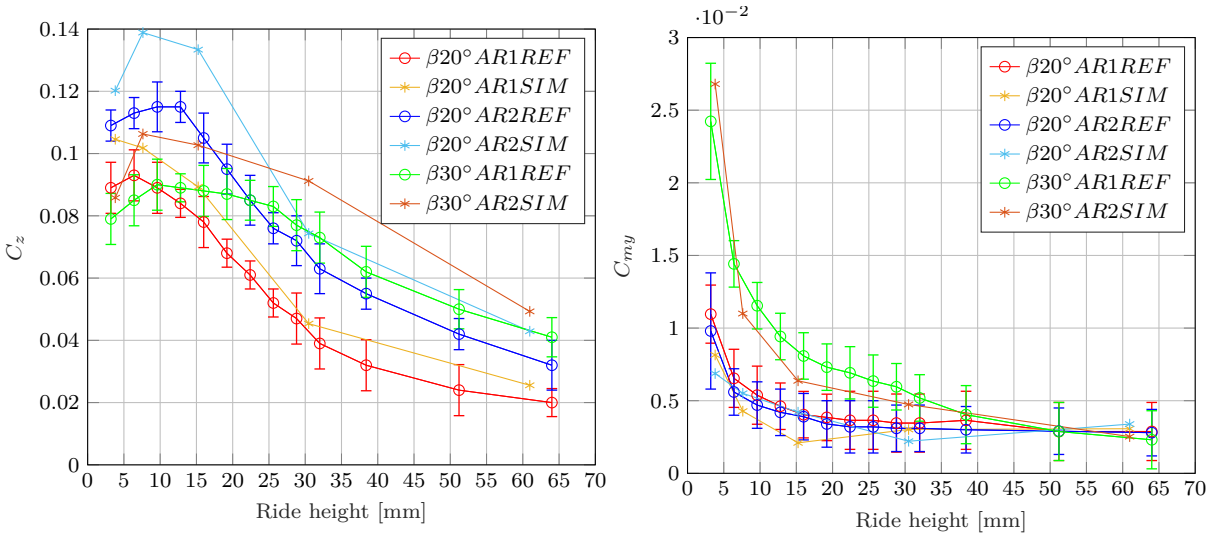


**Figure 5.2:** *Plots of the averaged negative lift coefficient Cz and Y-Moment coefficient Cmy for the three geometries. The "REF" curves represent the data found in [2], while the "SIM" curves are obtained using the IDDES CFD model.*

In fig. 5.2, it can be seen that the CFD model setup described in previous chapters provides decent accuracy when it comes to the qualitative behavior of the geometry at different ride heights, both for Cz and Cmy values. However, the measured values show an error of almost 20%. It's important to note that this error was not caused by the overset interface because simulations with $h = h_{min}$ were repeated using a single continuos grid, and no appreciable difference was observed.

This error can be attributed to differences between setups. In a study referenced as [5], the same wind tunnel setup as [2] was replicated, and a similar error was found to be caused by a slight positive angle in the plate.

# Chapter 6

# IDDES simulations of a Formula One 2022 style underbody

## 6.1 Geometrical features

The 2022 Formula One technical regulations saw some of the most significant changes in recent decades. Consequently, there were substantial differences in car designs among the various teams, as shown in fig. 6.1. At the start of the season, we witnessed a variety of approaches to car design, reflecting the different strategies adopted by teams in response to the new rules.

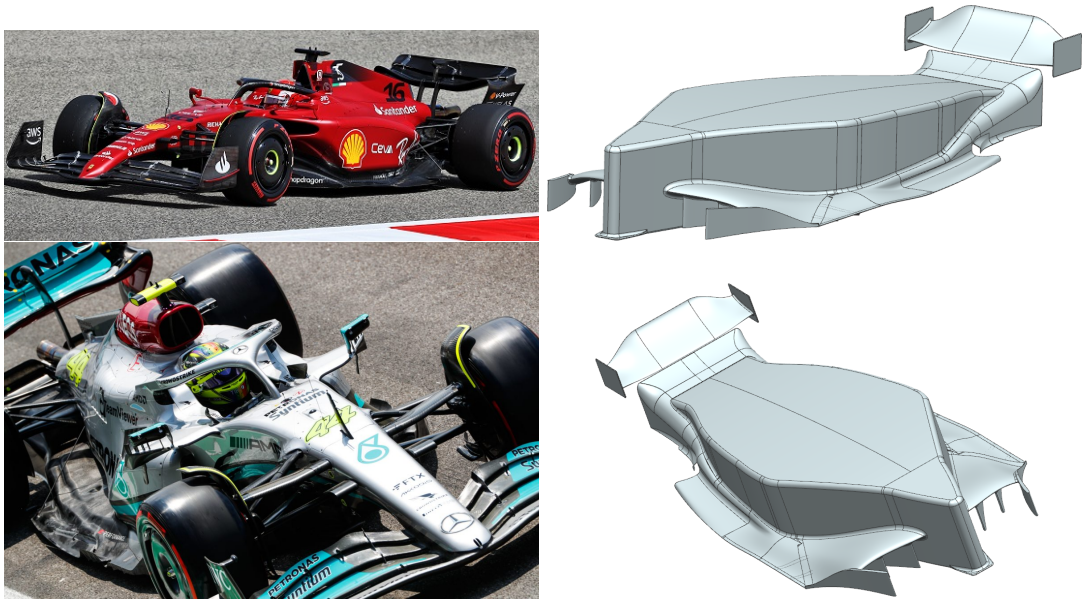

**Figure 6.1:** *Showcasing the simplified upper portion of the modeled geometry, the top features the narrow sidepods concept of the Mercedes WB13, while the bottom showcases the wide, sculpted sidepods approach of the Ferrari F1-75.*

Some teams, like McLaren and Mercedes, initially tried to replicate aerodynamic concepts from the 2021 season, intending to adapt their previous designs to the new regulations. In contrast, other teams took a completely different route. They embraced the idea of using wide and sculpted sidepods, which allowed them to achieve aerodynamic effects that were traditionally obtained using different methods under the previous regulations. Since there was no direct link between sidepod design and the porpoising issue, all surfaces above the underbody were treated as "closure" surfaces to ensure a stable and attached airflow over the top of the underbody and to the beamwing.

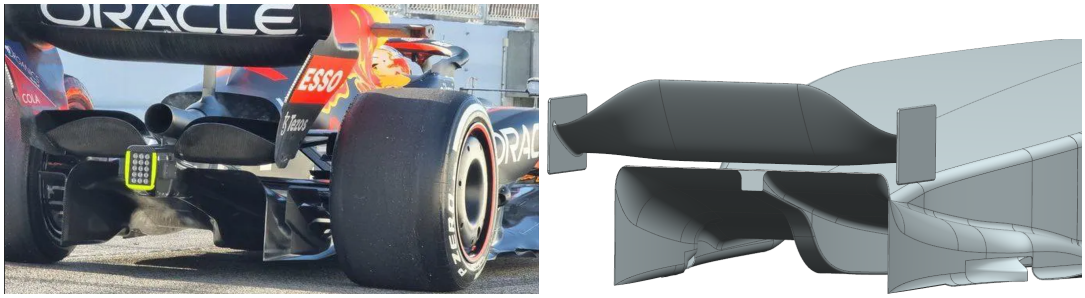


**Figure 6.2:** *RedBull RB18 viewed from behind exposing its beam wing design and a comparison with the designed CAD model.*

Another element that has undergone significant simplification in the model is the beam wing, as depicted in fig. 6.2. This component undergoes continuous evolutions and changes throughout the season, exerting a substantial influence on both aerodynamic balance (as it closely collaborates with the underbody and rear wing) and overall aerodynamic efficiency. With a few exceptions, this component typically adopts the form of a double-element wing, featuring a total of two junctions on each side. One of these junctions connects to the rear wing's endplate, while the other interfaces with the rear crash structure, with the exhaust passing in between. In this model, the beam wing has been simplified to a single, floating twisted element with two basic endplates. The section of the beam wing was a s1223 whose cord has been enlarged by $\sim 50\%$ compared to the rule-compliant design, aiming to partially replicate the absence of the rear wing.

Another characteristic feature introduced by the new 2022 regulations is the presence of vertical fences. As shown in fig. 6.3 these are rigid vertical thin surfaces with various purposes:

- Front wheel wake management
- Upper flow management
- Local vertical load generation through local expansion
- Downstream vertical load generation through:
  - *Venturi inlet flow management*
  - *Edge flow management and sealing*
  - *Downstream propagation of vortices*

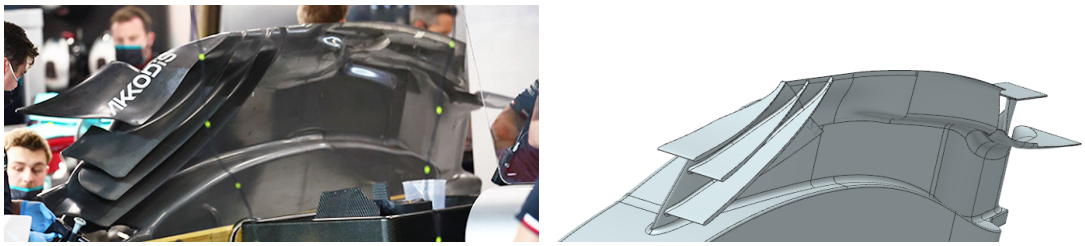

**Figure 6.3:** *Mercedes WB13 underbody design, with clearly visible fences and a comparison with the designed and tested fences.*

The 2022 Formula One technical regulations stipulate that vertical fence structures must not have a rounded leading edge. This requirement necessitates careful attention during optimization, as a sharp leading edge is less forgiving of variations in the angle of attack. The model usde in this thesis, the fences have a rounded leading edge to avoid the laborious process of optimizing the leading edge angle of attack to prevent flow separation. However, this choice results in slightly thicker modeled fences, reducing clearance between them. Additionally, to simplify the model and eliminate the need for meshing small gaps between fences, one of the four fences imposed by the technical regulation has been removed.

In order to design a geometry resembling the cars competing in the 2022 Formula One championship, a comprehensive review of the technical regulations was conducted. One of the distinguishing factors that sets apart the 2022 Formula One regulations from its predecessors is its definition based on volumes. For the first time, technical regulations have been crafted with the intention of being implemented directly in CAD software.

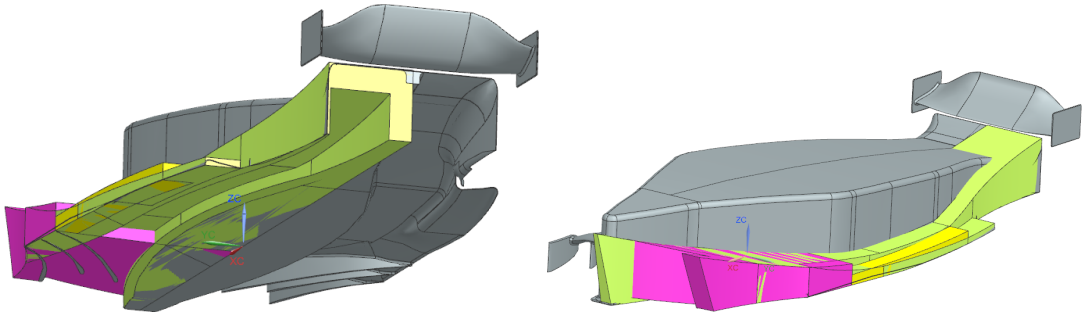

**Figure 6.4:** *Showcase of the technical regulations volumes overlapped to the designed geometry in a CAD environment.*

As depicted in fig. 6.4, the technical regulations provide explicit constraints not only on the existence volume and minimum height of both venturi channels and the floor edge and central hull, but also impose limitations on the vertical expansion slope and, more significantly, on the lateral expansion slope. These technical regulations not only dictate where the geometry must exist but also define the shape of these geometrical features, through minimum radii of curvature and continuity characteristics of specific sections. For the sake of simplicity, only the regulations related to volume constraints were

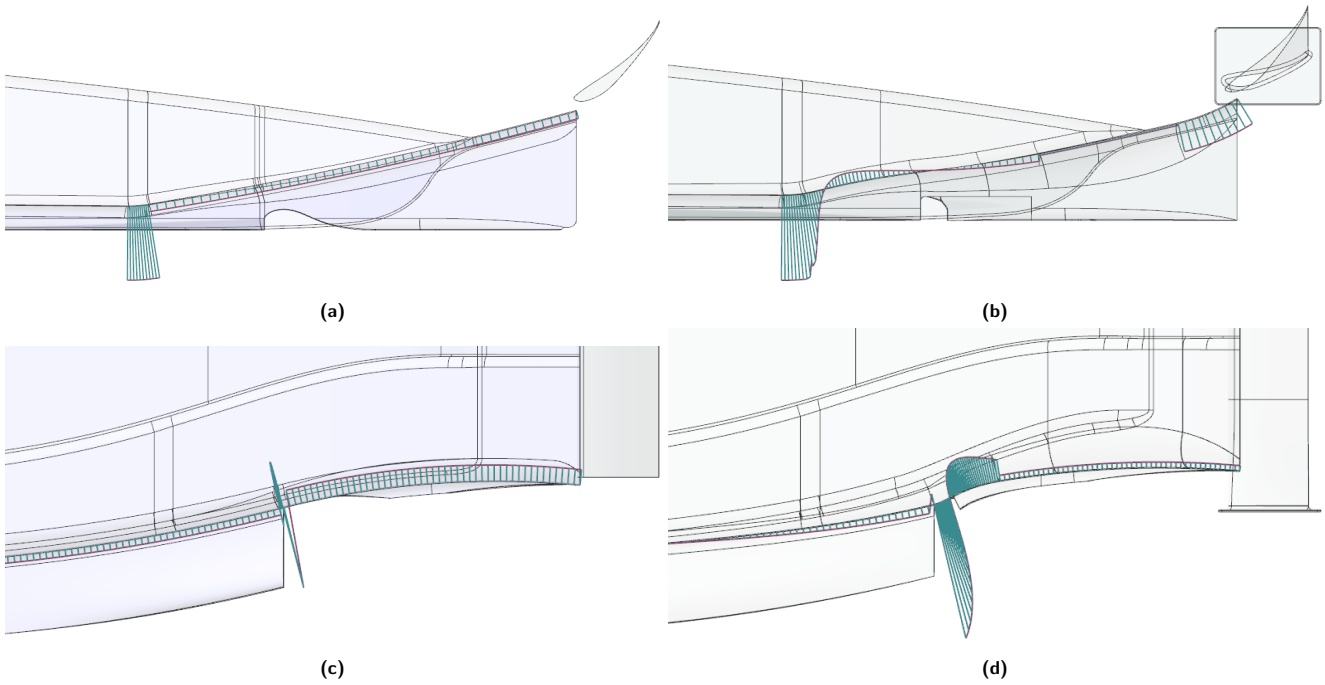


**Figure 6.5:** *Images (a) and (b) show a sideview comparison of 2 geometries highlighting a porcupine curvature analysis of the vertical expansion slope, while Images (c) and (d) show a top view comparison highliting the lateral expansion slope.*

followed during the design of this geometry. Regarding the vertical and lateral expansion slopes, several iterations were carried out to achieve a more optimal functioning of the underbody. In the early iterations of the geometry, significant fluctuations in force reports were observed. These fluctuations were primarily caused by the premature breakdown of vortices inside the expansion zone. The first iteration of the vertical slope (as shown in fig. 6.5a) featured a simple constant radius profile with another constant radius blending into the upstream channel. On the other hand, the lateral slope design is constrained by tight rules and regulations. Therefore, in the initial iteration, a straightforward sinusoidal-like shape consisting of two constant radius sections was adopted(as shown in fig. 6.5c). In the last iteration, the slopes were designed taking inspiration from shapes that are actually used in Formula One. In the new vertical slope design shown in fig. 6.5b, a single kick concave-convex profile has been employed. These types of profiles are characterized by a strong, localized suction peak at the beginning of the extraction slope, followed by a pressure recovery zone immediately after to the re-energize the boundary layer. This design also helps reduce the expansion rate in the middle portion of the diffuser, where vortex breakdown was observed to occur. Additionally, to further reduce the expansion rate in the middle zone and create a more favorable pressure gradient inside the diffuser, another constant radius kick-up was added at the end of the section. Modifications on the side extraction profile showed in fig. 6.5d were made to add a strong positive pressure gradient in proximity of the vortex brake down location.

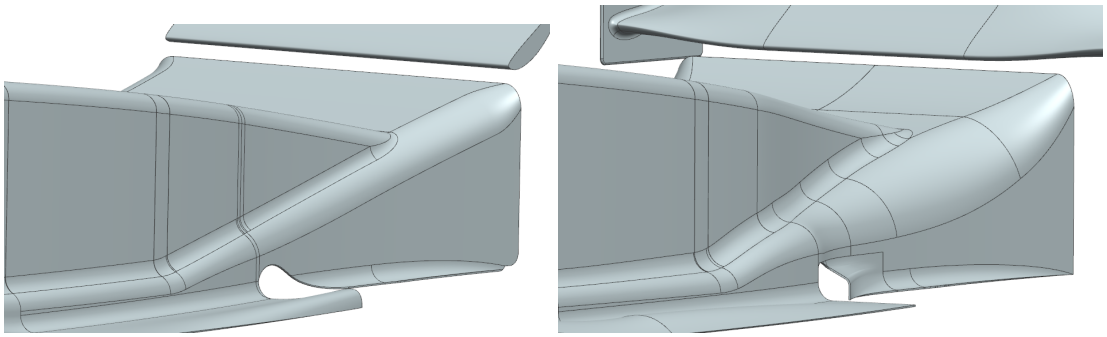


**Figure 6.6:** *Showcase of two "mousehole" tested geometries. In (a) the mousehole is a simple cut on the sidewall while (b) is a complex connected shape.*

Formula One teams in the 2022 season frequently utilized a feature known as the "mousehole" in order to manage edge flow in the sensitive area. This feature involves an opening in the side wall, as illustrated in fig. 6.6, which allows for the introduction of high-energy airflow into this critical region where vortex breakdown can lead to significant flow stability issues. Several shapes were explored in this area, ranging from a simple cut in fig. 6.6a to a more complex and connected shape in fig. 6.6b.

As a result of this optimization process, the integrity of vortex structures in the diffuser area has been significantly improved, as demonstrated in fig. 6.7c. This improvement is also evident when examining the force plot along the vertical axis. In a steady-state condition at 40m/s prior to optimization, the overall vertical forces exhibited an oscillation magnitude of nearly 10% of the total load produced, accompanied by a very slow oscillation frequency. This confirmed the unstable behavior of the macroscopic vortex structures, as shown in fig. 6.7a. In contrast, the optimized geometry exhibited a smaller oscillation magnitude at a higher frequency, in line with fig. 6.7a, which clearly shows a continuous propagation of vortices coming from downstream and a compact vortex structure that forms in proximity of the mousehole. In trying to avoid the vortex breakdown problem, an unintended consequence was an increase in the overall vertical load generated. This increase was attributed to the reduction in energy flow losses and the increase in the effective extraction area. Additionally, refinements were made in the edge geometry area, and the extraction efficiency of the beam wing, which was later adopted with endplates, also contributed to this effect.

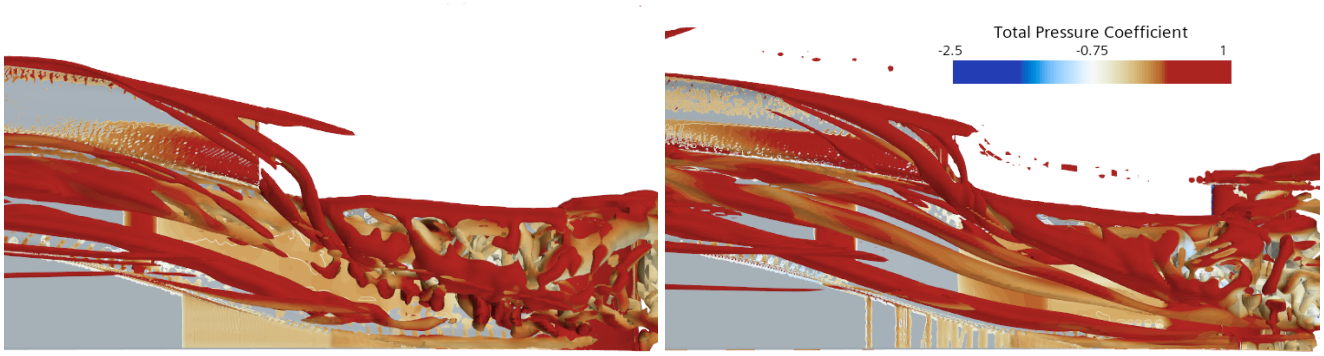


(a) (b)

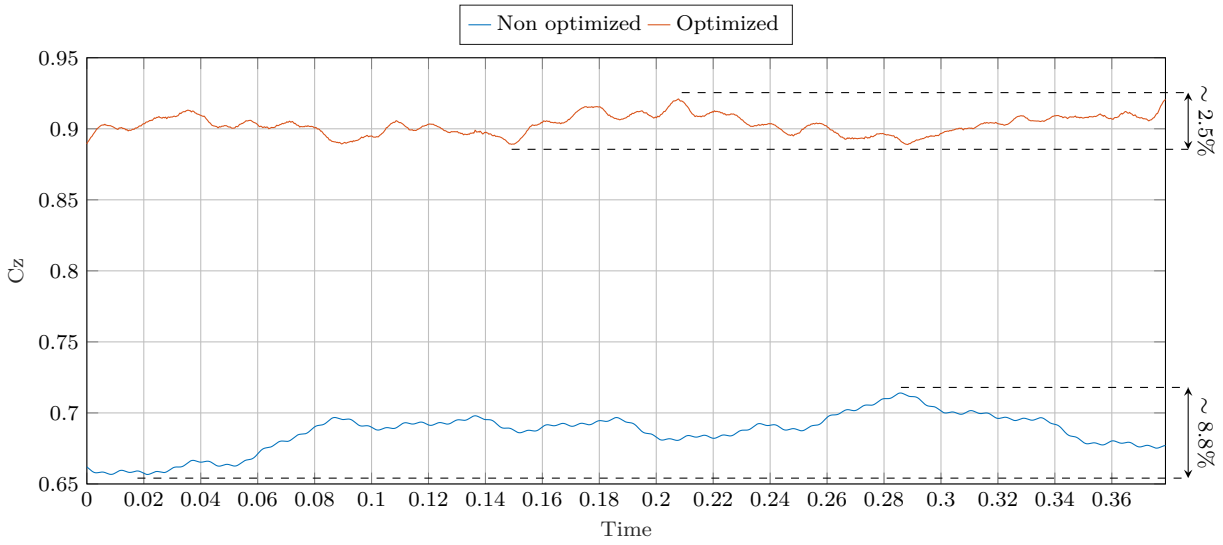


(c)

**Figure 6.7:** *Images on the top are frame captures of a view from below of the diffuser area showing a isosurface of $Q - Criterion = 5000/s^2$ representing flow vortex structures in a steady state condition at 40mm ride height at 40m/s. On the bottom instead there is the steady state Cz plot for the two geometries at 40mm ride height at 40m/s*

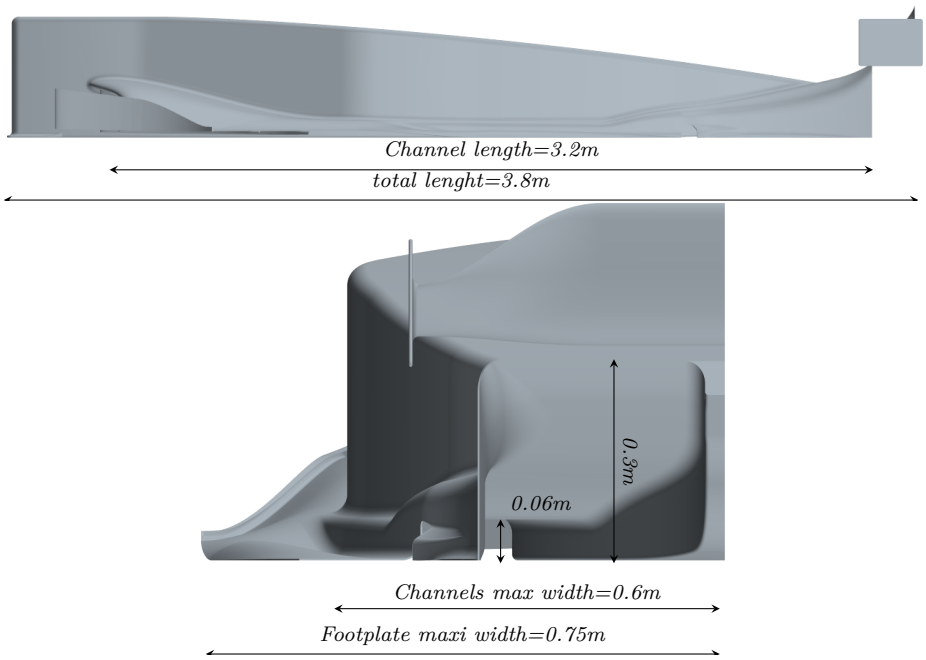


**Figure 6.8:** *Formula One 2022-like aerodynamic dimensions were considered, such as the length of the venturi channel and the maximum extension of the floor edge.*

All aerodinamic coefficients will be calculated within respect the channel dimensions and not the total dimensions.

## 6.2 Grid details

In chapter 3, the general meshing strategy adopted for all cases has been thoroughly described, so in this section, we will provide an overview of the details adopted to discretize the particular geometry described in the previous section. To determine an appropriate value of the $BS$ parameter described in section 3.2, a mesh sensitivity study has been performed following the method described in section 4.1. A value of $BS = 0.095m$ has been chosen for the complex geometry IDDES cases. This means, for example, that at an $L = 0$ isotropic refinement level, the actual cell size $CS[m]$ is:

$$CS = 0.095m \cdot \frac{16 \cdot 2^{L=0}}{100} = 0.0152m$$

And for $Lz = 4$ anisotropic refinement level cells:

$$XSide = YSide = 0.095m \cdot \frac{16 \cdot 2^{(-L_z=4+2)}}{100} = 0.0038m$$

$$ZSide = 0.095 \cdot \frac{16 \cdot 2^{-L_z=4}}{100} = 0.00095m$$

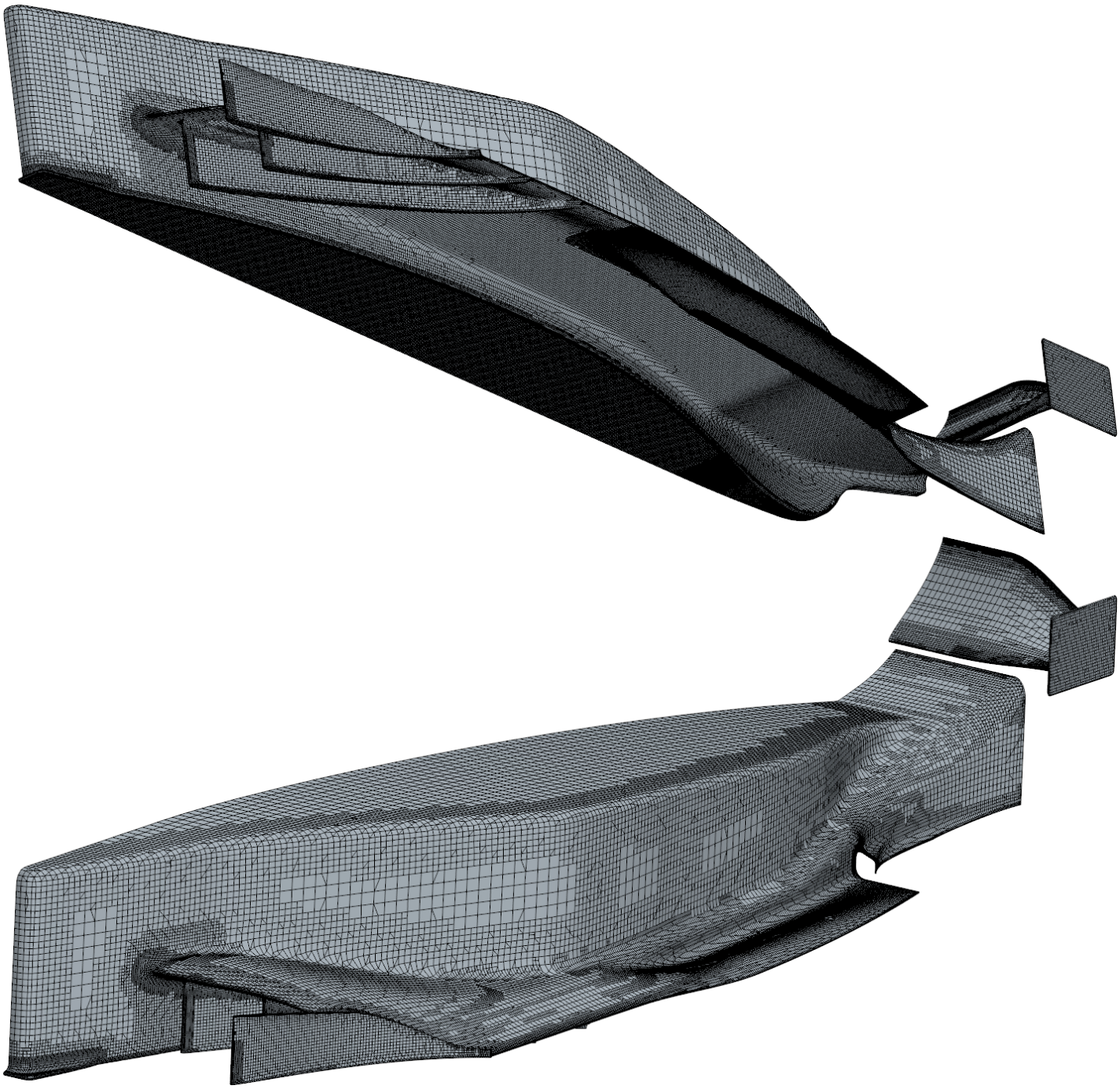

**Figure 6.9:** *Surface mesh distribution overview*

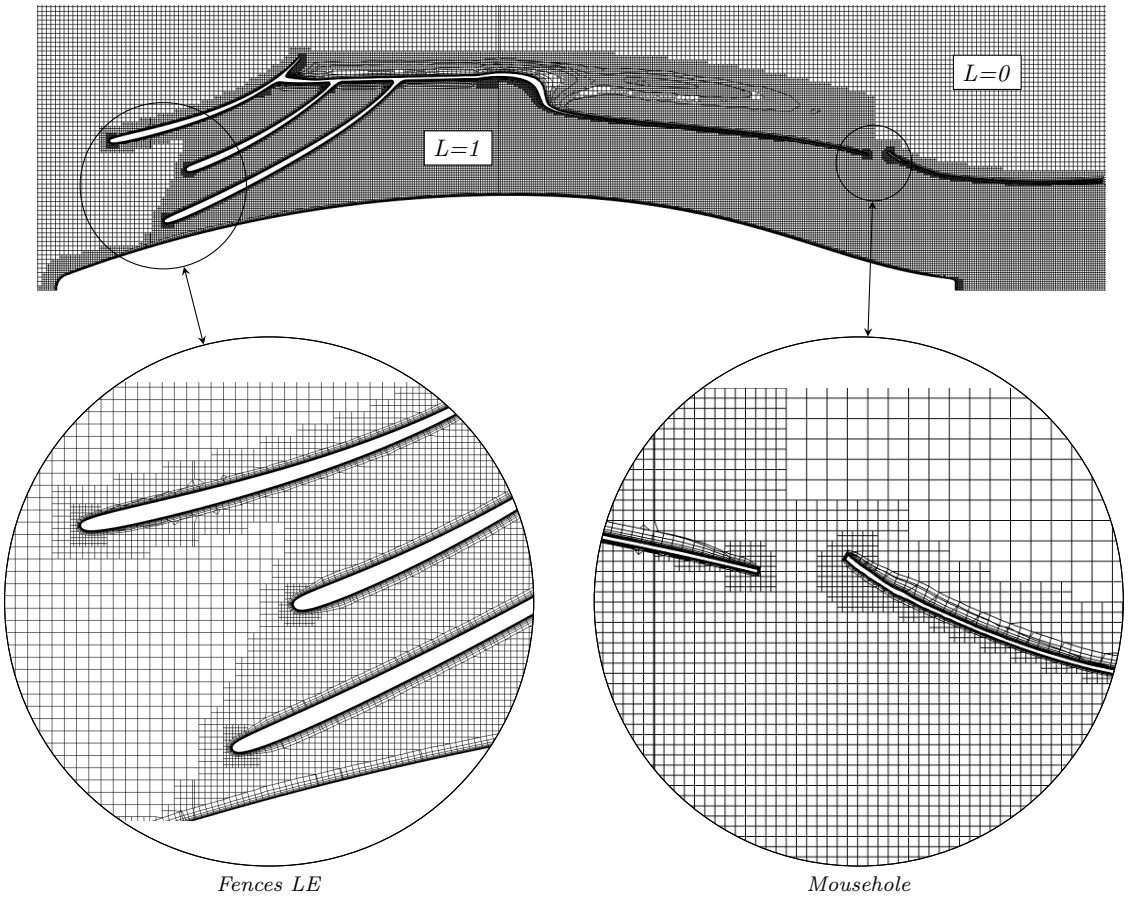


**(a)** *X-Y section cutting trough the ventury channel*

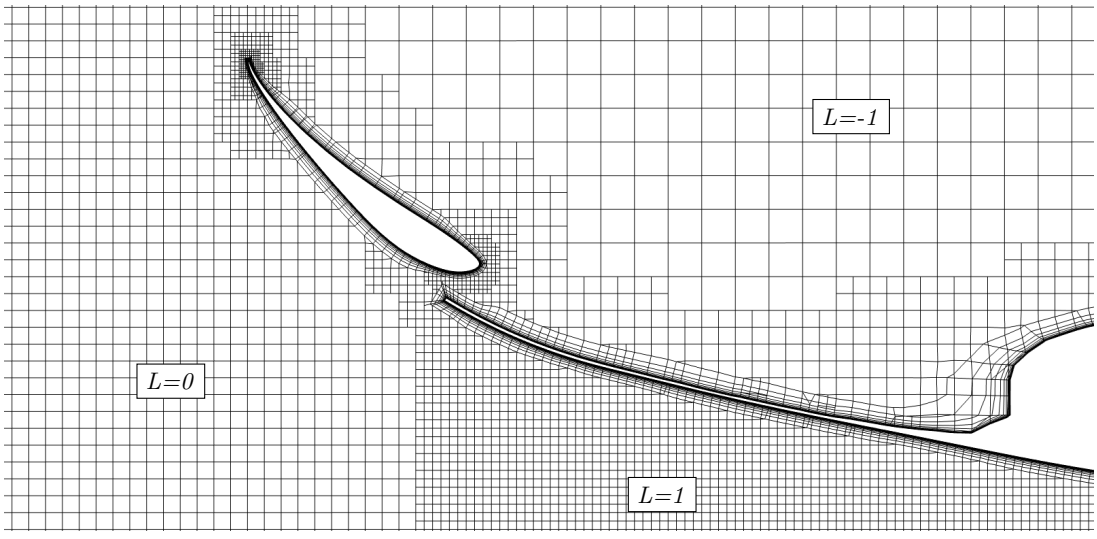


**(b)** *X-Z beam wing mesh section*

**Figure 6.10:** *Showcase of different mesh sections for the complex IDDES case.*

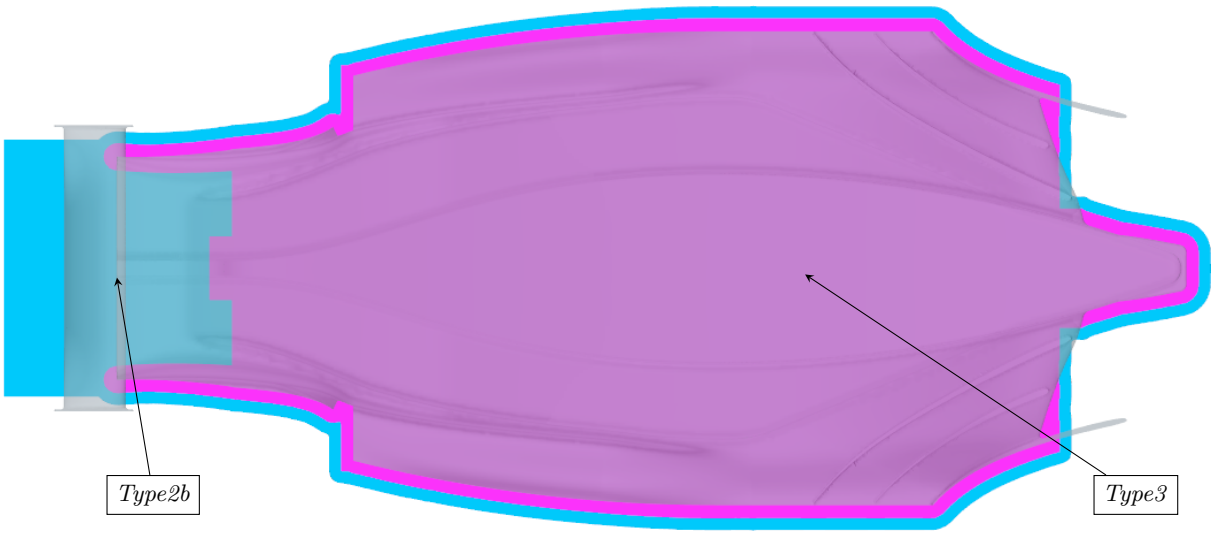


**(a)** *In cian Type 2b refinement have been aplied. In magenta a Type 3 refinement have been applied*

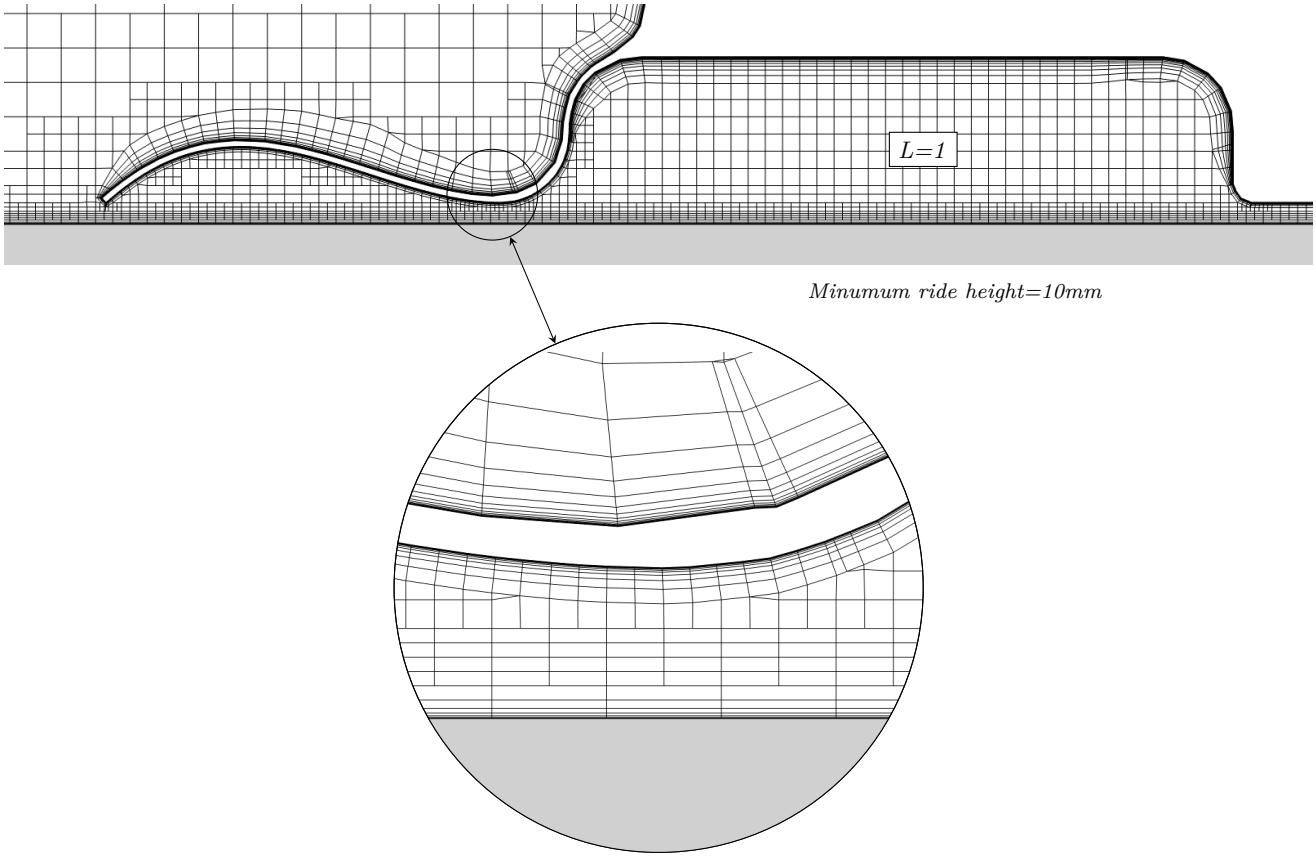


**(b)** *Y-Z mesh section showing minumum gap grid resolution with Type 3 overset interface refinement*

**Figure 6.11:** *Distribution of anisotropic treatment (referencing section 3.5) and a Y-Z section mesh at minimum clearence for the complex IDDES case*

## 6.3 Quasi-steady results

In this paragraph the quasi-static solutions of the IDDES simulations at various ground clearances will be presented. These results will provide valuable insights into the behavior of a Formula One 2022 compliant underbody, offering both quantitative and qualitative information. In fig. 6.12, we can observe how the average load generated at 40m/s by the underbody behaves in a nearly monotonic manner as the ride height varies (ride height $rh \in [10 - 40]mm$) but with clear non-linearities.

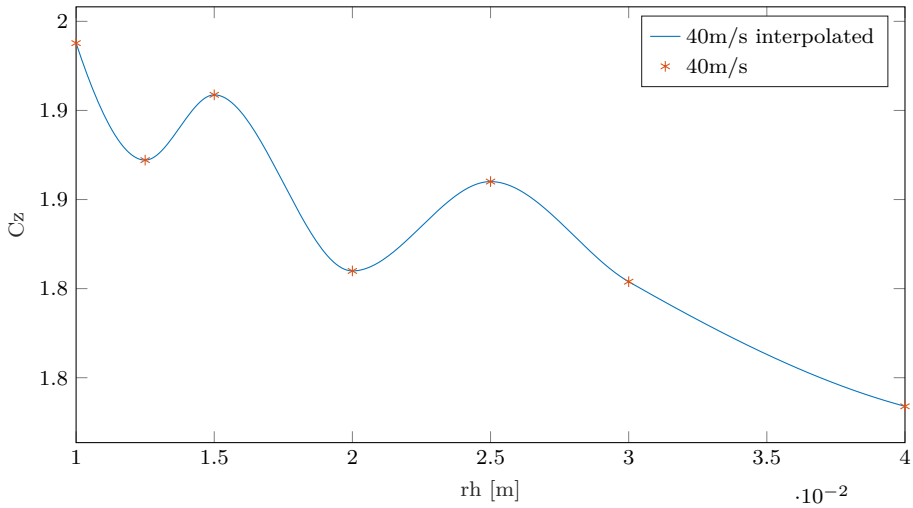


**Figure 6.12:** *Example of inner iteration converging residuals on the left and a convergent body-forces plot of unsteady IDDES solution on the right*

It must be noted that there is a parallelism between ground proximity and incidence on a stationary airfoil. When the incidence increases, more suction is generated on the suction surface and, as a consequence, more downforce. But at high angles the adverse pressure gradient becomes too high and the boundary layer starts to separate. Downforce might continue to increase up to point where separation is massive and the airfoil stalls (obviously the separation process depends on the particular airfoil, but this serves as a generic explanation). Similarly, an inverted airfoil getting closer to the ground will experience the same events trhough another mechanism called ground effect. Ground effect is an application of the Bernoulli principle, that for an incompressible, inviscid and stationary gas states:

$$p + \rho\frac{u^2}{2} + \rho gh = costant \tag{6.1}$$

This formulation of the Bernoulli equation can be applied, neglecting viscous effects, to a 2D inverted wing section at a distance $rh$ from the ground. In this situation the channel that forms between the ground and the wing can be seen as a Venturi channel (fig. 6.13).

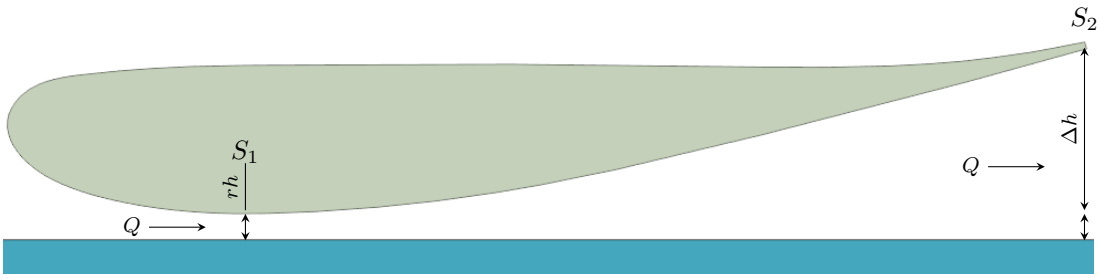


**Figure 6.13:** *Inverted 2D wing in ground effect*

For a 2D case a general section area $S_i$ can be defined as the product of its height $h_i$ and width $b_i$:

$$S_i = h_i \cdot b \tag{6.2}$$

Mass conservation law coupled with the incompressible hypothesis tells us that the mass flow $Q$ across the whole channel has to remain constant. Therefore the following relatioships can be written for the minumum height section $S_1$ and the exit section $S_2$ :

$$\frac{Q}{\rho} = u \cdot S_i = u_1 \cdot rh = u_2 \cdot (rh + \Delta h) \tag{6.3}$$

$$u_1 = \frac{u_2 \cdot (rh + \Delta h)}{rh} \tag{6.4}$$

By simply applying the Bernoulli equation eq. (6.1) and knowing that the conditions at the exit section $S_2$ have to be the freestream condition (neglecting losses and hypothesizing parallel streamlines at the exit section) the value of $\Delta p$ can be derived as follow:

$$p_1 + \rho\frac{u_1^2}{2} = p_2 + \rho\frac{u_2^2}{2} = p_{atm} + \rho\frac{u_{inf}^2}{2} \tag{6.5}$$

$$\Delta p = p1 - p_{atm} = \rho\frac{u_{inf}^2}{2}\left(1 - \left(\frac{(rh + \Delta h)}{rh}\right)^2\right) = \rho\frac{u_{inf}^2}{2}\Omega \tag{6.6}$$

with:

$$\Omega = \left(1 - \left(\frac{(rh + \Delta h)}{rh}\right)^2\right) \tag{6.7}$$

where:

$$\lim_{rh \to 0_+} \Omega = -\infty \tag{6.8}$$

$$\lim_{rh \to +\infty} \Omega = 0 \tag{6.9}$$

It is, therefore, safe to assume that the total vertical load coefficient of a 2D wing will be a non-linear function of the ride height. As for the 3D low aspect ratio case examined in this paragraph, it becomes much more chaotic, as shown in Figure 6.12. The non-linearity of $C_z$ as a function of the ride height $rh$ is due to the intricate interplay of various non-linear mechanisms that collectively contribute to the

overall vertical load. We could hypothesize that $C_z(rh)$ can be decomposed as:

$$C_z(rh) = \sum_{i=1}^{n} C_z(rh)_i$$

Where $C_z(rh)_i$ represents one of the $n$ seprate mechanisms that generate the full vertical load slope.

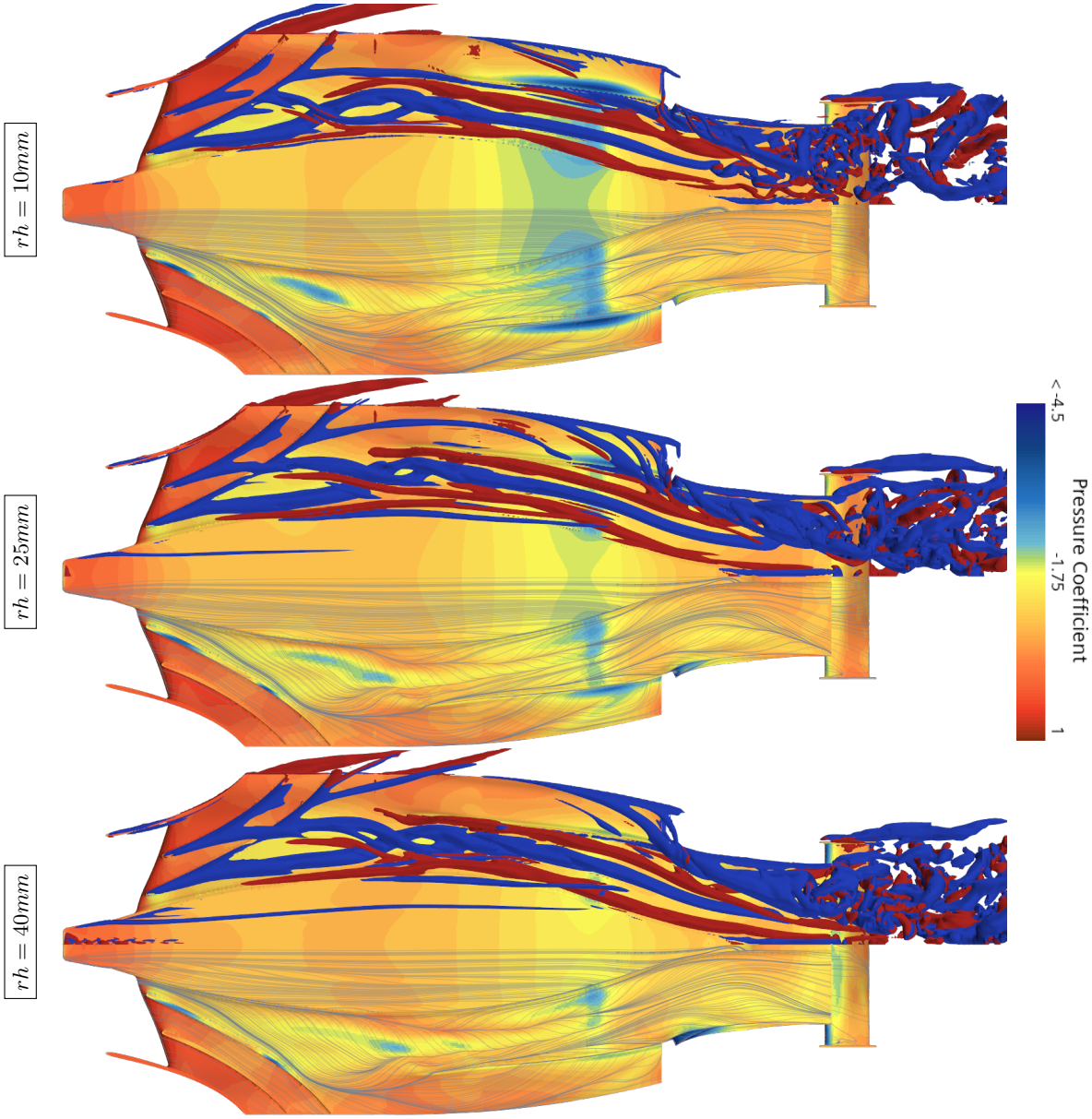


**Figure 6.14:** *Comparison between different ride heigths.The $Q - criterion = 5000/s^2$ isosurface is highligted in red and blue to show diffentent sign of te local x-vorticity. The body surface pressure distribution is shown with wall shear stress driven surface streamlines*

In the varius instances shown in fig. 6.14 it is clear that isolating each contributing component is not feasable for complex flows such tas that of a Fomula One underbody, especially because flow structures can be quite different based on different design choices. Looking at fig. 6.14 the flow show

numerous counter rotating vortices, mostly generated in the frontal fences area and propagating along the venturi channel. Numerous vortex structures are generated as a side effect of the edge opening. In this area, air is drawn into the diffuser from the side, and the shearing of the flow along the floor edge causes the formation of strong vortices. These edge vortices are, in nature, similar to the wingtip vortices of a 3D wing or the leading-edge vortices of a delta wing, with the major difference that in this case they interact both with the geometry and the ground. Just as on a delta wing, the presence of 3D structures like edge vortices is crucial for maximizing vertical load. In fact, vortices play a dual role in vertical load generation. They contribute directly to vertical load generation through a mechanism similar to the one described in [12]. Additionally, vortices promote flow attachment to the diffuser by inducing a favorable velocity field and mixing low-energy boundary layer flow with high-energy flow from inside and outside the channel.

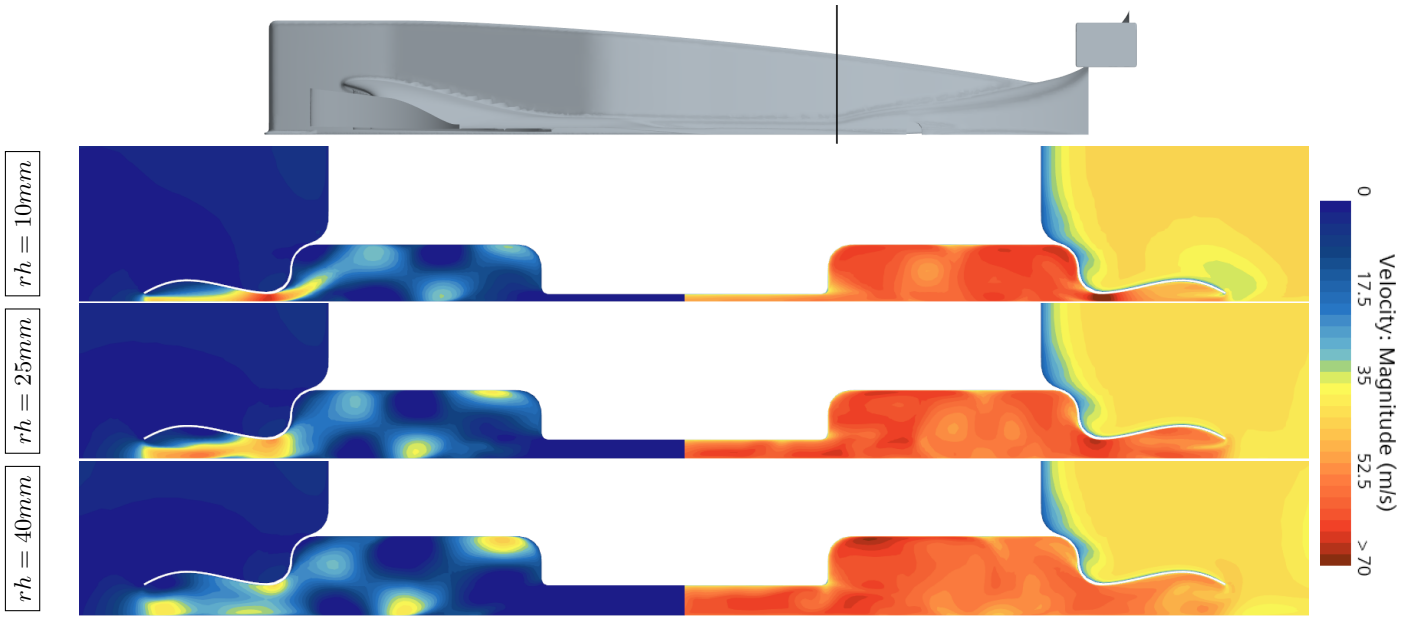


**Figure 6.15:** *Comparison of different ride heigth quasi-steady reuslts. On the right the contour plot of the velocity magnitude and on the left the horizontal velocity component(>0 if moving toward the symmetry plane). Above is shown the Y-Z section position to be right before the start of the diffuser*

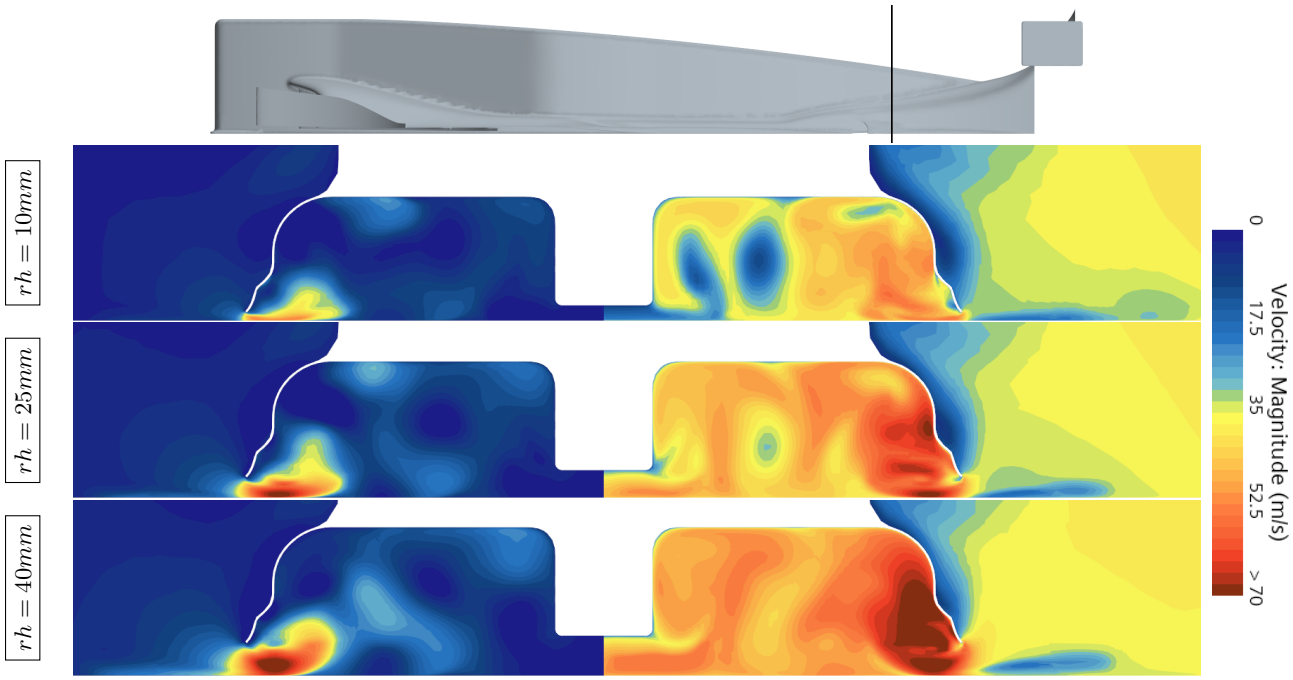


**Figure 6.16:** *Comparison of different ride heigth quasi-steady reuslts. On the right the contour plot of the velocity magnitude and on the left the horizontal velocity component(>0 if moving toward the symmetry plane). Above is shown the Y-Z section position to be in the middle of the diffuser*

Another factor contributing to the non-linearity of $C_z(rh)$ is the variation in the perceived aspect ratio of the venturi channels. The perceived aspect ratio would tend towards infinity if the edge touched the ground, resulting in the elimination of lateral infiltration and exhibiting behavior close to two-dimensionality. Comparing fig. 6.15 and fig. 6.16, it can be observed that different sections behave in opposite ways with changing ride height, depending on the local flow characteristics. In this particular case, it can be hypothesized that the mass flow through the mousehole area significantly decreases with a lower ride height. This reduction in mass flow in the area diminishes the local negative pressure peak, thus drawing less air through the edge gap.

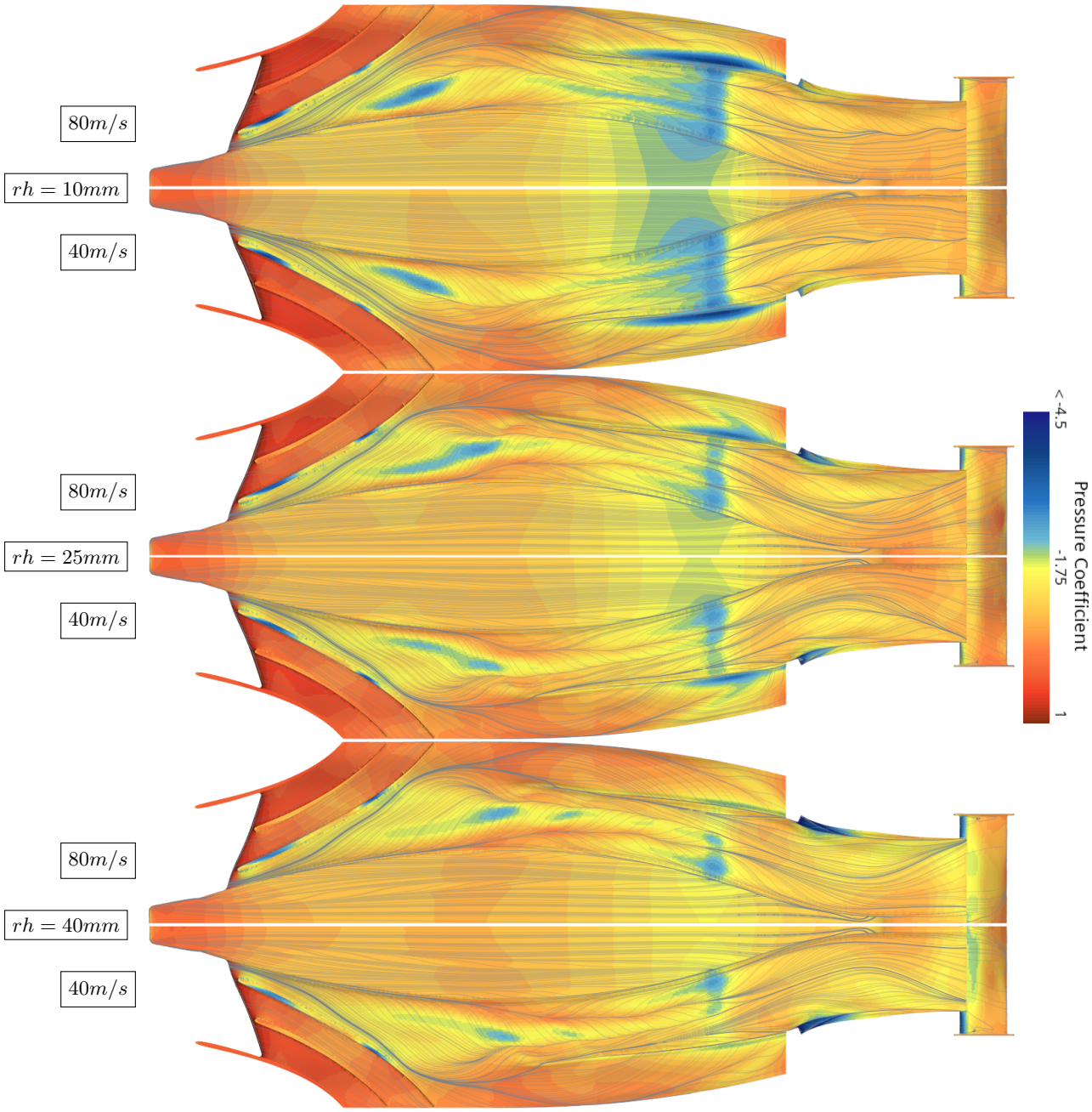


**Figure 6.17:** *Comparison between 40m/s and 80m/s results in quasi-steady conditions.The body surface pressure distribution is shown with wall shear stress driven surface streamlines*

A comparison has also been made for the same geometry at double the freestream flow to understand if there was any Reynolds number dependencies. Both the pressure distribution and wall shear stres driven streamlines in fig. 6.17are nearly identical between the two cases for all tested ride heights. This is expected given that this is a high Reynold number application and that the majority of the flow underneath the surface is mostly laminar.

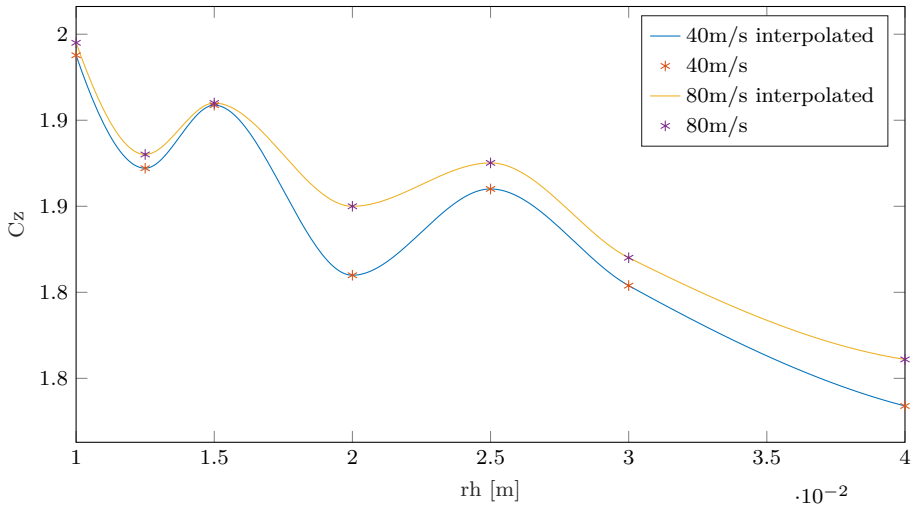


**Figure 6.18:** *Comparison between 40m/s and 80m/s quasi-steady negative lift coefficent slopes*

## 6.4 Heaving results

This paragraph discusses the flow behavior in a pure heaving harmonic condition, emphasizing differences from the quasi-steady solution discussed in the previous section. For the complex geometry heaving simulations, the full 30mm range of motion was utilized, ranging from the wood plank touching the ground condition (providing a 10mm minimum clearance, as shown in fig. 2.2) to the maximum considered ride height $rh = 40mm$. In a harmonic heaving oscillation, body position in terms of ride height $rh$ can be expressed as a function of the angular position $\theta[rad]$:

$$\theta(t) = wt + pi = 2\pi ft + \pi \tag{6.10}$$

$$rh(t) = rh_{av} + real(rh_0 e^{iwt}) \rightarrow rh(\theta) = rh_{av} + real(rh_0 e^{i\theta}) \tag{6.11}$$

Where $h_{av}$ is the mean ride height, and $rh_0$ is the oscillation amplitude. In fig. 6.19, values of the angle $\theta$ that will be sampled for the qualitative flow analysis are highlighted in red.

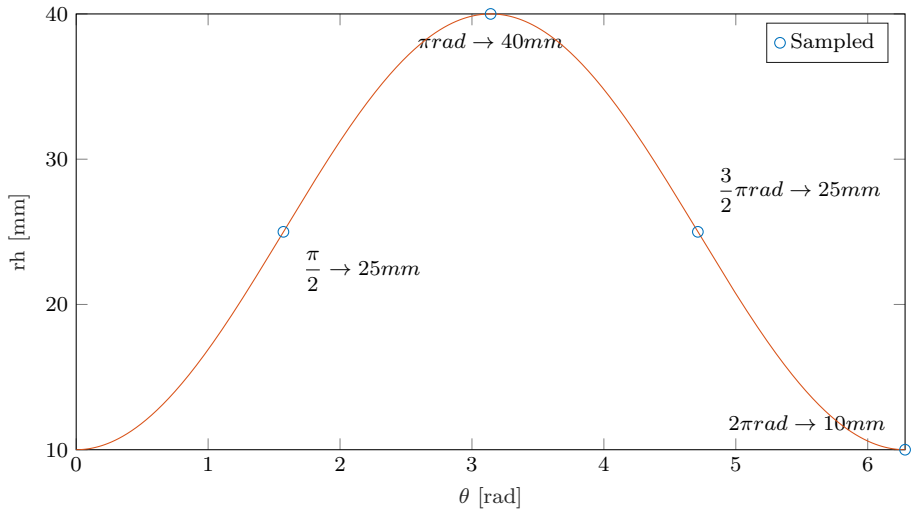


**Figure 6.19:** *Ride heigth plotted over the angle $\theta$ in rad. Higligted the sampled unsteady conditions used in this chapter*

In fig. 6.20, vertical force coefficients are presented for both the unsteady case and the quasi-steady prediction at a speed of 40 m/s. It becomes apparent that within the tested frequency range of $f \in [3-6]Hz$, the quasi-steady approach inadequately captures the forces generated during harmonic heaving conditions. Particularly noteworthy is the fact that at higher frequencies, the maximum recorded $C_z$ value increases by more than 50% than what was expected based on the quasi-steady analysis. Furthermore, as the heaving frequency increases, the amplitude of oscillation appears to diminish. The heaving forces recorded do not exhibit perfect sine wave patterns, and their phase is not in sync with the heaving motion. Both of these observations were anticipated. The distortion in sine wave patterns can be attributed to the non-linear nature of ground effect. Additionally, the phase

delay phenomenon, which is known to affect oscillating wings in freestream, results from the time required for the flow around the geometry to adjust to its new position, as described by Theodorsen in [15].

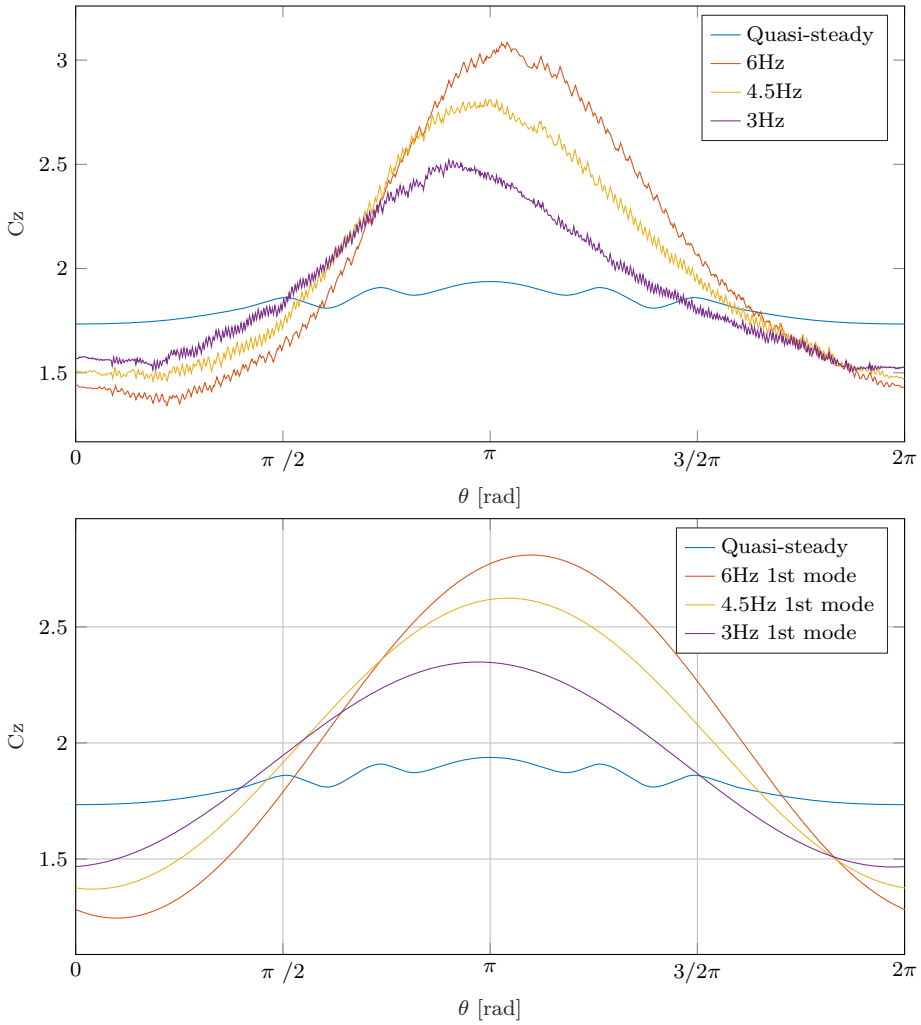


**Figure 6.20**

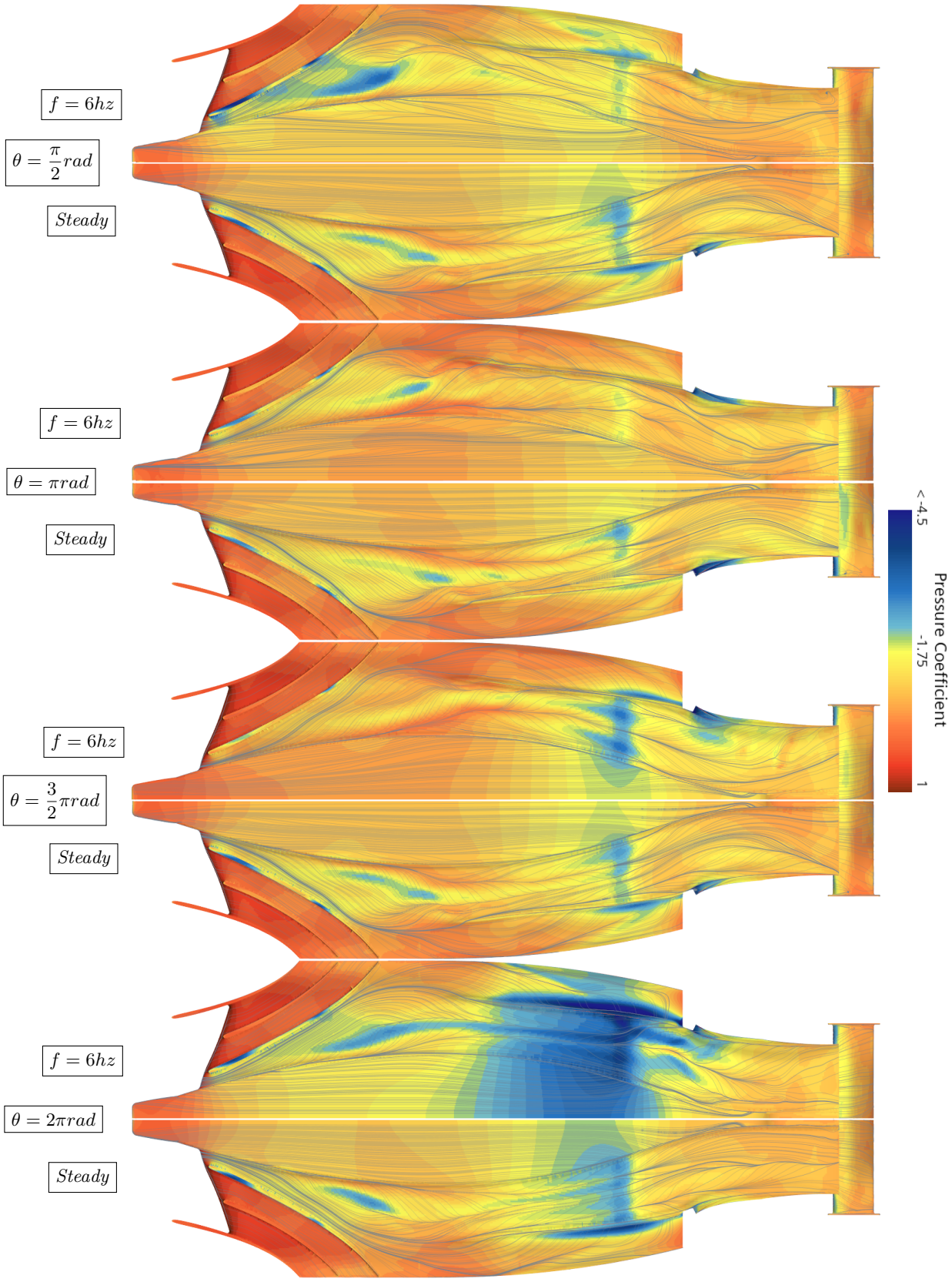


**Figure 6.21:** *Comparison between quasi-steady and unsteady 6hz 40m/s conditions. The body surface pressure distribution is shown with wall shear stress driven surface streamlines*

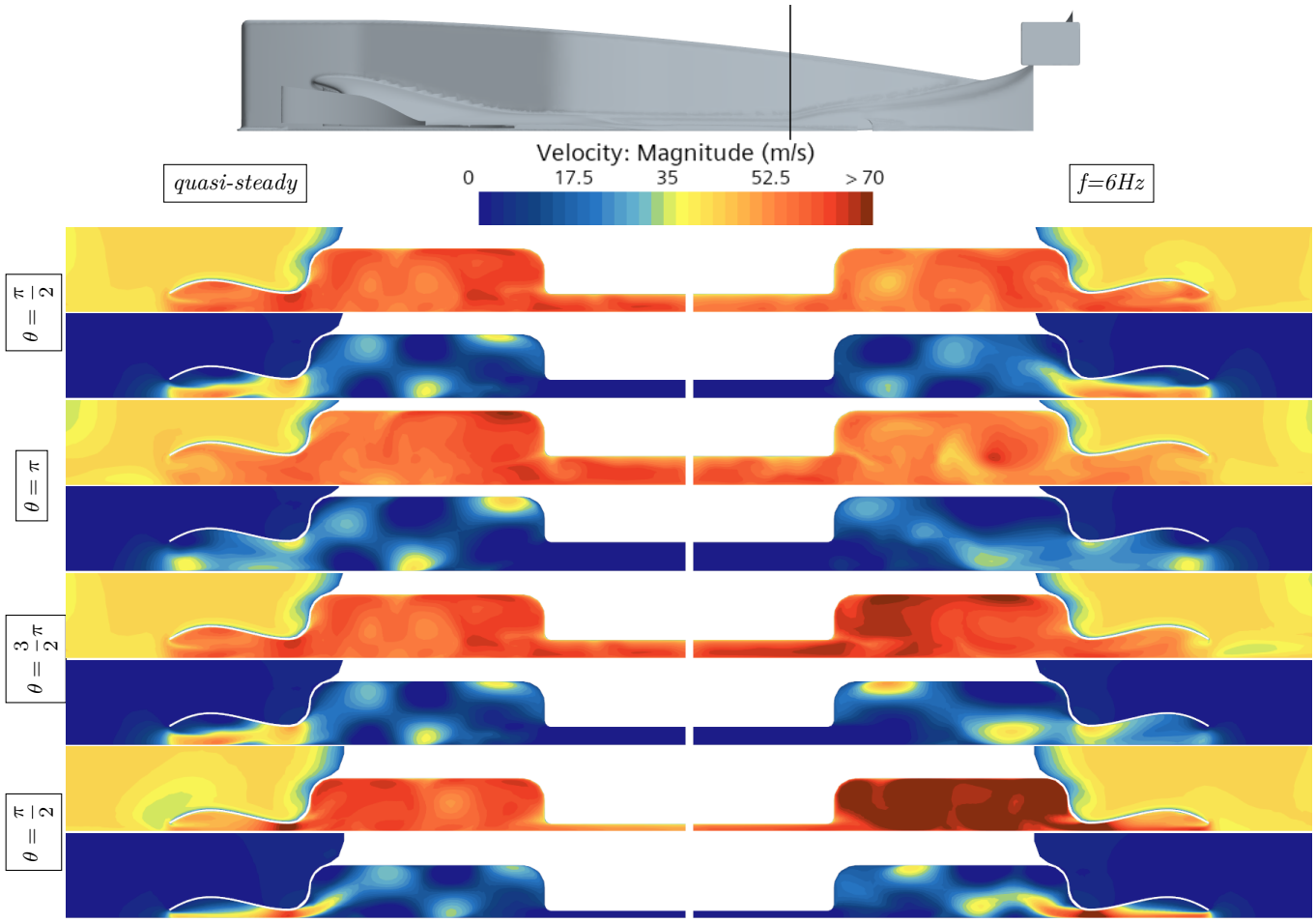


**Figure 6.22:** *Comparison of different phase angles between quasi-steady and 6hz 40m/s. The above sets are the contour plot of the velocity magnitude and on the below ones the horizontal velocity component(>0 if moving toward the symmetry plane). Above is shown the Y-Z section position to be at the start of the diffuser*

Looking at these figures, it is clear that during porpoising oscillations, the unsteady effects are non-negligible. Major differences occur at the minimum ride height and already start at $theta = \frac{3}{2}\pi$. During quasi-steady descent, it is easy to observe that the channel velocity in Figure 6.22 remains almost constant. During unsteady descent, the velocity at the start of the diffuser keeps climbing, lowering pressure below the whole region. This phenomenon could be attributed to an "hysteresis" effect. However, it will become clearer at the end of this thesis that due to the predictability of this phenomenon across a wide range of geometries, the hysteresis effect can only partially explain these amplifications.

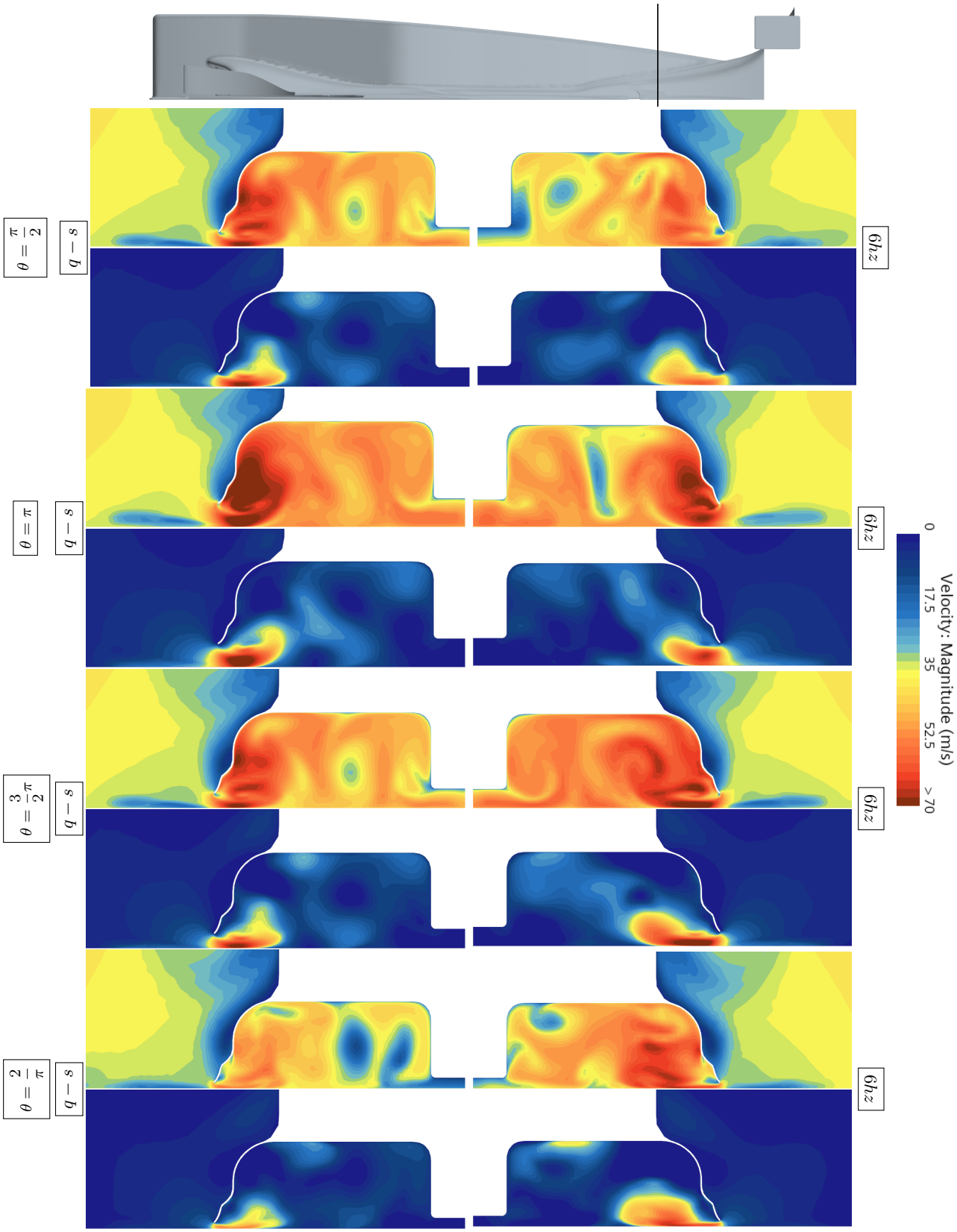


**Figure 6.23:** *Comparison of different phase angles between quasi-steady and 6hz 40m/s. The above sets are the contour plot of the velocity magnitude and on the below ones the horizontal velocity component(>0 if moving toward the symmetry plane). Above is shown the Y-Z section position to be at the middle of the diffuser*

# Chapter 7

# URANS simulations of an inverted wing

## 7.1 Geometry

In order to collect a larger dataset encompassing a wider range of geometries and to attempt to isolate the specific geometrical features that primarily influence porpoising, several simpler yet still representative geometries have been introduced. All of these geometries share a common main body, which was modeled after the wing used in experimental ground effect testing described in [6]. The only dimensions held constant across all geometries are the airfoil's angle of attack and its chord length. All other dimensions have been systematically varied:

- Wing span
- Airfoil ground clearence
- Endplates presence or absence
- Endplates longitudinal estension
- Footplates presence or absence
- Footplates estension
- Central hull presence or absence
- Central Hull shape and dimension
- Combination of all of theese

## 7.2 Some examples

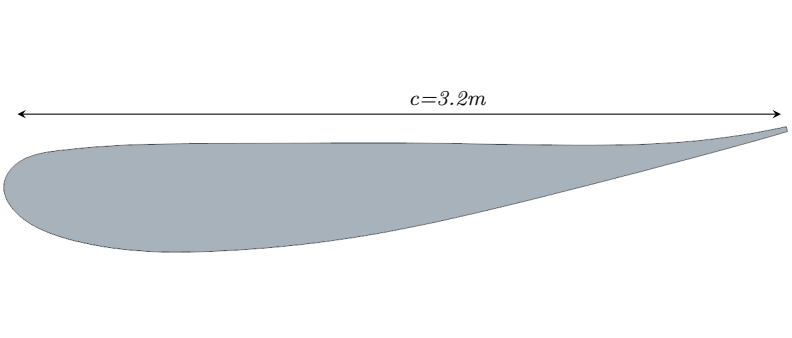


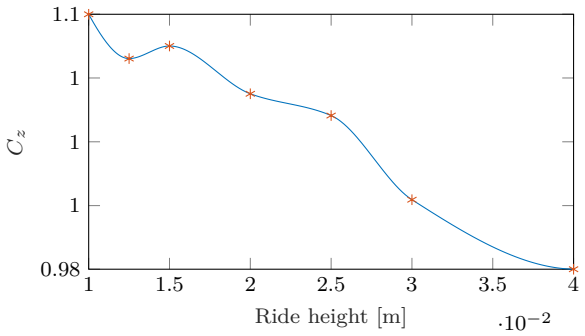


**(a)** *Simple*

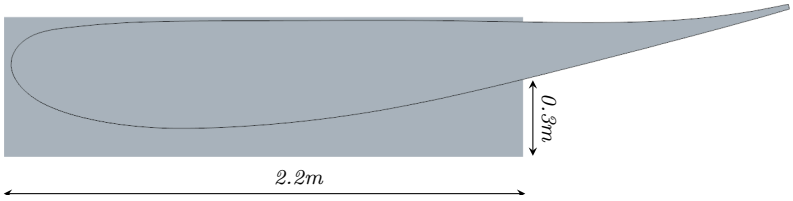


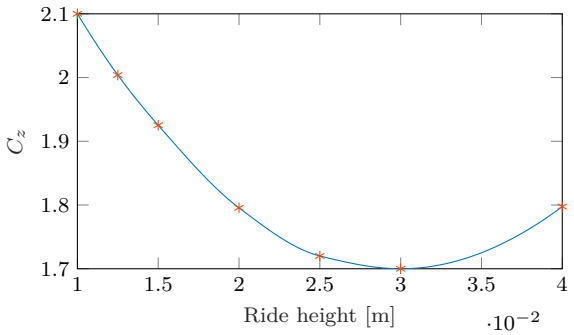


**(b)** *Long endplate*

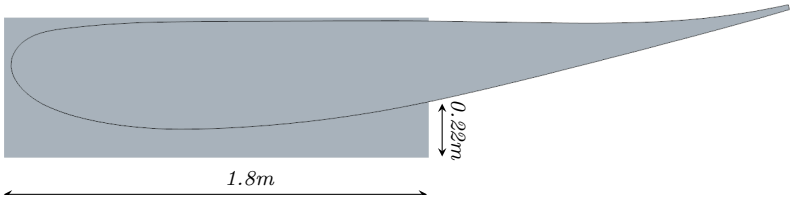


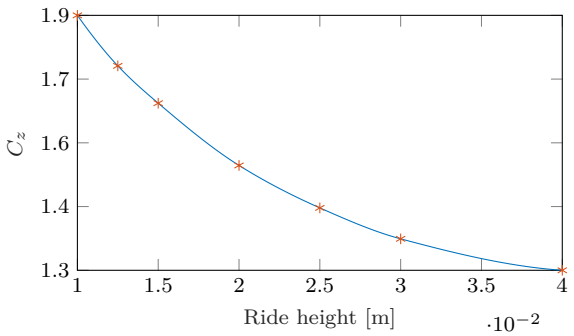


**(c)** *Short endplate*

**Figure 7.1:** *Sidewiew of some different simple geometries on the left and their corresponding steady state ride heigth sensitivity on the rhight.*

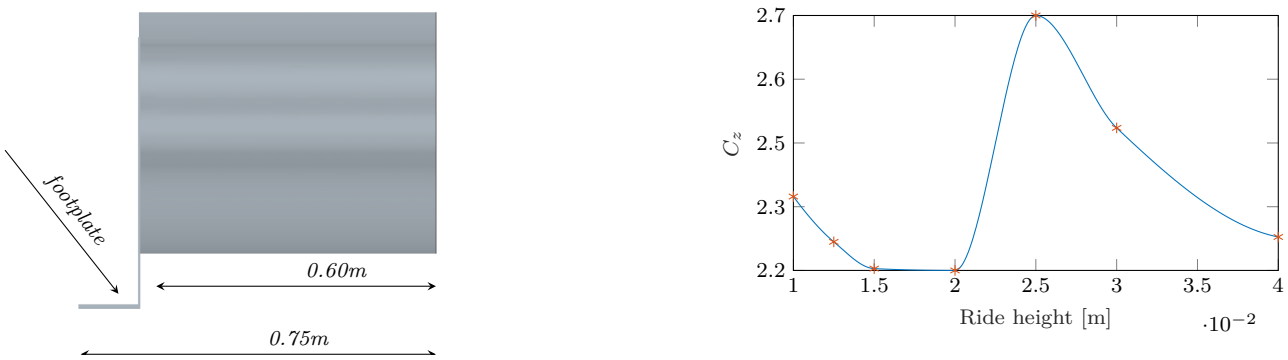


**(a)** *Wide footplate*

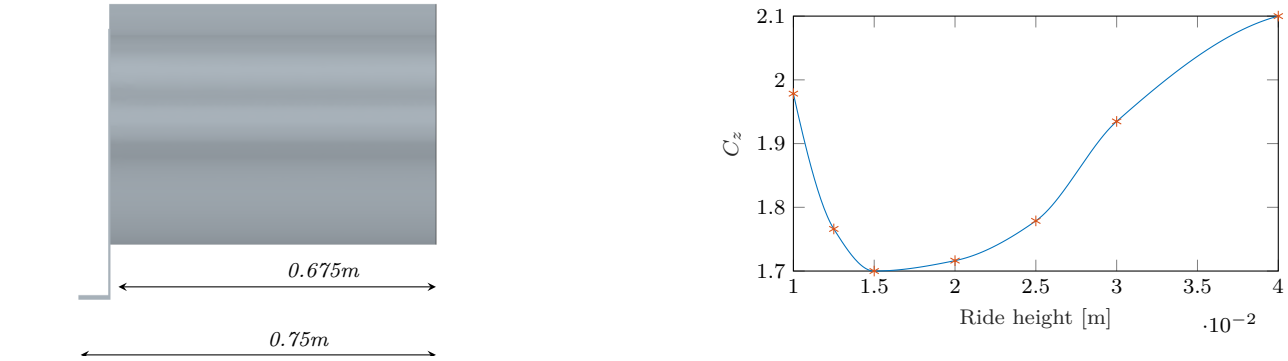


**(b)** *Wide span, short footplate*

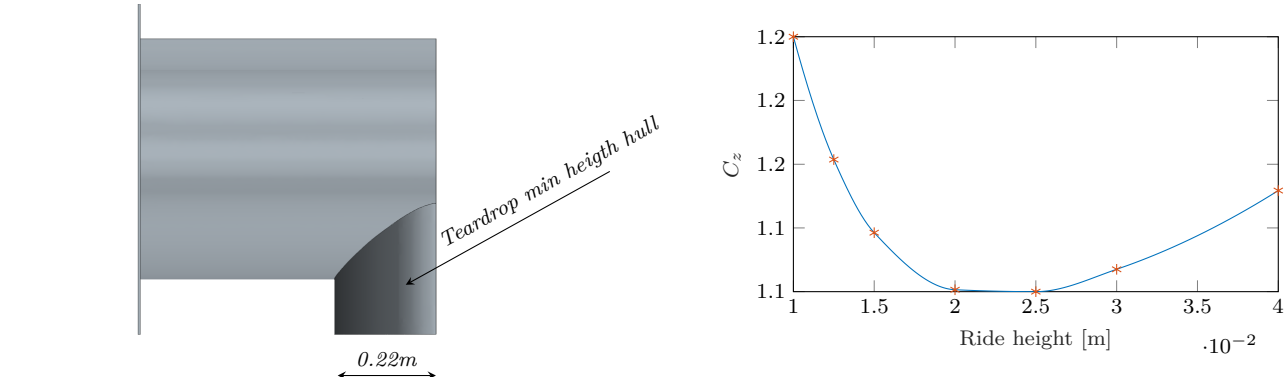


**(c)** *Teardrop hull*

**Figure 7.2:** *Frontal view of some other simple geometries on the left and their corresponding steady state ride heigth sensitivity on the right.*

As shown in the above images and the corresponding steady-state ride height sensitivity plots, the selected range of geometries provides a wide variety of aerodynamic behaviors. The objective of this thesis is to gain insights into the unsteady behavior of a racecar without the need for computationally expensive time-variant simulations or the complexities and potential fragility of simulation setups. In the next chapter, it will be demonstrated how this seemingly chaotic distribution of ground effect behaviors can be organized.

# Chapter 8

# Modelling forces

## 8.1 Literature review

Theodorsen in [15] developed an analytical expression for the lift generated by a 2D airfoil under sinusoidal motion. Although the solution is restricted to a symmetric airfoil in freestream and potential flow for small oscillations, it is still useful to understand the composition of the aerodynamic forces acting on an oscillating body. The expression for the downforce per unit length for the pure heaving case can be written as follows:

$$L = \underbrace{\frac{1}{4}\pi\rho c^2\ddot{z}}_{Noncirculatory} + \underbrace{\frac{1}{2}\rho U_\infty c C(k) C_z \dot{z}}_{Circulatory} \tag{8.1}$$

The unsteady downforce generated, as predicted by Theodorsen, consists of two distinct components: one that depends on the negative lift coefficient, denoted as $C_z$ (positive when the lift is towards the ground), and another one that does not. These two contributions are commonly referred to as the circulatory and non-circulatory components, respectively. The non-circulatory term arises from the displacement of air by the airfoil. In eq. (8.1), this component has been modeled as a cylinder of air with diameter $c$ moving with the airfoil. This effect is also called "added mass effect". For sinusoidal motion, the vertical coordinate $z(t)$ (positive away from the ground) can be replaced by $z(t) = z_0 e^{iwt}$. Consequently, the non-circulatory term can be expressed as follows:

$$\frac{1}{4}\pi\rho c^2\ddot{z} = \left(-\frac{1}{4}\pi\rho c^2 w^2\right) z_0 e^{iwt} \tag{8.2}$$

The circulatory term is filtered by the complex function $C(k) = F(k) + iG(k)$, known as Theodorsens function. The function $C(k)$ affects both phase and magnitude of the quasi steady response, and

depends on the reduced frequency $k$ that for an oscillating arifoil section can be defined as:

$$k = \frac{\pi f c}{U_\infty} \tag{8.3}$$

The reduced frequency represents the ratio between the time a particle takes to traverse the chord of the airfoil $c/U_\infty$ and the oscillation period $1/f$. In eq. (8.2) it can be observed that the added mass effect is proportional to $w^2 = 4(\pi f)^2$ while:

$$\lim_{k \to \infty} C(k) = 0.5 + 0j \tag{8.4}$$

$$\lim_{k \to 0^+} C(k) = 1 + 0j \tag{8.5}$$

meaning the circulatory component are going to be significant only at low oscillation frequencies while the added mass effect is going to be the predominant component at high oscillation frequencies.

For a 2D nonsymmetrical heaving airfoil in ground effect, three different mechanisms describe unsteady downforce generation. In [9], these mechanisms are referred to as the "ground effect", "incidence effect", and "added mass effect." The "incidence effect" corresponds to the circulatory term in eq. (8.1). The "ground effect" component is analogous to the circulatory component in eq. (8.1) but accounts for ground effect. The "added mass effect" is, in principle, the same as in Theodorsen's formulation. However, it has been observed to lose its symmetry at high enough frequencies, resulting in a non-zero average contribution that positively contributes to downforce generation. In this thesis, simulations of various geometries have been conducted across a range of frequencies, $f \in [3 - 6]Hz$, which corresponds to the frequency range where porpoising phenomena were observed during the 2022 Formula One season. Using a chord length of $c = 3.2m$ for the venturi channel and the definition eq. (8.3), a range of reduced frequencies $k \in [0.754 - 1.508]$ was obtained. It was noted in [9] that for values of $k > 0.11$, the quasi-steady hypothesis is no longer a valid assumption, corroborating the findings in chapter 6 and chapter 7. Maximum perceived incidence variation occurs during the moment of maximum heaving velocity. With a free flow velocity of 40 m/s and a 30 mm heaving amplitude at 6 Hz, the maximum vertical velocity is $U_z = \pm 0.566 m/s$, resulting in a maximum variation in perceived incidence for the geometry of approximately $a_{eff} \sim \pm 0.8^\circ$. Since this thesis has primarily focused on very low aspect ratio geometries ($AR \sim 0.3 < 1$), incidence angle sensitivity can be considered negligible in comparison to ride height sensitivity. This observation leads to the conclusion that all the unsteady effects observed in these simulations are primarily related to the "ground effect" and not to the better-known "incidence effect" present in Theodorsen's formulation.

In [11], simulations had an identical set-up as [9], focusing more quantitatively on unsteady force generation. For the range of $k$ considered in this thesis, it was observed that mean forces should remain unaffected during unsteady motion, while the amplitude should increase with oscillation frequency.

This deviation from the quasi-steady hypothesis occurs even for the lowest considered value of $k = 0.754$.

## 8.2 Mean forces

For all the simulations conducted, the time averaged value of the unsteady downforce coefficient $\overline{C_z^k}$ has been plotted against the time averaged value of the quasi-steady assumption downforce coefficient $\overline{C_z^0}$, yielding fig. 8.1.

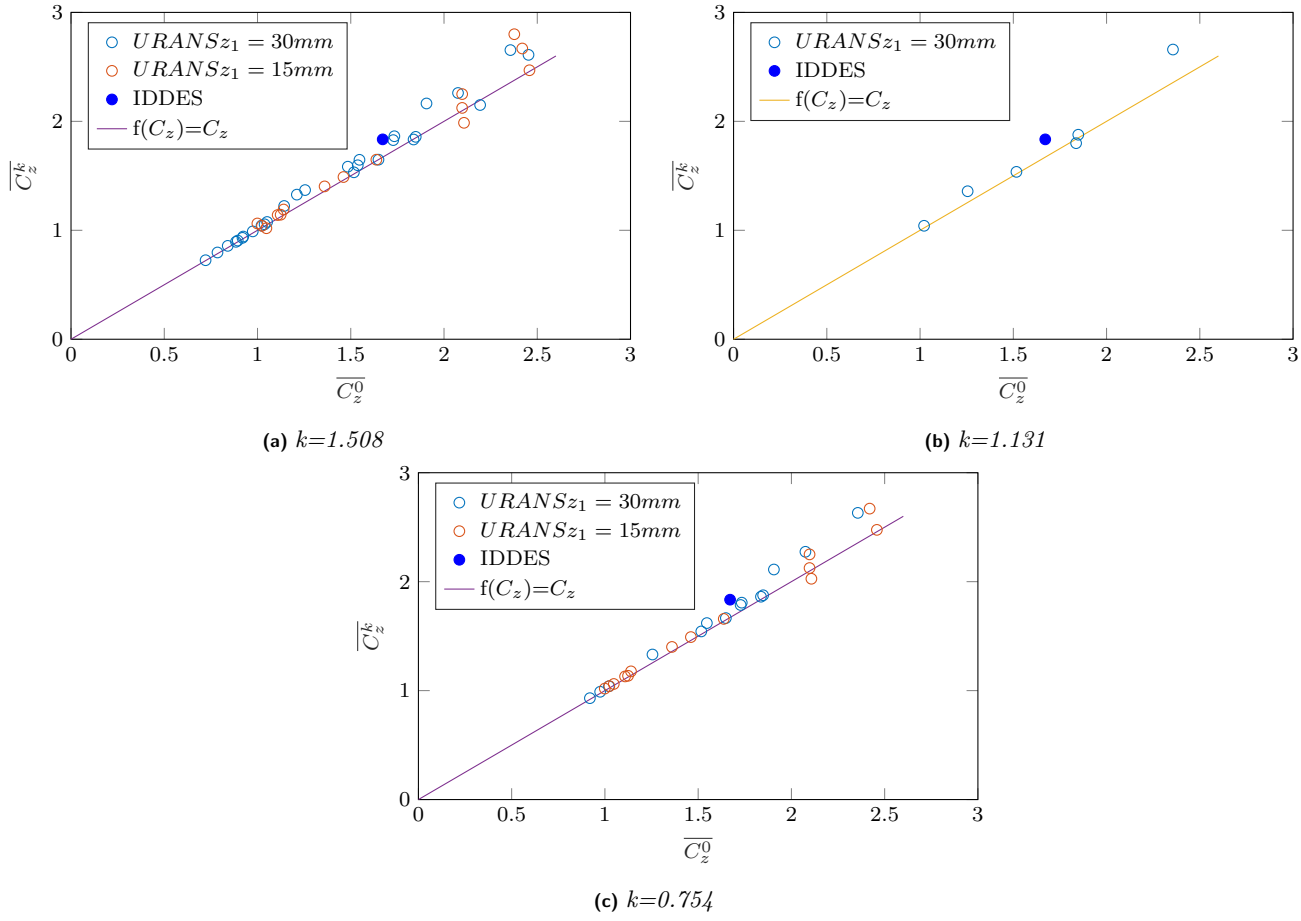


**(a)** *k=1.508*

**(b)** *k=1.131*

**(c)** *k=0.754*

**Figure 8.1:** *Average value for the unsteady signal $\overline{C_z^k}$ plotted over the quasi steady asumption$\overline{C_z^0}$ for all the simulations done. Including the ones at hald oscillation amplitude $z_1 = 15mm$*

These results are mostly consistent with what was found in [9] and [11], which indicates that for sufficiently low values of the reduced frequency k, there are no significant unsteady effects on the mean forces. However, geometries with the highest value $\overline{C_z^0}$ seem to experience the biggest deviation even at the lowest frequency. To achieve a higher level of precision in the final prediction, it might be useful to introduce a slight non-linearity in the relationship between the unsteady $\overline{C_z^k}$ and the quasi-steady $\overline{C_z^0}$.

## 8.3 GE parameter

As mentioned in section 8.1, the added mass effect is related to the flow accelerations imparted by the geometry. Therefore, to gain a deeper understanding of the relationship between geometrical features and this effect, it is more useful to examine the highest frequency conditions. Before starting to discuss these terms, it is usefull to show some correlations. To quantify the magnitude of the periodic unsteady downforce coefficent $magC_z^k$ a frequency decomposition has been achieved through a fast fourier transform algorithm.

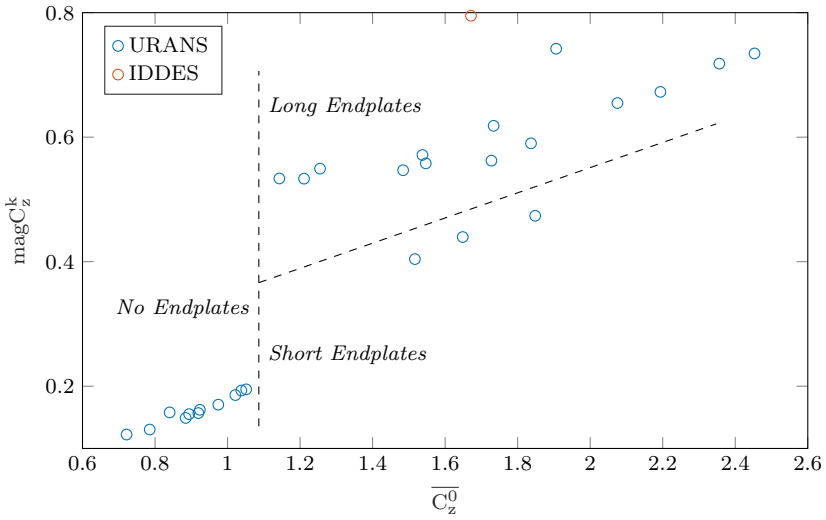


**Figure 8.2:** *$magC_z^k$ plotted against the mean quasi-steady $\overline{C_z^0}$*

By plotting $magC_z^k$ against the mean quasi-steady $\overline{C_z^0}$ in fig. 8.2, a clear separation is evident between geometries with different endplate extensions. The "No Endplate" group falls on a particular straight line, while the "long endplate" and "short endplate" groups follow different straight lines. No other geometrical features seem to affect this correlation. Observing fig. 8.2, it can be hypothesized that the circulatory components are somewhat proportional to $\overline{C_z^0}$ and the misalignment is caused by a non-circulatory component. Since it has already been established in section 8.1 that the non-steady effects are most likely due to ground effect, to better isolate its influence, a new parameter, denoted as $GE$, has been defined as follows:

$$GE = \frac{2}{\rho S U_\infty^2} \int_{Ground} p(x,y) Weigth(x,y)\, dA \tag{8.6}$$

Where the adimensional coefficients are the same for all negative lift coefficients. $GE$ represents a weighted "ground load." Considering the venturi channel layout in fig. 6.13, it is useful to note that when an airfoil or a generic surface is close enough to perceive ground effect, its pressure field will influence the pressure distribution on the ground, as shown in fig. 8.3.

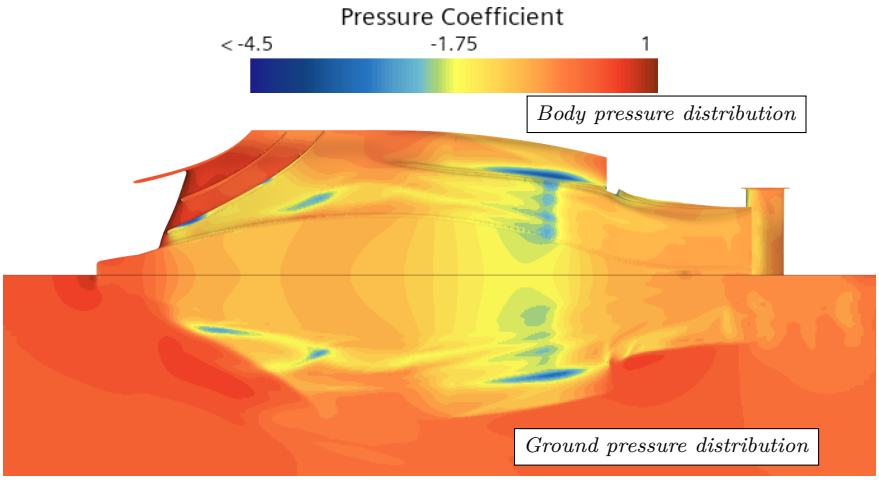


**Figure 8.3:** *Comparison between the body surface pressure distribution and the ground pressure distribution*

Of course the pressure distribution on the ground will be affected also by other aerodynamic phenomena, mainly by the interaction with edge vortices. To reduce the effects of pressure distribution due to vortices on the GE parameter a weighting function $Weigth(x, y)$ has been introduced in eq. (8.6) and defined as follows:

$$Weigth(x,y) = \begin{cases} \left(1 - \dfrac{y}{y_{edge}(x)}\right)^2 & \text{if } y \leq y_{edge} \\ 0 & \text{if } y > y_{edge} \end{cases} \tag{8.7}$$

This function depends on the y-coordinate and is scaled to be 1 at the middle symmetry plane and 0 from the edge of the geometry outward for each section, as shown in fig. 8.4.

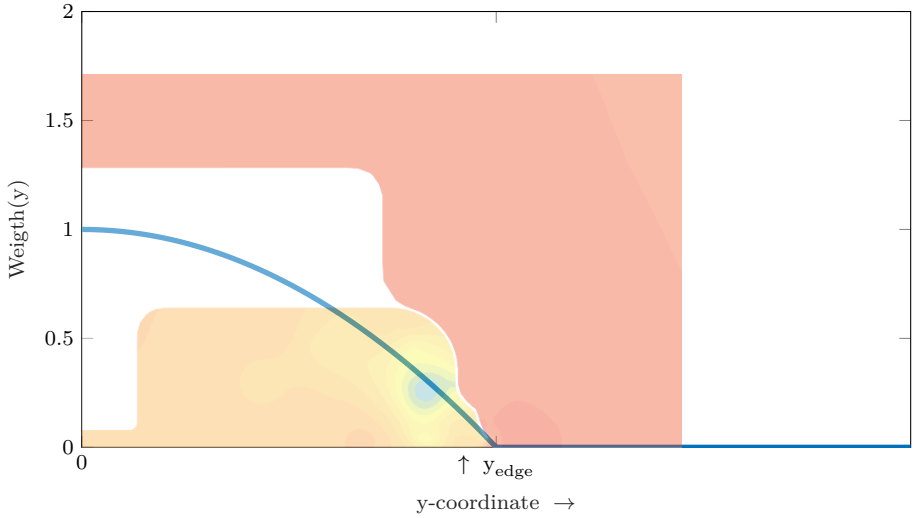


**Figure 8.4:** *Superposition of the function Weigth(y) and a Y-Z section*

If the magnitude of the unsteady forces $magC_z^k$ is plotted against the newly defined quasi-steady

time-averaged $\overline{GE^0}$ instead of being plotted against the mean quasi-steady downforce coefficient $\overline{C_z^0}$ fig. 8.5 is the result.

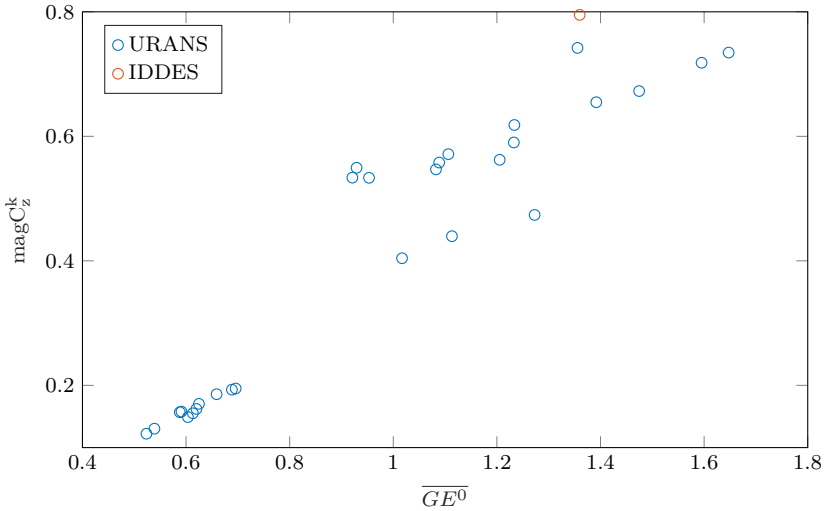


**Figure 8.5:** *$magC_z^k$ plotted against the mean quasi-steady ground load $\overline{GE^0}$*

By using a quasi-steady parameter that better represents the ground effect-related downforce production, a stronger correlation with the 1st mode magnitude $magC_z^k$ has been obtained. Various weight functions, other than the one presented in eq. (8.7), were also tested, such as linear functions, continuous functions, and step functions. The choice of weight function had little to no impact on the correlation with $magC_z^k$, as long as its value was much smaller from the edge outward compared to the middle of the domain.

## 8.4 Non circulatory components

While the introduction of the GE parameter has indeed led to an almost linear correlation with $magC_z^k$ in fig. 8.5, the three distinct groups of geometries, distinguished by differences in endplate extension, remain clearly visible. At this point, it is reasonable to assume that these offsets represent a manifestation of non-circulatory components. These components, by definition, are independent on the ground effect downforce production mechanism and result from the air displacement due to the body heaving motion. As described in eq. (8.2), there is no dependency on geometrical features, with the only geometrical link being the cord length $c$. This formulation is also inadequate for low aspect ratio geometries, as it describes the force needed to accelerate a cylinder of air of diameter $c$ across the wing span. The volume of air displaced by a 3D low aspect ratio geometry in close proximity to the ground is expected to exhibit a more three-dimensional nature. However, merely adjusting the volume in eq. (8.2) to accommodate low aspect ratio geometries would not explain the observed differences arising from variations in endplate longitudinal extension. Because endplates do not displace air when

moving vertically, all the considered geometries displace a very similar value of $V_{displaced}$ due to their nearly identical horizontal surface area. In fact, the geometries with the largest horizontal surface area do not exhibit greater deviations than the others. To address this issue, the problem has been divided into two parts, considering the volume displaced by the top and bottom body surfaces. For the top of the geometry, which is away from ground-related effects, the approach is similar to Theodorsen's, but half of an ellipsoid is considered instead of a cylinder.

$$V^{top}_{displaced} = \frac{2\pi\left(ca\frac{a}{2}\right)}{3} = \frac{\pi ca^2}{3} \tag{8.8}$$

Where $a$ represents the maximum y-extension, and $a/2$ has been arbitrarily chosen as the third dimension of the ellipsoid. Following Theodorsen's formulation, eq. (8.2) results in the following non-circulatory term, $C^{top}_{z,nc}$:

$$C^{top}_{z,nc} = V^{top}_{displaced}\rho\ddot{z}\frac{2}{\rho SU^2_\infty} \tag{8.9}$$

For what concerns the bottom surface, a different added mass mechanism has been hypothesized. This mechanism takes into account the force needed to accelerate the displaced volume of air between the ground and the endplate edge. Let us consider a generic section like in fig. 8.6, by assuming a 2D longitudinal behaviour. For this section the volume displaced $dV = dz\Delta xL_0$, during heaving motion, needs to go through the narrow section $H_E$ and by doing so it need to be accelerated. The force necessary to accelerate this volume can be written using the 2nd law of motion:

$$dV\rho\ddot{y} = dz\Delta xLo\rho\ddot{y} = dF_y \tag{8.10}$$

Where $\Delta x$ is the Hypothetical width of the 2D section, and $\ddot{y}$ is the flow acceleration across the edge gap. Dividing both members by an infinitesimal time increment dt:

$$\dot{z}\ddot{y}\Delta xLo\rho = \dot{F}_y \tag{8.11}$$

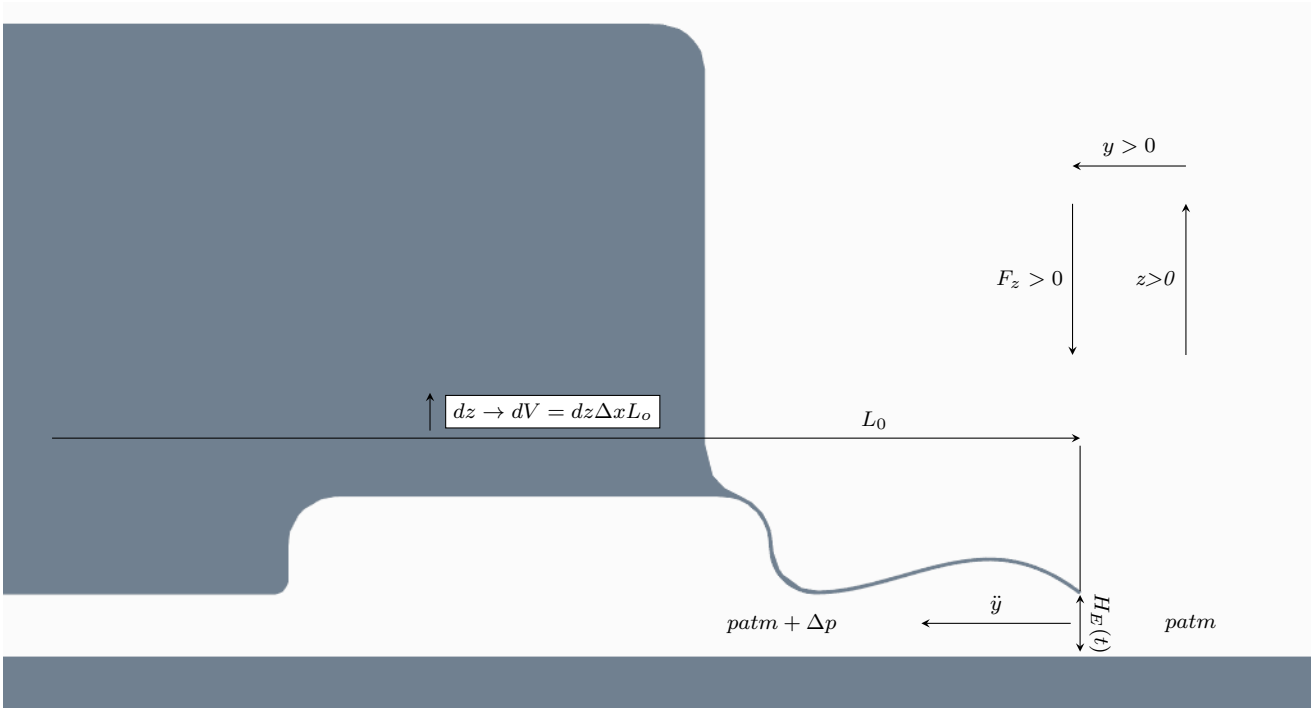


**Figure 8.6:** *representation of the geometrical quantities used to determine the added mass effect*

Leveraging the assumption of incompressible flow and ignoring viscous effects, the following mass conservation equation holds:

$$dz\Delta x Lo\rho = dy\Delta x H_E(t)\rho \tag{8.12}$$

Dividing by dt:

$$\dot{z}Lo = \dot{y}H_E(t) \tag{8.13}$$

Taking then the time derivative:

$$\frac{\partial}{\partial t}\left(\dot{z}Lo\right) = \frac{\partial}{\partial t}\left(\dot{y}H_E(t)\right) \tag{8.14}$$

$$\ddot{z}L_0 = \ddot{y}H_E + \dot{y}\dot{H_E} \tag{8.15}$$

The follwing assumption was made: the term $\dot{y}\dot{H_E} << \ddot{y}H_E$. This assumption can be justified by considering small vertical velocities and large $L_0/H_E$ ratios. This hypothesis ensures that $\dot{H_E}$ remain small compared to $\ddot{y}$, which is significant for large values of $L_0/H_E$. The acceleration of the volume dV going across the $H_E$ section can therefore be expressed as:

$$\ddot{y} \sim \frac{\ddot{z}L_0}{H_E} \tag{8.16}$$

The force $F_y$ required to generate this acceleration can be expressed as a pressure differential acting on the $H_E$ section. It can be assumed that the pressure differential $Dp$ acting on the edge gap section will propagate throughout the enclosed volume. It is important to remember that the force $F_y$ results

from the body motion, which means that the reaction force acting on the body will also be generated by the same $Dp$ but acting over a much larger surface.

$$F_Z = \frac{F_y L_0}{H_E(t)} \tag{8.17}$$

By substituting eq. (8.16) into eq. (8.11), we can derive the following ordinary differential equation:

$$\Delta x \dot{z} \ddot{z} \frac{Lo^2}{H_e(t)} \rho = \dot{F}_y \tag{8.18}$$

A spectral analysis of this equation has been performed to determine its characteristics analytically. Starting with:

$$\Delta x \dot{z} \ddot{z} Lo^2 \rho = \dot{F}_y(H_E(t)) \tag{8.19}$$

and applying the following identities for a sinusoidal heaving oscillation:

$$z = z_1 e^{iwt} \tag{8.20}$$

$$H_E = H_{E0} + z_1 e^{iwt} \tag{8.21}$$

$$F_z = F_{z1} e^{iwt} \tag{8.22}$$

The latter of this set of equations is a hypothesis made to obtain a similar behavior as the original Theodorsen non-circulatory term: in phase with accelerations and with the same frequency as the oscillation motion. By substituting these equations into eq. (8.19):

$$-iw^3 \rho z_1^2 \Delta x L_0^2 e^{i2wt} = \dot{F}_y(H_{E0} + z_1 e^{iwt}) \tag{8.23}$$

Leveraging the relationship between $F_y$ and $F_z$ as defined in eq. (8.17), we can derive the following expressions:

$$F_y = \frac{F_{z1} H_{E0}}{L_0} e^{iwt} + \frac{F_{z1} z_1}{L_0} e^{i2wt} \tag{8.24}$$

$$\dot{F}_y = iw \left( \frac{F_{z1} H_{E0}}{L_0} e^{iwt} + 2 \frac{F_{z1} z_1}{L_0} e^{i2wt} \right) \tag{8.25}$$

Substituting eq. (8.25) into eq. (8.23) and performing the product between $\dot{F}_y$ and $H_E(t)$ will yield a result as follows:

$$-iw^3 \rho z_1^2 \Delta x L_0^2 e^{i2wt} = A e^{iwt} + B e^{i2wt} + C e^{i3wt} \tag{8.26}$$

Having the coefficients A, B, and C, all different from 0 indicates that during the determination of the left term in eq. (8.19), information regarding the $e^{iwt}$ and the $e^{i3wt}$ modes has been disregarded. To maintain consistency with previous made assumptions, these modes will be disregarded once again. Therefore:

$$-iw^3 \rho z_1^2 \Delta x L_0^2 e^{i2wt} = B e^{i2wt} = iw \frac{3 F_{z1} z_1 H_{E0}}{L_0} \tag{8.27}$$

Rearranging the equation provides the magnitude for the new added mass effect:

$$F_{z1} = -\frac{w^2 \rho z_1 L_0^3 \Delta x}{3 H_{E0}} \tag{8.28}$$

By applying standard adimensionalization for aerodynamic forces, we can define the downforce coefficient for the non-circulatory terms in the same way as it was done for the top surface:

$$c_{z,nc}^{bot} = F_{z1} e^{iwt} \frac{2}{\rho S U_\infty^2} \tag{8.29}$$

Of course this result is valid in the 2D hypothesis since $F_{z1}$ is dependent upon $\Delta x$. To obtain the full contribute, there is the need to integrate this value along the longitudinal vehicle direction.

$$C_{z,nc}^{bot} = \int_x c_{z,nc}^{bot} Weigth(x)\, dx \tag{8.30}$$

Where the $Wheigth$ function takes into account the finite longitudinal exstension of endplates and has been arbitrarly chosen as shown in fig. 8.7

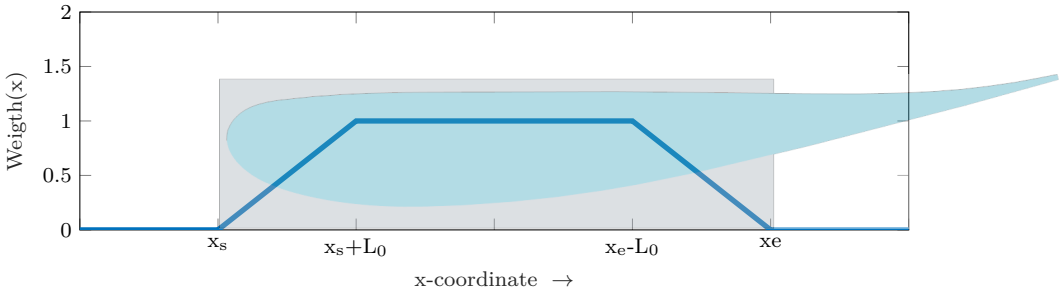


**Figure 8.7:** *superposition of the Weigth(x) function with a geometry equipped with endplates*

By adding together the two added mass components for each geometry and then subtracting them from the unsteady downforce signal, a reduced signal containing only the component directly related to ground effect is obtained. Observing fig. 8.8, it becomes apparent that the amplitude of the first mode of the reduced downforce, represented as $magC_z^k$ is well approximated by a linear relationship with the parameter $\overline{GE^0}$ for all the considered geometries.

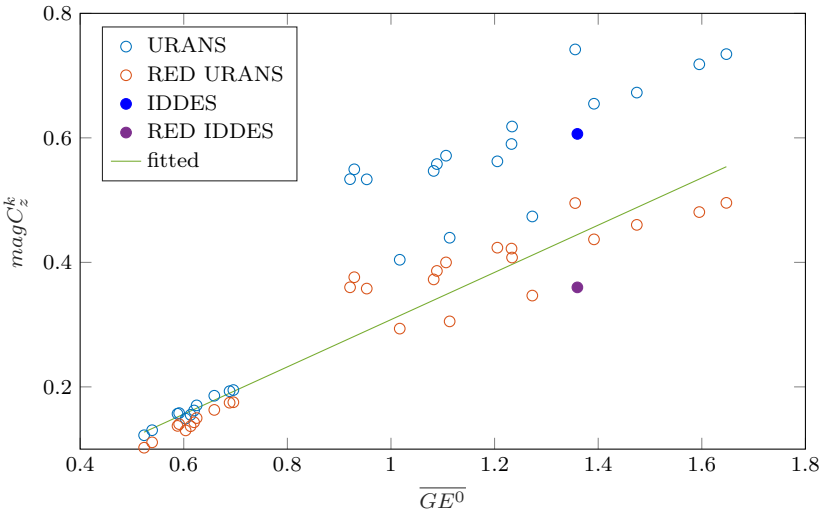


**Figure 8.8:** *Compatison between the full magnitude against the one reduced of its non circulatory terms. Linear fitting of the reduced magnitudes*

Looking at the difference in magnitude for the complex geometry IDDES simulation between the total signal and the reduced signal seem that a Formula One 2022 like geometry is particularly affected by added mass effect related amplification at high frequencies.

## 8.5 Circulatory terms

Now that the worst case scenario for circulatory components hasbeen addressed, it is possible to apply the same procedure to all the other oscillation conditions tested.

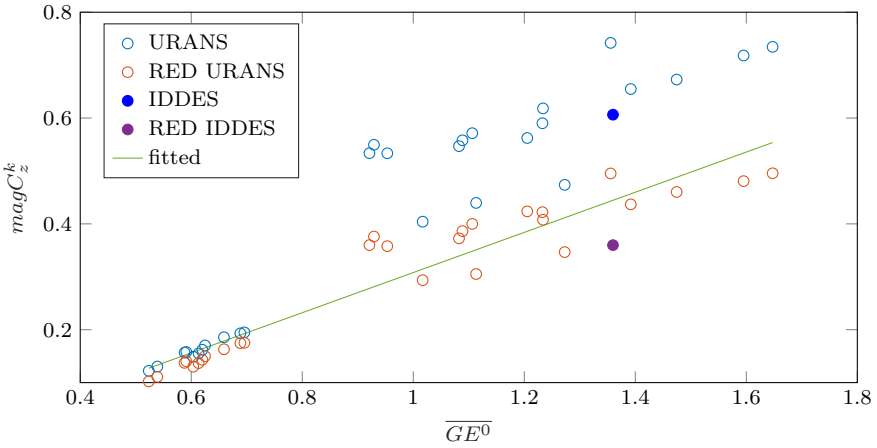


**(a)** *k=1.508*

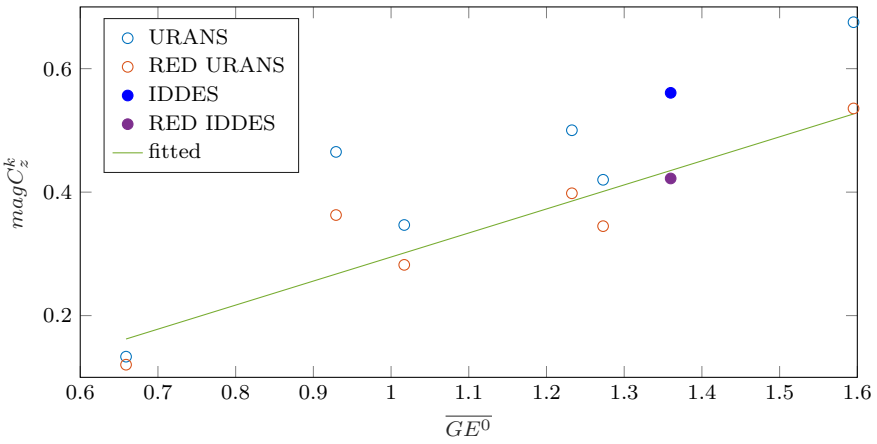


**(b)** *k=1.131*

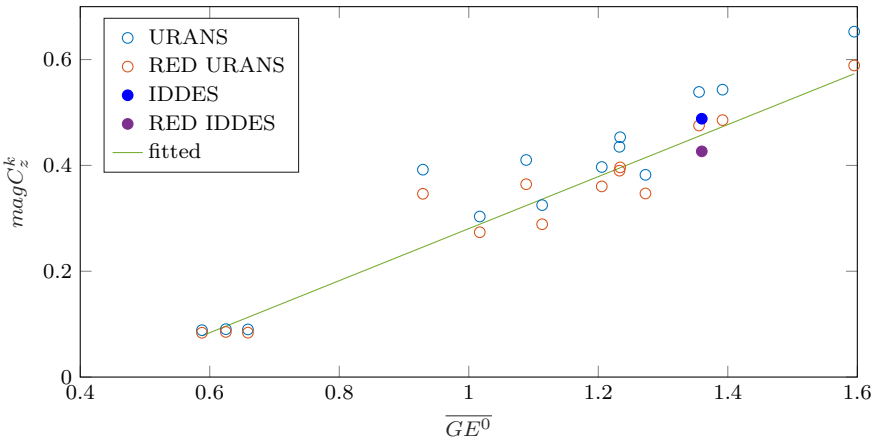


**(c)** *k=0.754*

**Figure 8.9:** *1st mode amplitude for $z_1 = 30mm$, comparison between total amplitude value, reduced amplitude value and linear fitting of the reduced value*

In fig. 8.9 the same linear correlation can be observed between the reduced $magC_z^k$ for lower reduced frequencies, although the effect of non-circulatory components is less prominent at $k = 1.131$. This is expected because the added mass effects are proportional to $f^2$. It can be noticed that at lower frequencies, the separation between different geometries with varying geometric features becomes less prominent, which reinforces the confidence in the hypothesis that the discrepancies seen at higher frequencies were solely caused by non-circulatory components.

| k | a | b |
|---|---|---|
| 1.508 | -0.0714 | 0.3798 |
| 1.131 | -0.0945 | 0.3894 |
| 0.754 | -0.2111 | 0.4916 |

**Table 8.1:** *Table containing linear fits parameters for different values of k and $z_1 = 30mm$. $magC_z^k = a + b\overline{GE^0}$*

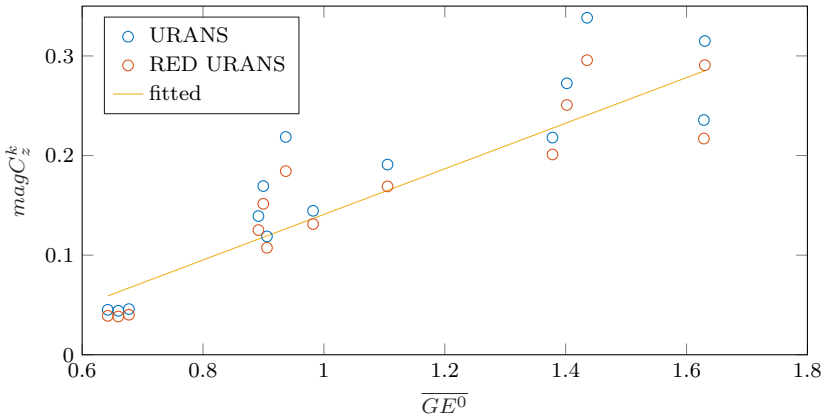


**(a)** *K=1.508*

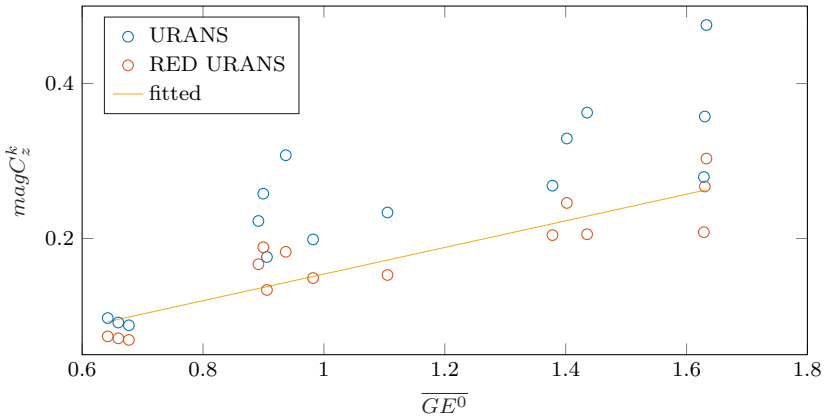


**(b)** *k=0.754*

**Figure 8.10:** *1st mode amplitude for $z_1 = 15mm$, comparison between total amplitude value, reduced amplitude value and linear fitting of the reduced value*

Looking at fig. 8.10 intead contains 1st mode-related data for geometries that were instead oscillated within a halved range of $z_1 = 15mm$ but at different mean heights. It is observed that, especially in the case of the maximum frequency, the non-circulatory load model applied has significantly reduced the uncertainty range of reduced amplitudes $magC_z^k$.

| k | a | b |
|---|---|---|
| 1.508 | 0.3794 | 0.1718 |
| 0.754 | 0.4916 | 0.2288 |

**Table 8.2:** *Table containing linear fits parameters for different values of k and* $z_1 = 15mm$. $magC_z^k = a + b\overline{GE^0}$

Below, the linear fitted functions have been interpolated across the entire considered range of $\overline{GE^0}$ and reduced frequency $k$ for both cases: full oscillation amplitude, and half oscillation amplitude. However, due to the limited resolution in the $k$ dimension, especially for the half-amplitude oscillation case, (which considers only two different values of $k$), these graphs should be interpreted with caution.

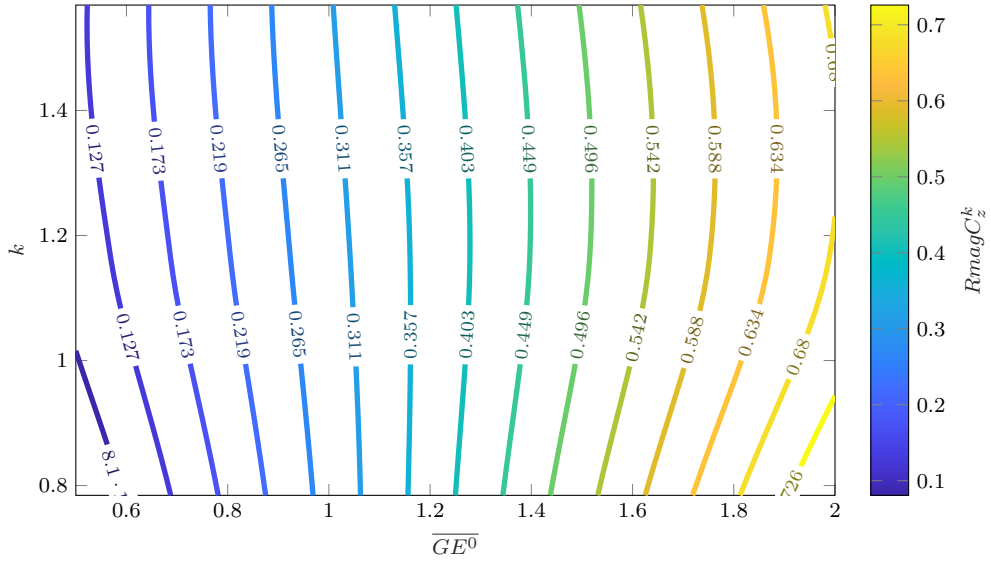


**Figure 8.11:** *Countour plot of the interpolated data across the different values of the reduced frequency k for* $z_1 = 30mm$

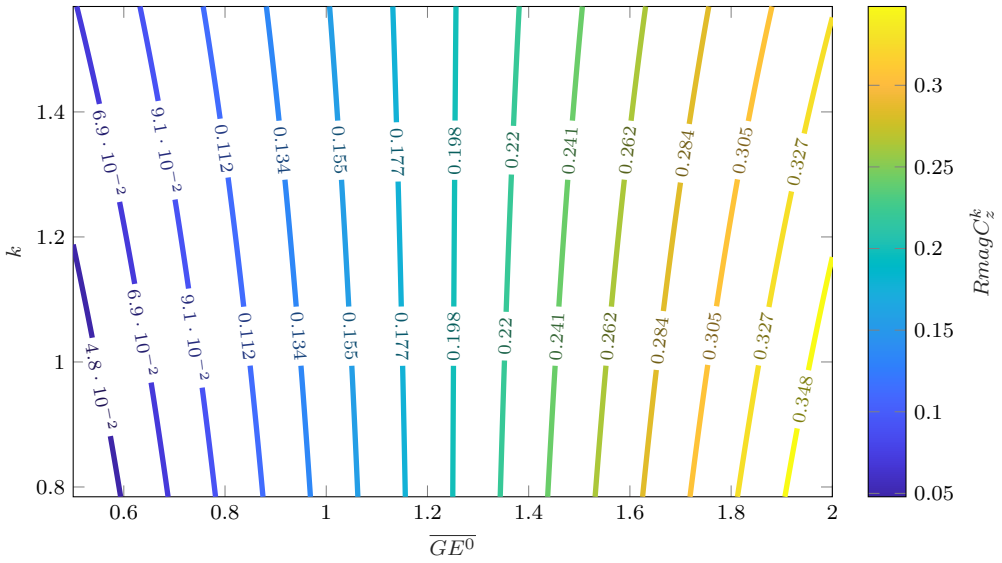


**Figure 8.12:** *Countour plot of the interpolated data across the different values of the reduced frequency $k$ for $z_1 = 15mm$*

## 8.6 Phase shift

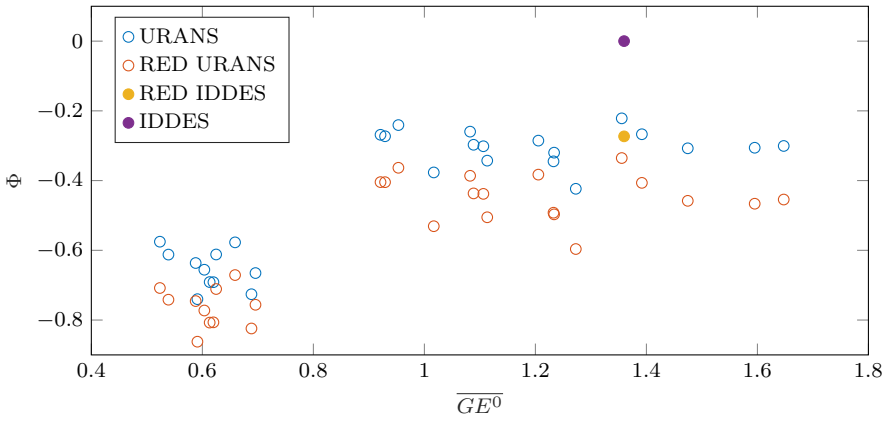


**(a)** *K=1.508*

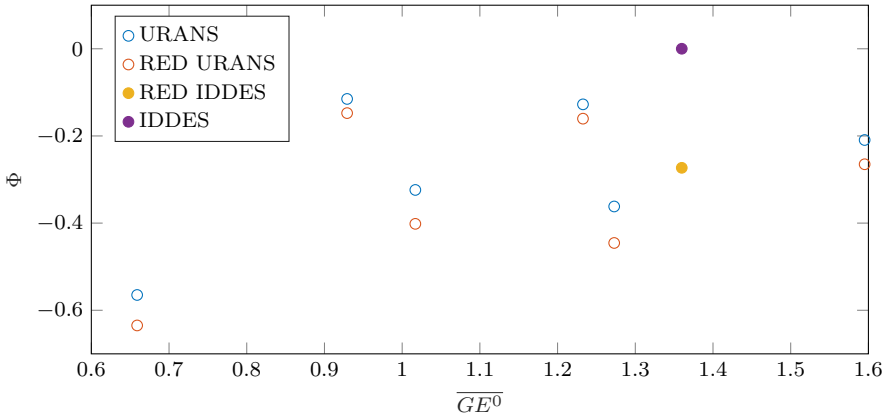


**(b)** *K=1.131*

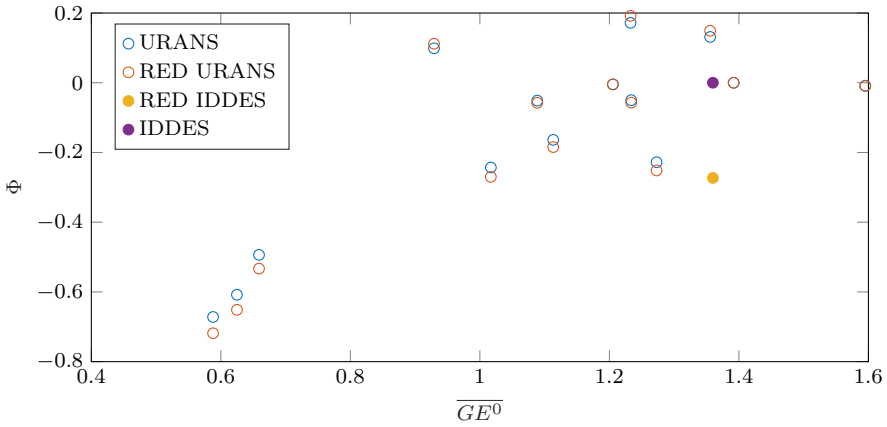


**(c)** *k=0.754*

**Figure 8.13:** *1st mode phase shift in rad for $z_1 = 30mm$, comparison between the unfiltered value and rhe reduced amplitude value*

In section 8.1, Theodorsen approach has been discussed for an oscillating 2D airfoil in freestream. In Theodorsen's formulation eq. (8.1), the total lift generated in the sinusoidal motion had two components: the non-circulatory one in counterphase with the oscillation and the circulatory one in phase

quadrature (before going through Theodorsen's formula $C(k)$ which induces a delay in the circulatory component). The combination of these two signals, depending on the properties of the airfoil and its oscillation regime, could lead to a variety of different phases for the overall lift signal. However, in the case of a 3D low aspect ratio ground effect-predominant geometry, this is not the case. Here, both circulatory and non-circulatory components are mostly in phase with the heaving motion. Phase variation must be caused only by some delay in the response of the circulatory component.

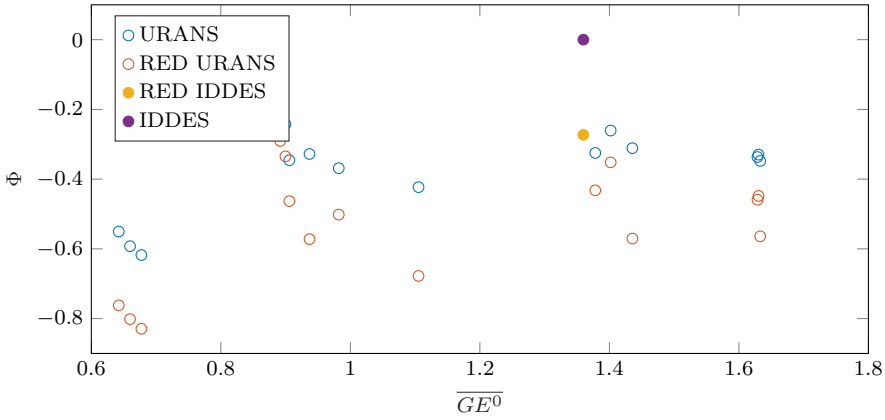


**(a)** *K=1.508*

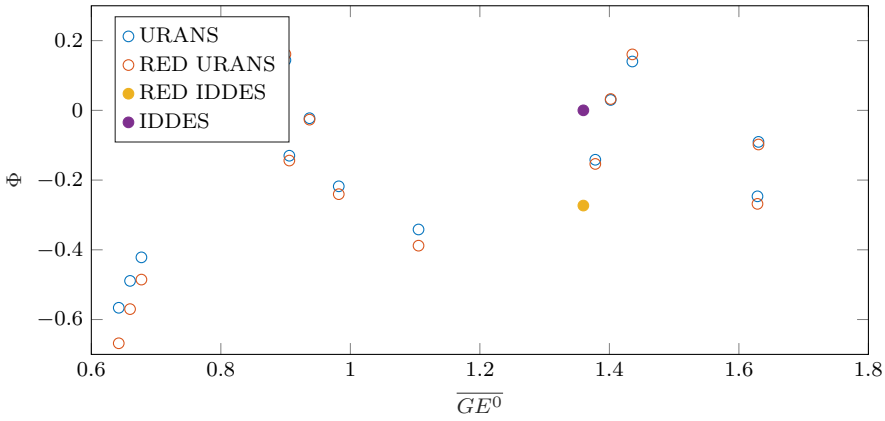


**(b)** *k=0.754*

**Figure 8.14:** *1st mode phase shift in radiants for $z_1 = 30mm$, comparison between the unfiltered value and rhe reduced amplitude value*

In both fig. 8.13 and fig. 8.14, it can be observed how the delay in the response increases with the reduced frequency, as expected. However, it also seems to depend on the magnitude of $\overline{GE^0}$ since the lowest values of mean ground load always coincide with the highest delay values. This could be caused by a shift in the principal downforce generating mechanism, transitioning from predominantly ground effect at high values of ground load to a more freestream-oriented load generation.

# Chapter 9

# Conclusions

In this thesis, the primary objective was to deepen our understanding of the aerodynamics behind the porpoising phenomenon observed in the 2022 Formula 1 World Championship. Several key findings and insights have emerged from this study. The methodology of overset simulations was successfully applied to investigate unsteady aerodynamic phenomena, with particular attention to the interaction between the ground and the vehicle's body. One of the most striking revelations is that the quasi-static assumption significantly underestimates the aerodynamic forces during porpoising conditions. This underestimation becomes even more pronounced at higher frequencies, where the quasi-static predictions fall short by more than 50% in estimating the peak forces generated. Comparisons between quasi-static and transient variables remained consistent whether obtained through URANS or IDDES simulations. Notably, for oscillatory phenomena such as porpoising, there is no compelling evidence to necessitate a CFD model capable of resolving turbulent scales. The study examined multiple geometries of increasing complexity, leading to the proposal of a predictive model. This model estimates the non-circulatory components for low aspect ratio geometries in close proximity to the ground. It introduced the concept of the ground load (GE) as a measure of ground effect, which demonstrated a strong correlation with the amplitude of force oscillations for low aspect ratio bodies that rely heavily on ground effect for lift generation. In the context of reduced frequencies $k \in (0.754 - 1.508)$ characteristic of porpoising, it was observed that transient effects do not significantly impact the time-averaged aerodynamic forces. This finding provides valuable insights into the frequency-dependent behavior of aerodynamic forces during porpoising. Furthermore, the study revealed that the delay in force response increases with reduced frequency but decreases with the ground load parameter (GE). This observation allows for a clear distinction between geometries heavily reliant on ground effect and those generating downforce through alternative mechanisms.

# Bibliography


[1] Dominic D.J. Chandar. On overset interpolation strategies and conservation on unstructured grids in openfoam. *Computer Physics Communications*, 239:72–83, 2019.

[2] Darwin L. Garcia and Joseph Katz. Trapped vortex in ground effect. *AIAA Journal*, 41(4):674–678, 2003.

[3] Mikhail S. Gritskevich, Andrey V. Garbaruk, Jochen Schütze, and Florian R. Menter. Development of ddes and iddes formulations for the k-shear stress transport model. *Flow, Turbulence and Combustion*, 88(3):431–449, 2012.

[4] Kan He, Guglielmo Minelli, Jiabin Wang, Guangjun Gao, and Sinia Krajnovi. Assessment of les, iddes and rans approaches for prediction of wakes behind notchback road vehicles. *Journal of Wind Engineering and Industrial Aerodynamics*, 217:104737, 2021.

[5] Joseph Katz and Frederic Morey. Aerodynamics of large-scale vortex generator in ground effect. *Journal of Fluids Engineering-transactions of The Asme - J FLUID ENG*, 130, 07 2008.

[6] Stephen Alexander Mahon. *The aerodynamics of multi-element wings in ground effect.* PhD thesis, University of Southampton, 2005.

[7] F. R. Menter. A Comparison of Some Recent Eddy-Viscosity Turbulence Models. *Journal of Fluids Engineering*, 118(3):514–519, 09 1996.

[8] Florian R Menter. Improved two-equation k-omega turbulence models for aerodynamic flows. Technical report, 1992.

[9] Juan Molina and Xin Zhang. Aerodynamics of a heaving airfoil in ground effect. *AIAA Journal*, 49(6):1168–1179, 2011.

[10] Juan Molina, Xin Zhang, and Antoni Alomar. Aerodynamics of a pitching and heaving airfoil in ground effect. *AIAA Journal*, 54:1–14, 02 2016.

[11] Juan Molina, Xin Zhang, and David Angland. On the unsteady motion and stability of a heaving airfoil in ground effect. *Acta Mechanica Sinica*, 27(2):164–178, 2011.

[12] Polhamus. A concept of the vortex lift of sharp-edge delta wings based on a leading-edge-suction analogy. 1966.

[13] Mikhail L. Shur, Philippe R. Spalart, Mikhail Kh. Strelets, and Andrey K. Travin. A hybrid rans-les approach with delayed-des and wall-modelled les capabilities. *International Journal of Heat and Fluid Flow*, 29(6):1638–1649, 2008.

[14] Philippe Spalart, W-H Jou, Michael Strelets, and Steven Allmaras. Comments on the feasibility of les for wings, and on a hybrid rans/les approach. 01 1997.

[15] Theodore Theodorsen. General theory of aerodynamic instability and the mechanism of flutter. Technical report, 1949.